

YOKOHAMA NATIONAL UNIVERSITY

DOCTORAL THESIS

**Numerical Investigations on the  
Aerodynamic Characteristics of Circular  
Cylinders with Indented Surfaces**

インデントケーブルの空力特性に関する数値解析による検討

*Author:*

Xiang ZHUANG

*Supervisor:*

Prof. Hitoshi YAMADA

Prof. Hiroshi KATSUCHI

Department of Civil Engineering

2021.2.26



## Abstract

The typical cable structures always suffer from severe wind loads and various kinds of vibrations. Driven by the need to reduce the drag and suppress the vibration, this thesis aims at investigating the flow characteristics and mechanisms on flow around indented circular cylinders. Based on the efficiency of roughened cylinders on flow control which has been investigated by bunches of researchers, a detailed investigation on the indented cylinder with various indentation parameters are discussed in the current thesis.

Firstly, two fully uniform indented cylinders with 6 rows and 8 rows of indentations on the circumference were taken into consideration. The aerodynamic force coefficients of both drag and lift forces are discussed. It is revealed that for the indented model, the sectional drag force reduces slightly at the indented surface when compared to the plain surface. By examining the pressure distribution, the value is lowest at the edge and largest at the pit for those indents at the frontal part, which is resulted from the acceleration of flow at the edge and deceleration inside the indent. By plotting the boundary layer profiles of velocity at the indents, it is disclosed that inside the indent, closed circulating flow could be formed with the “S” shape boundary layer profiles. At the location just downstream the indent, greater velocities are observed with higher vorticities. It means that the boundary layer is energized by those indents. These features are similar to a dimple on the cylinder, which should have effect on drag reduction at lower Reynolds number. While those indents located at the backward face of cylinder do not have such effects.

Secondly, three half uniform-indented cylinders with various indentation sizes are taken into consideration. The decrease in drag force is observed for all the indentation sizes. While for a larger indentation size, a reduction in lift force is also identified. By examining the velocities distribution in the wake region, it is found that the r.m.s. velocity in cross direction also reduced for the large indentation size cylinder. The stream-wise correlation of pressure coefficients and span-wise correlation of drag force on those indented models are found to be much weaker than the smooth one. The weaker correlation in span-wise direction is detected for large indentation size. By comparing the boundary layer profile of velocity just downstream of indent with that of smooth cylinder, it is identified that flow accelerates with deeper indents. It is argued that the rougher the cylinder, the more energetic the boundary layer. This feature contributes to an earlier transition on boundary layers from laminar to turbulence and delaying the separation.

Ultimately, circular cylinder with only one indentation located at various positions are investigated. Two types of indentations, i.e., indentation with and without bump at the edge, are taken into consideration. Both types can energize the velocity near the surface downstream the indentation. The indentation with bump are found to be more effective on empowering the boundary layers. The different flow mechanisms between these two cases are investigated by the streamline and kinetic turbulent energy

visualizations. It is found that the additional concave of indentation increases the surface roughness. Thusly, the skin friction increases, and the energy increases in the boundary layers. Larger shear layer instability and velocity fluctuations are detected at a higher Reynolds number though still in the subcritical regime. It is believed that the effects of indentation still work on a much higher Reynolds number, such as trans-critical one and contribute to an economic cost.

The considered three cases indicates the efficacy of indented cylinders with various design parameters. Triggered by the current studies, more research topics and some potential usages related with the indented cylinder and the indentation maybe investigated in the future.

## Acknowledgements

Three years past so fast and I will finish my study and research in Yokohama National University. I am so lucky and happy that I can stay in this quiet and beautiful city for these years and met a lot of lovely guys.

My chief advisors, Prof. Hitoshi Yamada and Prof. Hiroshi Katsuchi, have let me into this interesting world of structures and wind engineering. I met with both sensei in BBAA, Boston, 2016. Then also a short conversation in the café at Tongji University with Prof. Yamada. He kindly helped me to apply for the scholarship and answer my problems. During these 3 years, he also offered me with lots of great ideas in cable aerodynamics. This thesis is also the outcome of their kind help and supports during these years.

Prof. Tamura, Dr. Kim, Dr. Wang are thanked for giving me advices and personal communications. All the previous and current members in structural laboratory are thanked for their kind help and support.

I came to Japan by the so called Special English Program without any Japanese language skills. For 3 years, thanks to the Japanese courses in the international student center, I was so lucky that so many kind teachers kindly taught me Japanese, Imu sensei, Yamamori sensei, etc. Also, I was happy to make some good friends that help me to study Japanese from various countries. Specially, I would like to thank my tutor, Mr. Fujii, who taught me Japanese and skills on job hunting in Japan. I am also highly thankful and obliged to Japanese government for supporting me with the MEXT scholarship.

Because of corona virus, I am not able to go back to China for the past one and half year. I do miss my parents, my grandparents and my forever hometown, Longyanying road. They support me with unconditional love at any time.

Lastly, for my best friends. Ding, Kim, Peng, Lei, Coepin, Sang and Seven. I would like to mention the words I wrote in my master thesis again:

Live with dreams & 18 till we die.

いつまでも夢を、死ぬまで18歳。

愿我们永远有梦，愿我们致死都是18岁。

# Contents

<b>Abstract</b> .....	<b>2</b>
<b>Contents</b> .....	<b>5</b>
<b>List of figures</b> .....	<b>7</b>
<b>List of Tables</b> .....	<b>10</b>
<b>Chapter 1 Introduction</b> .....	<b>11</b>
1.1 Background .....	11
1.2 Problems statements and motivations .....	11
1.3 Scope and objectives .....	13
1.4 Thesis layout.....	14
<b>Chapter 2 Literature Review</b> .....	<b>15</b>
2.1 Surface roughness as flow control approach .....	15
2.2 Flow around a circular cylinder.....	16
2.3 Previous studies of a cylinder with rough surface.....	19
<b>Chapter 3 Methods</b> .....	<b>23</b>
3.1 Governing equations.....	23
3.2 Discretization.....	23
3.3 Matrix solvers.....	25
3.4 Solution procedures .....	25
<b>Chapter 4 Simulation on Flow Past a Circular Cylinder</b> .....	<b>28</b>
4.1 Geometry and mesh.....	28
4.2 Numerical methods.....	30
4.3 Verification using 3-D LES.....	31
4.4 Summary .....	41
<b>Chapter 5 Simulation of Flow Past Cylinders with uniform indented surface</b> .....	<b>42</b>
5.1 Case setup.....	42
5.2 Aerodynamic forces.....	44
5.3 Statistics on the cylinder surface .....	46
5.4 Statistics along the circumference of cylinder.....	49
5.5 Region division.....	54
5.6 Statistics of fields around the cylinder .....	55
5.7 Summary .....	59
<b>Chapter 6 Simulation of Flow Past Half-Indented Circular Cylinders</b> .....	<b>61</b>

6.1 Half uniform-indented circular cylinders with various indentation sizes.....	61
6.2 Half-indented circular cylinders with various indentation arrangements.....	74
6.6 Summary .....	80
<b>Chapter 7 Indentations on circular cylinders with different locations and shapes ....</b>	<b>82</b>
7.1 Case setup.....	82
7.2 Different locations and shape of indentations .....	83
7.3 Discussions.....	87
7.4 Summary .....	90
<b>Chapter 8 Final Remarks.....</b>	<b>92</b>
8.1 Conclusions .....	92
8.2 Prospects for future researches.....	93
<b>Bibliography.....</b>	<b>94</b>

## List of figures

Figure 1.1 An overview of Hutong bridge .....	12
Figure 1.2 An overview of Tatara Bridge, from Omishima Island, Japan .....	13
Figure 1.3 The pattern indented cylinder .....	13
Figure 2.1 Saguars in Saguaro National Park, southeastern Arizona, America .....	15
Figure 2.2 A golf ball model .....	16
Figure 2.3 Definition sketch .....	17
Figure 2.4 Drag coefficient of a circular cylinder at different surface roughness .....	20
Figure 4.1 Schematic of the fluid domain.....	29
Figure 4.2 Computational grid.....	30
Figure 4.3 Spatial-temporal distribution of force coefficients (Case A1).....	32
Figure 4.4 Space-averaged force coefficients (Case A1).....	33
Figure 4.5 Spatial-temporal distribution of force coefficients (Case A2).....	33
Figure 4.6 Time histories of force coefficients (Case A2).....	33
Figure 4.7 Spatial-temporal distribution of force coefficients (Case B1).....	34
Figure 4.8 Time histories of force coefficients (Case B1).....	34
Figure 4.9 Spatial-temporal distribution of force coefficients (Case B2).....	35
Figure 4.10 Time histories of force coefficients (Case B2).....	35
Figure 4.11 Spatial-temporal distribution of force coefficients (Case C).....	35
Figure 4.12 Time histories of force coefficients (Case C).....	36
Figure 4.13 Time-averaged pressure coefficients on the cylinder surface.....	36
Figure 4.14 Mean stream-wise and r.m.s. velocity along wake center line .....	37
Figure 4.15 Mean stream-wise and r.m.s. velocity at $x/D=0.6$ .....	37
Figure 4.16 Mean stream-wise and r.m.s. velocity at $x/D=1$ .....	37
Figure 4.17 Mean stream-wise and r.m.s. velocity at $x/D=2$ .....	38
Figure 4.18 Boundary layer profiles of the circular cylinder.....	39
Figure 4.19 Iso-surfaces of $Q = 1.5$ for the flow around the cylinder .....	40
Figure 5.1 Schematics of the cross-sectional and side views of the indented cylinders .....	43
Figure 5.2 Meshing .....	44
Figure 5.3 Spatial-temporal distribution of force coefficients (Case IND6) .....	45
Figure 5.4 Spatial-temporal distribution of force coefficients (Case IND8) .....	45
Figure 5.5 Mean pressure coefficient on cylinder surface (from a view of $45^\circ$ ).....	46
Figure 5.6 Mean pressure coefficient on cylinder surface (from a view of $135^\circ$ ).....	46
Figure 5.7 Distribution of mean pressure coefficient near the indentation for IND6..	47
Figure 5.8 Distribution of mean pressure coefficient for IND6.....	47
Figure 5.9 Distribution of mean pressure coefficient near the indentation for IND8..	48
Figure 5.10 Distribution of mean pressure coefficient for IND8.....	48
Figure 5.11 Comparison results of cylinder circumference for ORI and IND6 .....	49
Figure 5.12 Comparison results of cylinder circumference for ORI and IND8 .....	49



Figure 5.13 Boundary layer profiles near the indentation of IND6.....	50
Figure 5.14 Boundary layer profiles near the indentation of IND8.....	50
Figure 5.15 Vector plot showing flow within the indentations .....	51
Figure 5.16 Boundary layer profile of velocity at the trailing edge of indentation .....	52
Figure 5.17 Vorticity distributions at the indentations .....	53
Figure 5.18 Three-dimensional horseshoe vortices for IND8.....	54
Figure 5.19 Region division of indentation locations .....	54
Figure 5.20 Schematic of cylinder surface showing the two azimuthal profiles .....	55
Figure 5.21 Comparison of velocity statistics of three models.....	56
Figure 5.22 Comparison of pressure statistics of three models .....	57
Figure 5.23 3-D vortical structures for three geometries .....	58
Figure 5.24 Contour lines of stream-wise vorticity .....	58
Figure 6.1 Different sizes of indentation .....	61
Figure 6.2 Geometry of the half uniform-indented circular cylinder .....	62
Figure 6.3 Geometries of the cylinders with various indentation sizes .....	62
Figure 6.4 Spatial-temporal distribution of force coefficients (Case S1) .....	63
Figure 6.5 Spatial-temporal distribution of force coefficients (Case M2).....	64
Figure 6.6 Spatial-temporal distribution of force coefficients (Case B3).....	64
Figure 6.7 Sectional forces coefficients .....	65
Figure 6.8 Pressure distributions around the cylinders .....	66
Figure 6.9 Pressure distribution on cylinder surfaces .....	67
Figure 6.10 Comparison results of cylinder circumference.....	68
Figure 6.11 Sketch of pressure taps and reference tap.....	68
Figure 6.12 Stream-wise correlation contour of $C_p$ .....	69
Figure 6.13 Span-wise correlation coefficients of force coefficients .....	70
Figure 6.14 Mean stream wise velocity in the y-z planes for the indented cylinders..	71
Figure 6.15 The root mean square of velocity contours in the wake region.....	72
Figure 6.16 The sketch of calculation about the area difference of boundary layer profiles between a smooth cylinder and an indented one .....	73
Figure 6.17 Difference of boundary layer profiles .....	74
Figure 6.18 Different arrangement of indentations.....	74
Figure 6.19 Geometries of the cylinders with various indentation arrangements .....	75
Figure 6.20 Spatial-temporal distribution of force coefficients (Case MV).....	76
Figure 6.21 Spatial-temporal distribution of force coefficients (Case MH).....	77
Figure 6.22 Spatial-temporal distribution of force coefficients (Case MHD) .....	77
Figure 6.23 Sectional drag forces coefficients.....	77
Figure 6.24 Pressure distribution on cylinder surfaces .....	78
Figure 6.25 Mean pressure coefficients of cylinder circumference.....	79
Figure 6.26 Span-wise vorticity of cylinder circumference.....	79
Figure 6.27 Span-wise mean pressure coefficients at indentation row 3.....	80
Figure 7.1 <i>Left:</i> Indented cable of Tataru Bridge; <i>Right:</i> Design sketch and 3D models of indentation.....	82

Figure 7.2 Meshing of indentation with bumps (BIND).....	83
Figure 7.3 Difference of boundary layer profiles of velocity .....	84
Figure 7.4 The mean streamlines of two models at various angles .....	85
Figure 7.5 turbulent kinetic energy near the indentation at various angles .....	86
Figure 7.6 Sketch of flow at the indentations .....	87
Figure 7.7 The fluctuating stream-wise velocity at the indentation.....	88
Figure 7.8 Sketch of bodies with and without a separation point.....	89
Figure 7.9 Shape of slender and blunt bodies .....	90

## List of Tables

Table 4.1 Mesh dependency test. ....	29
Table 4.2 Force coefficients and Strouhal No. ....	31
Table 4.3 Experimental and numerical works of flow past a circular cylinder at Re=3900. ....	31
Table 4.4 Recirculation length of five cases .....	38
Table 5.1 The covered simulated cases .....	43
Table 5.2 Aerodynamic forces of three models .....	44
Table 6.1 Aerodynamic forces of three models .....	62
Table 6.2 Aerodynamic forces of three models .....	75

# Chapter 1 Introduction

## 1.1 Background

Long or tall structures have been widely constructed in recent years. As the structures have become slenderer and more flexible, such structures frequently suffer from excessive aerodynamic forces and various kinds of vibrations.

To understand the flow mechanisms of those flexible and slender structures, as well as the control methods on flow past bluff bodies, field studies and wind tunnel experiments have commonly been conducted. However, the biggest problem of wind tunnel tests is the cost and time. In addition, for some micro and detailed flow visualizations, it is much more difficult to be identified by these experiments and field studies.

As the rapid development of computational technology and numerical techniques in the past several decades, Computational Wind Engineering (CWE) has been proved to be an alternative tool to wind tunnel test, which can analyse a lot of problems in the field of wind engineering.

Nowadays, detailed information of the complex, three-dimensional flow mechanisms on bluff structures can be obtained easily by conducting the computational numerical simulations. Thusly, safer, more durable and more economic structure designs can be put forward.

## 1.2 Problems statements and motivations

In recent years, with the increasing constructions of long-span bridges in the world, the length of main span is also growing. Cable-stayed bridge, as one of the forms of long-span bridges, has been widely adopted worldwide. Figure 1.1 shows an overview of Shanghai-Suzhou-Nantong Yangtze River Bridge, Hutong Bridge for short, which have been completed in July 2020. Ranking as the second longest cable-stayed bridge in the world at this time, the stay cable is of great important.



Figure 1.1 An overview of Hutong bridge

source: <https://structurae.net/en/structures/hutong-yangtze-river-bridge>

For a cable-stay bridge with over several hundred meters' span length, it is estimated that wind loads on the cables may be larger than that on the main elements, such as the pylon and girder (Hojo, Yamazaki, & Okada [1] ; Svensson [2] ). Although to the cable itself, the static wind load is not that important. However, when the static force was transferred to the deck or pylon, it becomes an important design factor.

Another important issue is about the vibration. It is reported that stayed cables suffer from much larger wind-induced vibrations under some certain circumstances. Rain-wind induced vibrations (RWIV) is one of the most severe problems, as its name suggests, which usually happens when it rains with high-speed wind.

Over the past decades, aerodynamic modifications have been introduced to disrupt the formation of water rivulets, leading to the suppression of rain-wind induced vibrations (RWIV), such as helical fillets, surface treatments including groove, dimple and pattern-indented one, etc. Researches into the modifications of surface treatments show that besides the purported ability to suppress RWIV, they also modestly reduce drag forces at design wind velocities. This is of interest to bridge designers, as the static force on the cable presents a significant design factor as the loads transfer to the main structure elements.

Cables with indented-patterned surface was firstly adopted on Tatara Bridge in Japan and later the Sutong Bridge in China. Miyata et al. [3] reported a minimum drag coefficient of 0.61 and a design drag coefficient of 0.7 for the Tatara Bridge. The similar drag reduction is also detected for the Sutong bridge. The overview picture of Tatara Bridge is shown in Figure 1.2.



Figure 1.2 An overview of Tataru Bridge, from Omishima Island, Japan

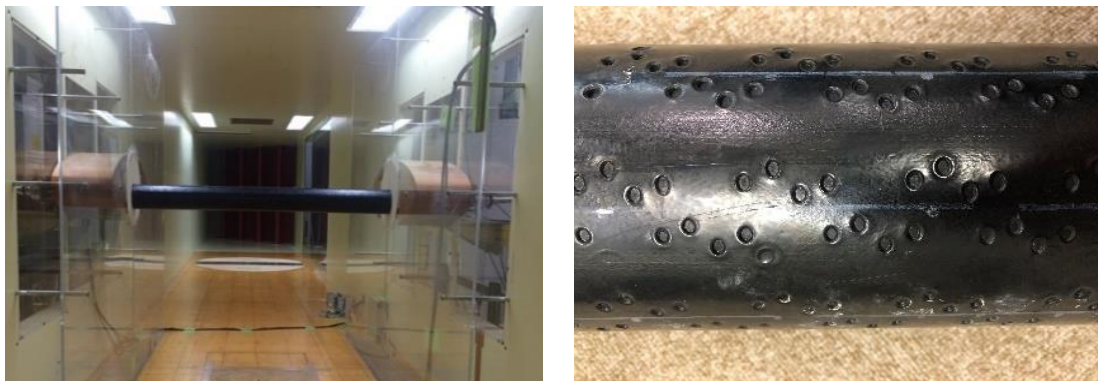


Figure 1.3 The pattern indented cylinder

Since its first use in Tataru bridge in 1999, the cylinders with pattern-indented surface have been subjected to some researches both in the field and in the wind tunnel test (Chen [4] ; Katsuchi and Yamada [5] ). Kleissl and Georgakis [6] conducted experiments on a yawed inclined cable and found that the flow transition was found to be independent of the relative cable-wind angle and only governed by the along-wind flow velocity. Iwazaki [7] compared indented cylinders with various patterns and the orientation of the indentations to the approaching flow. The wind tunnel test on cylinders with pattern-indented surface is shown in Figure 1.3.

Although the previous researchers have contributed significant investigations in this issue, a lot of problems remain to be explored. First of all, rare researches in numerical simulations are conducted to investigate the flow characteristics on the indented cylinder. Secondly, although the mechanism of dimpled or grooved cylinder is yet to be identified, that of the indented ones are remained to be discussed, such as the similarities and discrepancies between them. Ultimately, the various parameters of indentations, such as the width or depth, the indent location and different shape of indent, etc. still remain unknown.

### 1.3 Scope and objectives

On the basis of the above concerns, the current study on these curious issues was

conducted by using the numerical simulations. It is hopefully anticipated that the following objectives could be achieved by the current studies:

First of all, by investigating the flow characteristics on the indented cylinder, the mechanism on the drag mitigation of the indented cylinder could be revealed. Although the current cases are studied at a Reynolds number of a few thousand and the boundary layer was kept laminar, the results still could be adopted in the subcritical regime with for a wide range of  $Re$ . Moreover, the disclosed mechanism could offer some clues to the aerodynamic phenomena of indented cylinder at high Reynolds number. Thusly, this kind of aerodynamic modification could be used for other similar cylindrical structures in the future.

Secondly, the current thesis studied indentations with some design parameters, namely locations, sizes as well as the different shapes, etc. It is anticipated that the certain design optimizations of indentation may be disclosed for reducing the structural cost more efficiently.

Last but not least, by studying the flow past a circular cylinder with only one indentation, the results could be applied to other bluff bodies having a movable separation point, such as sphere or other curved objects.

## **1.4 Thesis layout**

The organization of this thesis is listed as follows.

In Chapter 1, a general introduction to the CWE skills, the current status of the usages and problems of indented cylinders as well as the objectives is presented. Then in Chapter 2, a detailed literature review starts from a summary of the aerodynamic and aeroelastic behaviors of a circular cylinder in wind engineering, followed by an introduction of various kinds of flow control methods. Chapter 3 gives a summary of the numerical methods to the current paper.

Chapter 4 to 7 show the main results: Chapter 4 addresses the first objective: Flows normal to a circular cylinder at Reynolds number equals to 3900 were simulated by means of large eddy simulation for verification and validation. Next, the flow past fully uniform-indented cylinders were simulated in Chapter 5. The mechanism of drag mitigation at high Reynolds for the indented cylinder are discussed by comparing to the dimpled and grooved ones, accessing the efficacy of the former one. In Chapter 6, characteristics of the flow around the half-indented cylinder are analyzed with respect to different indentation sizes and arrangements. Chapter 7 discussed the different flow mechanisms on two types of indentation with and without bump. Then some discussions on this topic are considered. At last, Chapter 8 presents some conclusions and prospects for future researches.

## Chapter 2 Literature Review

In this chapter, some main concepts and basic knowledge related to the current studies are presented by literature review. At the beginning, some examples with surface roughness as flow control approaches on both bluff-body and streamlined body aerodynamics are introduced. Then we focus on the field of bluff-body aerodynamics, i.e., circular cylinder. Some general concepts of flow around a smooth circular cylinder are introduced, such as the flow pattern, the impact (lift and drag forces) of the flow on it and the vortex-induced vibration are introduced. In addition, previous researches of flow past a roughened circular cylinder are also reviewed.

### 2.1 Surface roughness as flow control approach

The saguaro is a tree-like cactus species that can grow up to a height of 12 meters with a shallow taproot of up to 1 meter. Figure 2.1 shows an image of saguaros in Saguaro National Park in America. Founded only in the desert regions in US and Mexico, the saguaros are able to withstand very high wind velocities. The impact of those longitudinal cavities on the aerodynamics has been of great interest to biologist for a long time. Various parameters of this cacti-shape and the effect and mechanism to mitigate the drag force are studied by researchers so far, such as the  $h/D$  aspect ratio (the total height above ground/diameter of maximum cross-section of the cylinder) (Niklas and Buchman [8]), the number of cavities (Hodge [9]) and the depth of cavities (Geller and Nobel [10]), etc.



Figure 2.1 Saguaros in Saguaro National Park, southeastern Arizona, America

source: <https://www.nps.gov/sagu/index.htm>

Another surface roughness treatment is dimples. It is widely known that dimples of a golf ball could reduce dramatically the aerodynamic drag force of the ball. Figure 2.2 shows a model of golf ball with dimpled surface. By compared with a smooth sphere and spheres with sand-grain roughness, Bearman [11] found that the drag force



coefficient of a golf ball falls at a lower Reynolds number. After this fall the drag coefficient remains almost constant for the golf ball, whereas for the sand-roughened sphere it rises sharply after the minimum. Hence, the mitigation of drag coefficient in the postcritical regime caused by the dimpled surface is very effective. In the actual engineering field, the structures usually suffer from huge aerodynamic forces at this Reynolds number region, thusly drag decrease is very effective in reducing the cost.



Figure 2.2 A golf ball model

In comparison with the aforementioned bluff shape, i.e., cylinder and sphere, those with the generally streamlined structures in aerospace engineering have inherently slender shape (e.g., sailplane wings). Although the wings of sailplanes have extremely smooth surface to maintain the laminar airflow over the surface to minimize the drag force, the wing surface architecture of birds and sailplanes are, however, different as night and day.

The construction of the body surface of mammals which fly or swim in the water reduces the drag by change in boundary layer dynamics over the surface area of their body (Bechert et al. [12]). The wing surface of birds does not follow a single smooth curve surface. Feathers are a key adaptation that distinguishes wings of birds from other flying animals such as insects or bat. With a wing roughness height of 1-2% of chord length on the upper surface, the feathers of swift make their wings remarkably rough for their size. Lentink and de Kat's [13] aerodynamic analysis indicates that swifts attain laminar flow over their rough wings because their wing size is comparable to the distance the air travels (after a roughness-induced perturbation) before its transitions from laminar to turbulent. The effect of bio-Inspired surface roughness on airfoil is also investigated and studied for the past decades [14]

As introduced above, the above examples prove that the surface roughness could contribute to a better aerodynamic performance for some certain objects.

The indentation as an efficient flow control method has already innovated some applications. There must be more in the future.

## 2.2 Flow around a circular cylinder

Flow around a circular cylinder is a classical topic in the fluid mechanics. The reason of studying this problem lies in the following parts: Firstly, it is known that cylindrical

structures are widely used in offshore, marine and wind engineering. The applications include marine pipelines, bundles of marine risers, cables of long-span bridge, tall chimneys and towers, etc. It is of great importance to thoroughly understand the aero/hydro-dynamics for design. Secondly, flow past a circular cylinder is often used as a benchmark case to validate a new numerical method due to its simple configuration. Thusly we present general overview of the flow around a circular cylinder by reviewing the related literatures.

## Regime of flow

The non-dimensional quantities describing the flow around a circular cylinder are mainly dependent on the Reynolds number  $Re$ :

$$Re = \frac{DU}{\nu} \quad (2.1)$$

in which  $D$  is the diameter of the cylinder,  $U$  is the flow velocity, and  $\nu$  is the kinematic viscosity. The flow undergoes enormous changes as the Reynolds number is increased from zero. Figure 2.3 shows a definition sketch of the two different flow regions referred to various flow regime, namely the boundary layer and the wake region. The wake region is usually compared with the cylinder diameter,  $D$ . While the boundary layer extends over a very small thickness,  $\delta$ .

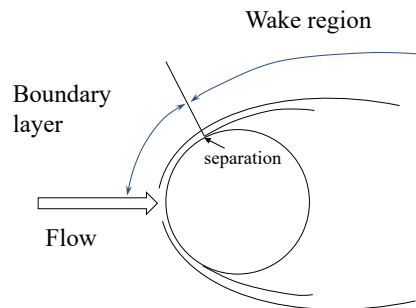


Figure 2.3 Definition sketch

The separation shown in Figure 2.3 doesn't occur for a very small  $Re$  and the first separation takes place in the range of  $5 < Re < 40$ , a fixed pair of vortices forms in the wake of the cylinder. The length of this vortex formation increases with  $Re$  (Batchelor [15]).

When the Reynolds number is further increased, the wake becomes unstable, which would eventually give birth to the phenomenon called vortex shedding in which vortices are shed alternately at either side of the cylinder at a certain frequency. For the range of the Reynolds number  $40 < Re < 200$ , the shedding maintains in two-dimensional form and it does not vary in the span-wise direction (Williamson [16]). As  $Re$  is increased in the range of  $200 < Re < 300$ , a transition to turbulence in the wake region occurs. And the region of transition to turbulence moves towards the cylinder with a further increase in  $Re$  (Bloor [17]). The laminar vortex shedding becomes distinctly three-dimensional in this range and the vortices are shed in span-wise direction.

The wake is completely turbulent while the boundary layer still remain laminar for a wide range of  $Re$ , namely  $300 < Re < 3 \times 10^5$ . This regime is known as the subcritical flow regime.

With a further increase in  $Re$ , the boundary layer itself transits from laminar to turbulence which only occurs at one side of the cylinder. Since the one side of boundary layer transits to turbulence while the other side remains laminar, this asymmetry causes a non-zero mean lift force on the cylinder. (Schewe [18] ; Rodríguez et al., [19] ; Lehmkuhl et al., [20] ). This flow regime is called as the critical one for a range of  $3 \times 10^5 < Re < 3.5 \times 10^5$ , accompanied by a significant drop in drag force.

The next Reynolds number regime is the named the supercritical flow regime. In this regime, the boundary layer transits from laminar to turbulence in both sides of the cylinder and the transition region is located somewhere between the stagnation point and the separation point. When the  $Re$  is further increased, the boundary layer becomes fully turbulent.

## Vortex shedding

One of the most important features of the flow regimes described above is the vortex shedding phenomenon, which occurs extensively over a wide range of Reynolds numbers. The mechanism of vortex-shedding phenomenon is detailed described by Gerrard [21] and is briefly reviewed in the following text.

For Reynolds numbers  $Re > 40$ , one vortex will grow larger than the other, owing to the instability of two vortices exposed to the small disturbances. The larger vortex fed by assumptive clockwise direction vorticity in the shear layer becomes strong enough to draw the opposing smaller vortex across the wake. In contrast, the vorticity in the smaller vortex is in the anti-clockwise direction. At some point, the approach of vorticity of opposite sign will cut off the further supply of vorticity to larger vortex, which is then shed as a free vortex. This process will continue to occur in an alternate manner between both sides of the cylinder, forming the so-called vortex shedding.

The vortex-shedding frequency, when normalized by the income flow velocity  $U$  and the diameter of cylinder  $D$ , can be expressed in a non-dimensional form as:

$$St = \frac{f_v D}{U} \quad (2.2)$$

in which  $f_v$  is the vortex-shedding frequency.

The normalized vortex-shedding frequency, namely  $St$ , is called the Strouhal number. The Strouhal number, which is stable at around 0.2 in the subcritical regime.

## Pressure and force coefficients

The surface pressure can be expressed by  $C_p$ , which is non-dimensional pressure coefficient:

$$C_p = \frac{p - p_0}{0.5 \rho U^2} \quad (2.3)$$

in which  $p$  represents the local pressure and  $p_0$  is the reference upstream pressure; the term  $0.5\rho U^2$  represents the dynamic pressure.

The drag force and lift force ( $F_d, F_l$ ) can be described in terms of non-dimensional lift and drag coefficients ( $C_d, C_l$ ) as:

$$C_d = \frac{2F_d}{\rho D U^2 L} \quad (2.4)$$

$$C_l = \frac{2F_l}{\rho D U^2 L} \quad (2.5)$$

in which  $L$  is the span-wise length of the cylinder.

Throughout the subcritical Reynolds numbers ( $300 < Re < 3.5 \times 10^5$ ), a practically constant value of 1.0 are assumed for the mean drag force coefficient  $C_d$  (Zdravkovich [22]). When  $Re$  reaches the value of  $3.5 \times 10^5$ , a dramatic drop occurs and  $C_d$  decreases to a much lower value in the supercritical regime ( $3.5 \times 10^5 < Re < 1.5 \times 10^6$ ). This phenomenon is so-called drag crisis. However, there is no general consensus on the value of the lift coefficient (Norberg [23]). This is due to the flawed correlation in span-wise direction which can change the lift force greatly.

## 2.3 Previous studies of a cylinder with rough surface

For a smooth circular cylinder, the boundary layer turns from laminar to turbulent at critical Reynolds number. The empowered boundary layer with higher momentum can against the adverse pressure gradient and delays the main separation. The conception of energizing the boundary layer and delay the separation has bred several kinds of methods, including surface roughness, dimples, grooves, ridges and indentations, etc. In the following text, we will go through a detailed tour of these flow control methods.

### Sand roughness

Surface with sand roughness is one of the important influencing factor on flow-induced pressure and associated forces. The effect of sand roughness as flow control method has been widely investigated by a lot of researchers. Figure 2.4 depicts  $C_d$  plotted as a function of  $Re$  and surface roughness  $k/D$ , where  $k$  is the thickness of roughness elements (Achenbach and Heinecke [24]).

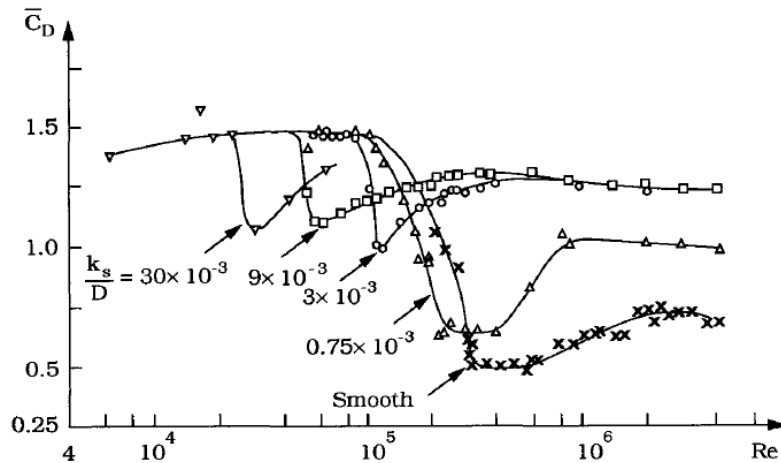


Figure 2.4 Drag coefficient of a circular cylinder at different surface roughness (Achenbach and Heinecke, 1981)

By conducting the wind tunnel tests, Achenbach concluded that rougher the surface, the lower the critical Reynolds number, but the smaller the fall in drag force. This behavior is resulted in the early transition to turbulence in the boundary layer with increasing roughness. The drag crisis is not as extensive as that in the smooth cylinder. The drag recovers rapidly in the post-critical regime and exhibits a higher drag force than the smooth one. This feature is directly linked with the separation angle, which is investigated at the earlier researches of Achenbach [25]. In the supercritical regime, the roughness thickens the turbulent boundary layer which results in a weaker momentum exchange near the wall, and thusly the separation occur earlier, and then the drag coefficient rises.

Although the surface sand roughness could reduce the drag force at a lower critical Reynolds number, it is only effective in a narrow range of  $Re$ . Moreover, the drag force recovers to a higher value than the smooth cylinder in the post-critical regime, making it not effective for a large flow velocity. In actual cases, most of the structures suffer from huge aerodynamic force at post-critical regime, thus it is debatable whether the surface sand roughness is an economical method or not.

## Dimpled cylinder

As introduced in the former Chapter, Golf ball travels far owing to the dimples on the surface. Dimples are proved to have effects on reduce the drag force of the circular cylinder.

Kimura and Tsutahara [26] studied the effect of a golf ball's dimples by a two-dimensional model, a circular-arc groove on the surface of a circular cylinder, at Reynolds numbers of about a few thousand. By studying several types of grooves with different positions, they concluded that the grooves are most effective at a position of about 80deg and there is closed circulating flow over the cavity.

Prompted by the researches of Kimura and Tsutahara, wind tunnel tests on a dimpled

circular cylinder over the Reynolds number from  $2 \times 10^4$  to  $3 \times 10^5$  were conducted by Bearman and Harvey [27]. It is reported that the drag force of the dimpled cylinder doesn't rise to high values as cylinders with sand-roughness but is found to be closer to that for a smooth cylinder in the post-critical regime. However, the dimple used in their studies were modeled on those found on a typical golf ball. Thusly they also suggested that a larger reduction in drag might be obtained with different design and arrangements of dimples.

In the sub-critical regime ( $7.43 \times 10^3$  to  $1.798 \times 10^4$ ), Zhou et al. [28] conducted the experiments on the flow past a circular dimpled cylinder with various dimple arrangements, i.e., half dimpled and fully dimpled. Their study revealed that even in the sub-critical regime, the cylinder covered with dimples uniformly over the total surface could also produce a drag reduction of about 10%. Among the different dimple arrangements, the “dimple half forward” cylinder depicted the lowest drag force.

The main difference between the dimples and the sand-roughness is the size. The dimples have spherical shape and are much larger than ordinary roughness scales. Hence, by considering drag coefficient values, it appears that especially in the postcritical regime the dimples have a more beneficial effect on the flow development than sand roughness.

## **Grooved cylinder**

The axially grooves also hold similar effect on mitigating the drag force at certain Reynolds numbers. Motivated by the Saguaro species of cacti, flow past cactus-shaped cylinders at Reynolds numbers of 20, 100 and 300 has been studied by Babu and Mahesh [29] with direct numerical simulation. It is reported that the grooves reduce viscous drag force significantly at low Reynolds number and the grooves only have effects on the near-surface fields rather than the free-stream field.

A comparative study of the wakes behind cylinders with grooved and smooth surfaces has been performed at a sub-critical Reynolds number of 1500 by Liu et al. [30] They concluded from the experiment results that the length of the recirculation zone behind the grooved cylinder was extended by nearly 18.2%, yet the longitudinal velocity fluctuation intensity was considerably weakened.

Comparison of flow past a circular cylinder with smooth, grooved and dimpled surface has been investigated by Zhou et al. [31] in an open channel and a towing tank. In their study, a wide range of Reynolds numbers has been taken into consideration ( $7.4 \times 10^3$  to  $8 \times 10^4$ ). They revealed that the strength of vortex shedding from the cylinder becomes weaker due to the effect of grooved or dimpled surfaces, as indicated by a smaller and narrower wake than that of the smooth cylinder.

As the grooves can help to reduce the drag force at a lower Reynolds number, the design parameters of the grooves on the cylinder surface have also been studied by a large number of researchers.

Oki, Aoki and Nakayama [32] studied the flow characteristics for grooves' depth of a grooved cylinder by applying the unsteady RNG simulation. They found out that the

deeper the groove, the lower the critical Reynolds number. Meanwhile, the minimum drag force is also larger for the deep grooves. The shape and number of grooves on the cylinder surface have been studied by Yamagishi, Kimura and Oki [33] . Their works identified that for grooves with same depth, triangle one is more effective than arc one in drag mitigation. More grooves on the circumference of cylinder result in lower critical Reynolds numbers, while minimum drag force does not vary with the different number of grooves.

## Chapter 3 Methods

Computational Wind Engineering, has developed quickly in past several decades along with revolutionary. CWE covered wide and various studies: from flow past a bluff body to fluid-structure interaction; from a tiny scale to an atmospheric scale; from one single element to complex structures; from structural cases to environmental problems. In the current study, large eddy simulation is adopted for a relatively high Reynolds number. In this chapter, the governing equations, discretization schemes and solution algorithms will be briefly introduced.

### 3.1 Governing equations

The LES equations comes from the time-dependent filtered incompressible Navier-Stokes equation:

$$\frac{\partial \bar{u}_i}{\partial x_i} = 0 \quad (3.1)$$

$$\frac{\partial \bar{u}_i}{\partial t} + \frac{\partial \bar{u}_i \bar{u}_j}{\partial x_j} = -\frac{1}{\rho} \frac{\partial \bar{p}}{\partial x_i} + \frac{\partial}{\partial x_j} \left[ \nu \left( \frac{\partial \bar{u}_i}{\partial x_j} + \frac{\partial \bar{u}_j}{\partial x_i} \right) + \tau_{ij} \right] \quad (3.2)$$

$$\tau_{ij} = \overline{u_i u_j} - \bar{u}_i \bar{u}_j \quad (3.3)$$

where  $\nu$  is the kinematic viscosity,  $\bar{u}$  and  $\bar{p}$  are the filtered velocity and pressure, respectively. Eq. 3.3 is termed the sub-grid scale (SGS) stress which requires modeling. The SGS stress  $\tau_{ij}$  is expressed according to the Boussinesq approximation.

In modeling of subgrid-scale turbulent stress, some different approaches are widely used, including the eddy viscosity model (Smagorinsky [34]), the dynamic model (Germano et al. [35]) and dynamic  $k$ -equation model (Fureby et al., [36]).

LES method needs a much-refined grid resolution in all directions, especially in the wall bounded flows at high Reynolds number. It results in both high temporal resolution and quite a long time in integration to get an ensemble averaged result. LES is thusly much more computationally expensive than RANS.

### 3.2 Discretization

Discretization aims to transform the continuous governing equations to a set of discrete algebraic expression, which can be solved by iterative or certain direct methods. This procedure consists of the equations as well as the discretization of the solution domain, these two parts.

As for the spatial domain discretization, the methodology of FVM (Finite Volume Method) is used in OpenFOAM. By this method, the fluid domain will be separated into several regions (in a finite number) which is named as control volumes. These



control volumes fill the solution domain without overlap.

When transient problems are being solved, time should also be discretized. Then, a specified time step is determined from the beginning to the end of calculation.

Another one is the discretization of equation. The Gauss theorem is adopted here. Think about a nonexclusive type of transport equation for a scalar property  $\phi$ :

$$\frac{\partial \phi}{\partial t} + \nabla \cdot (\mathbf{U}\phi) - \nabla \cdot (\gamma \nabla \phi) = S(\phi) \quad (3.4)$$

Integration of Equation 3.4 over a certain control volume  $V_P$  and time-step  $\Delta t$  gives:

$$\int_{\Delta t} \left[ \frac{\partial}{\partial t} \int_{V_P} \phi dV + \int_{V_P} \nabla \cdot (\mathbf{U}\phi) dV - \int_{V_P} \nabla \cdot (\gamma \nabla \phi) dV \right] dt = \int_{\Delta t} \int_{V_P} S(\phi) dV dt \quad (3.5)$$

where  $U$  indicates the velocity vector and  $S(\phi)$  is the source term. The convection term is discretized by:

$$\begin{aligned} \int_{V_P} \nabla \cdot (\mathbf{U}\phi) dV &= \sum_f \mathbf{S} \cdot (\mathbf{U}\phi)_f \\ &= \sum_f \mathbf{F} \cdot (\mathbf{U}\phi)_f \end{aligned} \quad (3.6)$$

in which  $\mathbf{S}$  is the surface area vector,  $\mathbf{F}$  is the mass flux through each of the surface surrounding the control volume and this worth requires exceptional treatment, as will be explained in the following part.  $\phi_f$  is the variable value on the center of surfaces. It is gotten by utilizing some certain convection differencing scheme.

In this thesis, *Gauss limitedLiner*, one of the TVD (Total Variation Diminishing) schemes is adopted for the convection differencing. The details of this scheme won't be introduced here, intrigued reader may refer to the related references (Versteeg and Malalasekera [37]).

The diffusion term is treated likewise as the convection:

$$\begin{aligned} \int_{V_P} \nabla \cdot (\Gamma \nabla \phi) dV &= \sum_f \mathbf{S} \cdot (\Gamma \nabla \phi)_f \\ &= \sum_f \Gamma \mathbf{S} \cdot (\nabla \phi)_f \end{aligned} \quad (3.7)$$

in which  $(\nabla \phi)_f$  is obtained by the gradient scheme specified in the *fvschemes* file and *Gauss linear* is used in the current simulation. Exceptional consideration ought to be considered for the orthogonality problem. Some possible correction methods are offered by Jasak [38].

The source term is discretized as:

$$\int_{V_P} \mathbf{S} \cdot (\phi) dV = \mathbf{S}_p V_P \quad (3.8)$$

The last discretization is time. In this study, an implicit and second-order time scheme called *backward* is used. It is defined as:

$$\frac{\partial \phi}{\partial t} = \frac{\frac{3}{2} \phi^n - 2\phi^o + \frac{1}{2} \phi^{oo}}{\Delta t} \quad (3.9)$$

where  $\phi^n$  is the variable value at next time,  $\phi^o$  and  $\phi^{oo}$  are the old and second old" times, respectively.

Now, the entire discretization process is done, bringing about the fully discretized transport equation as Equation 3.10:

$$\frac{\frac{3}{2}\phi^n - 2\phi^o + \frac{1}{2}\phi^{oo}}{\Delta t} V_P + \sum_f \mathbf{F}\phi_f^n - \sum_f \Gamma \mathbf{S} \cdot (\nabla\phi)_f^n = \mathbf{S}_P V_P \quad (3.10)$$

### 3.3 Matrix solvers

The N-S equations are discretized by the procedures described in the previous section, resulting in a system of algebraic system. While the direct methods like Gauss elimination, LU decomposition are theoretically applicable to any matrix, in most CFD applications iterative methods are adopted due to its higher efficiency.

In the current study, the *GAMG* solver (generalised geometric-algebraic multi-grid solver), together with Gauss-Seidel smoother is adopted for the pressure equation. *PBiCG* (preconditioned bi-conjugate gradient solver) for asymmetric matrices was adopted to calculate equations of  $k$  and velocity.

### 3.4 Solution procedures

The flow is driven by the pressure gradient without other source term, which is presented in Equation 3.2. Together with the non-linearity and the couple of the mass and momentum conservation equations, this forms the solution of the N-S equation.

Substitute  $\phi$  with  $\mathbf{U}$  in Equation 3.6 gives the non-linear term  $\nabla(\mathbf{U}\mathbf{U})$ , which means velocity being transported by itself. Due to the complexity and large computational resource required by the non-linear solver, this term is conventionally linearized to forward computation.

The non-linear term is discretized as:

$$\begin{aligned} \int_{V_P} \nabla \cdot (\mathbf{U}\mathbf{U}) dV &= \sum_f \mathbf{S} \cdot \mathbf{U}_f \mathbf{U}_f \\ &= \sum_f \mathbf{F}\mathbf{U}_f \\ &= a_P \mathbf{U}_P + \sum_N a_N \mathbf{U}_N \end{aligned} \quad (3.11)$$

in which the subscript  $N$  denotes the center of neighboring control volumes.  $a_P$  and  $a_N$  s are a function of  $\mathbf{U}$ . Linearisation of the convection term implies that an existing velocity (flux) field that satisfies the continuity Equation 3.2 will be used to calculate  $a_P$  and  $a_N$  s.

Equation 3.10 could be reconstructed to take as:

$$a_P \mathbf{U}_P = \mathbf{H}(\mathbf{U}) - \nabla p \quad (3.12)$$

where  $\mathbf{H}(\mathbf{U})$  consists of the source part of the transient term and the contribution of the convection and diffusion from the neighboring control volumes.

Take the divergence of Equation 3.12 and noting the continuity Equation:

$$\nabla \cdot \left( \frac{1}{a_p} \nabla p \right) = \nabla \cdot \left( \frac{\mathbf{H}(\mathbf{U})}{a_p} \right) \quad (3.13)$$

Integration of Equation 3.13 over a control volume gives:

$$\sum_f \mathbf{S} \cdot \left[ \left( \frac{1}{a_p} \right)_f (\nabla p)_f \right] = \sum_f \mathbf{S} \cdot \left( \frac{\mathbf{H}(\mathbf{U})}{a_p} \right)_f \quad (3.14)$$

The above equation together with 3.12 are the final form of the discretised incompressible Navier-Stokes system.

Now, we are going to move to the solution procedure of the discretized N-S equations. Solver called *pimpleFoam* is used in this study, which is a variant of the PISO (Pressure Implicit with Splitting of Operator) algorithm. According to Jasak [38] the main procedure of the PISO algorithm could be summarised as:

1. Determine the boundary conditions;
2. Solve the discretized momentum to compute an intermediate velocity field;
3. Compute the mass fluxes at the cell faces;
4. Calculate the pressure;
5. Correct the value from step 3;
6. Correct the velocities based on the new pressure results;
7. Renew the boundary conditions;
8. Move to the next time-step and calculate from 1 again.

The difference between the PIMPLE algorithm and the conventional PISO lies in the determined iteration numbers of the PISO procedure. The main part of the source code in the *pimpleFoam.C* is shown as:

```
Info<< "Time = " << runTime.timeName() << nl << endl;
// --- Pressure-velocity PIMPLE corrector loop
while (pimple.loop())
{
#include "UEqn.H"
// --- Pressure corrector loop
while (pimple.correct())
{
#include "pEqn.H"
}
if (pimple.turbCorr())
{
turbulence->correct();
}
}
```

}

The above algorithm is controlled by two parameters:

*nOuterCorrectors*, which specifies the outer-iteration numbers (the PISO algorithm).  
*nCorrectors* specifies the pressure corrections times inside the above PISO algorithm.  
In the file called *fvSolution*, the above parameters are defined.

In the current simulation, *nOuterCorrectors* is set to be 3 and *nCorrectors* is set to be 2. This setting is employed to yield stable and accurate results since a larger time-step is set, as shown in the next Chapter.

# Chapter 4 Simulation on Flow Past a Circular Cylinder

3D simulation of the flow past a smooth circular cylinder is a fundamental and essential case in wind engineering for verification and validation (AIAA 1998) in CWE. In a process of verification, the errors in simulation due to numerical modeling are estimated and reduced. While in the validation process, the assessments are done between the simulated cases and experimental data. Thusly, the flow characteristics by simulation can be identified. In the current study, 3-D simulations of flows perpendicular to a circular cylinder at  $Re = 3900$ . The verification and validation are assessed by LES.

## 4.1 Geometry and mesh

A schematic view of a circular flow field domain around a circular cylinder with a diameter  $D$  ( $D$  equals to 110mm in this study) is shown in Figure 4.1. The fluid domain has a same extension of  $40D$  both in stream-wise and cross-stream direction.

As for the spanwise direction, most authors used the length  $L_z = 3.14D$  discretized by 48 computational nodes to simulate the flow past a smooth circular cylinder (Mittal and Moin [39] ; Parnaudeau et al. [40] ; Lysenko, Ertesvåg, and Rian [41] ). It was found by Kravchenko and Moin [42] and Breuer [43] that doubling the cylinder span from  $\pi D$  to  $2\pi D$  and keeping the span-wise resolution did not change the results so much. It was revealed by Lehmkuhl et al. [44] that regarding the span-wise size of the domain, for Reynolds numbers smaller than  $6.5 \times 10^5$  a length of  $L_z = 0.5\pi D$  was enough to capture the largest scales of the flow.

In the light of these results, in this study, two cases span-wise extension  $L_z = 3.14D$  (48 grids in span-wise direction) and  $L_z = 2D$  (36 grids) were simulated in order to identify the effect of aspect ratio on the simulation results.

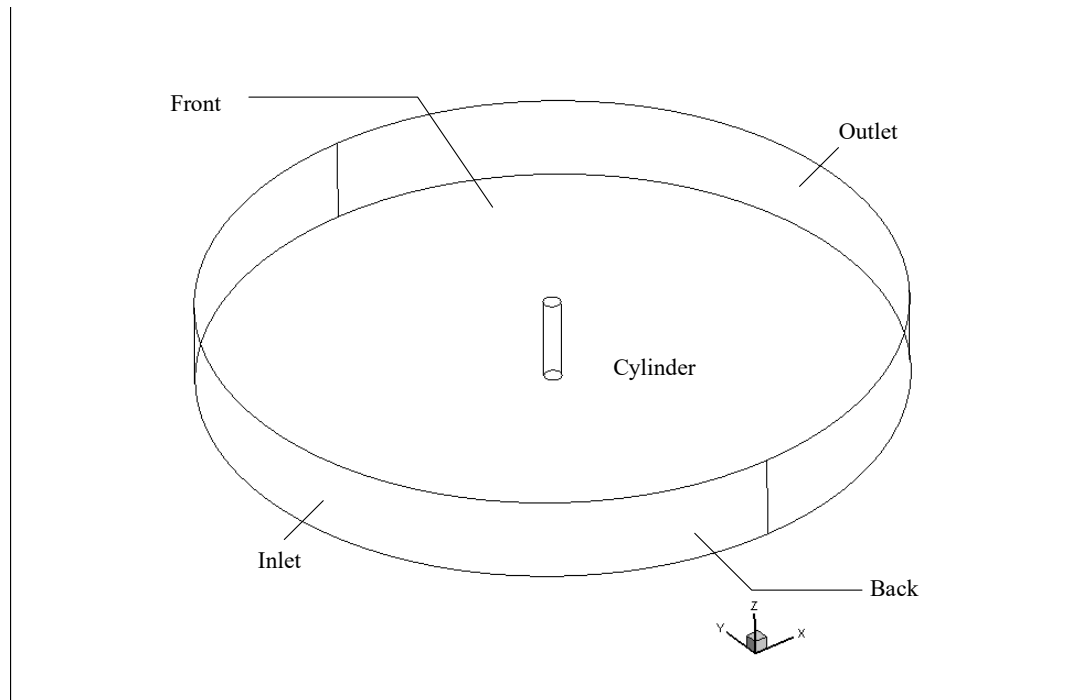


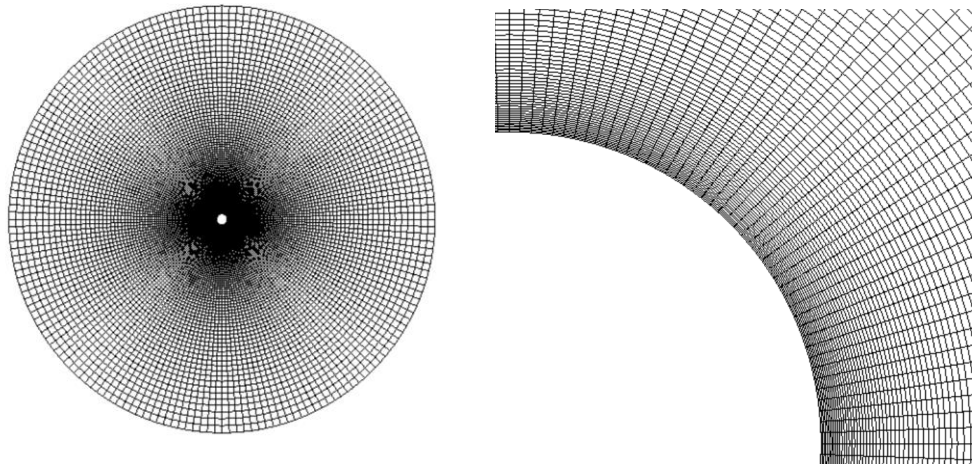
Figure 4.1 Schematic of the fluid domain

Table 4.1 Mesh dependency test.

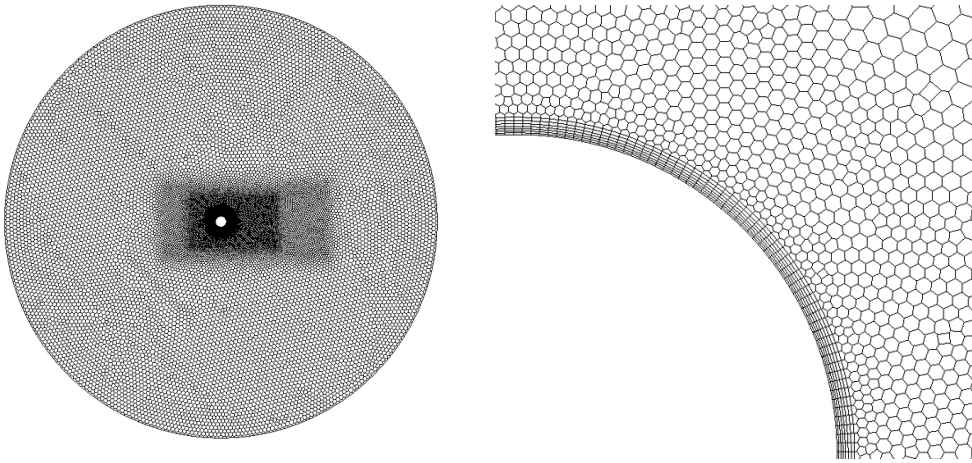
No.	Domain	Grid	Cells
A1	40D × 3.14D	180 × 180 × 50	1080000
A2	40D × 3.14D	160 × 160 × 50	960000
B1	40D × 2.0D	180 × 180 × 40	864000
B2	40D × 2.0D	160 × 160 × 40	768000
C	40D × 2.0D	/	1040000

Table 4.1 presents the 5 cases for the mesh dependency test at  $Re = 3900$ . Among them, Case As and Bs are structured hexahedral meshes with different span-wise extension and grid refinements. Case C is unstructured polyhedral mesh which has the same span-wise extension with Case Bs. This is to identify the effect of mesh shapes on the simulation results, since the cases in following study is based on the polyhedral meshes.

For all the cases, the first cell at the wall of the cylinder was positioned with a size of  $0.0025D$  to meet the requirement of  $y_+ \Delta$  smaller than 1. The spacing ratio for structured cases is less than 1.05 to avoid an abrupt change of cell sizes. The meshing for the whole domain and near the cylinder for both structured and unstructured cases are presented in Figure 4.2.



(a) Structured Mesh



(b) Unstructured Mesh

Figure 4.2 Computational grid

## 4.2 Numerical methods

### 4.2.1 Numerical characteristics

During the simulation, non-dimensional time  $t^*$  is defined as

$$t^* = \frac{U}{D} t \quad (4.1)$$

in which  $t$  is the real time. A non-dimensional time of 1 equals to the time for the flow in streamwise direction to pass along the circular cylinder diameter.

The time-step is firstly decided by the condition  $\max Co < 2$  (where  $\max Co$  stands for the maximum courant number during the simulation) in a pre-run and then kept fixed during the time integration.

In general, for each case statistics are compiled over periods of at least 200 non-dimensional seconds, or about 40 vortex shedding cycles to obtain the mean flow variables after a pre-run of 100 non-dimensional seconds.

## 4.2.2 Boundary conditions

At the inlet, the constant velocity  $u=1$  m/s along the x-axis were set up. The outlet was positioned by 20D downstream of the cylinder for a fully developed flow.

The no-slip condition is employed on the wall boundary, which is the surface of cylinder. The no-slip condition means that a zero-tangential velocity are on the wall. Periodicity is enforced in the span-wise direction of the cylinder.

## 4.3 Verification using 3-D LES

### 4.3.1 Force coefficients

Table 4.2 Force coefficients and Strouhal No.

No.	$C_d$	$C_{l, rms}$	$St$
A1	1.036	0.218	0.209
A2	1.032	0.205	0.212
B1	0.991	0.139	0.209
B2	0.999	0.146	0.213
C	0.987	0.123	0.207

Table 4.3 Experimental and numerical works of flow past a circular cylinder at  $Re=3900$

Contributors	Method	$C_d$	$C_{l, rms}$	$St$
Lourenco and Shih[45]	Experiment	0.99		0.22
Norberg[46] [47]	Experiment	0.98	0.04-0.15	
Parnaudeau et al.[40]	Experiment			0.208
Mittal and Moin[39]	LES	1.00		0.21
Breuer[43]	LES	1.02		0.22
Lysenko et al.[41]	LES	0.97	0.09	0.209
Kravchenko andMoin[42]	LES	1.04		0.21

Table 4.2 presents the force coefficients and  $St$  (Strouhal number) of five cases. Table 4.3 presents the force coefficients and Strouhal No. from available experimental and numerical (LES) results. Regarding to the average drag, the maximum difference among the five cases (A1 and C) is less than 5%. Most of the results from references shown in Table 4.3 are between 0.97 to 1.04, which have a good agreement with the previous studies. The r.m.s. fluctuating lift force coefficients various among five models, the values are between 0.12 to 0.22, which is also closed to the references. However, the lift coefficients of the cases with aspect ratio of 3.14D (cases As) is slightly higher than the 2D cases. The Strouhal number determined from a Fast Fourier transform of



the  $C_l$  time signal of all of the five cases were around 0.207 to 0.213. This value was in good agreement with the experimental predictions by Parnaudeau et al. [40] ( $St = 0.208$ ) and LES numerical simulations by Lysenko et al. [41] ( $St = 0.209$ ).

Figures 4.3 to 4.12 presents the spatial-temporary distribution of the force coefficients. The horizontal axis represents the non-dimensional time and the vertical axis is the span-wise size of cylinder. The vertical axis is standardized by the diameter of cylinder.

Compared to the cases with 3.14D spanwise aspect ratio, the results of cases with 2D spanwise aspect ratio do not show a big discrepancy. All the five cases show 3-D characteristics, which can be observed in both the time history of force coefficients as well as the spatial-temporal distribution.

In Figure 4.11, one can observe that the force in case C (unstructured mesh) have a weaker correlation along the cylinder length. The lower spatial correlation leads to small magnitudes of spaced-averaged force coefficients in Figure 4.12. This is due to the difference mesh refinement in spanwise direction which has a strong relation with the partially correlated flow structures along the cylinder axis. Compared to the structured mesh in Case As and Bs with 48 grid in spanwise direction, the grid number in unstructured mesh in case C is much larger, therefore a finer mesh in the refinement may contribute to a weaker spatial correlation.

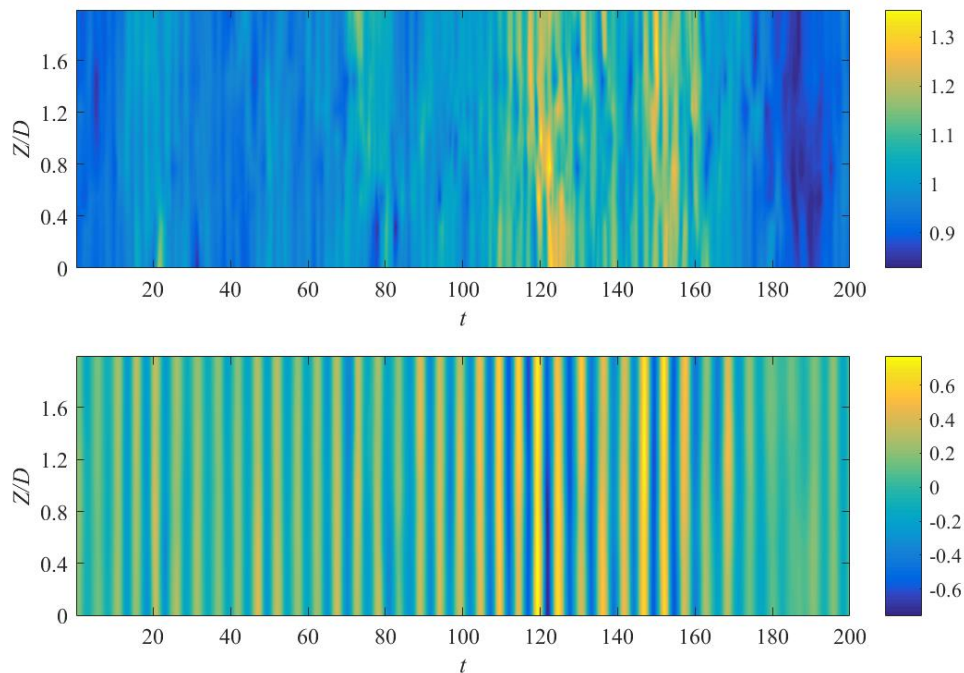


Figure 4.3 Spatial-temporal distribution of force coefficients (Case A1)  
(upper figure,  $C_d$  ; lower figure,  $C_l$ )

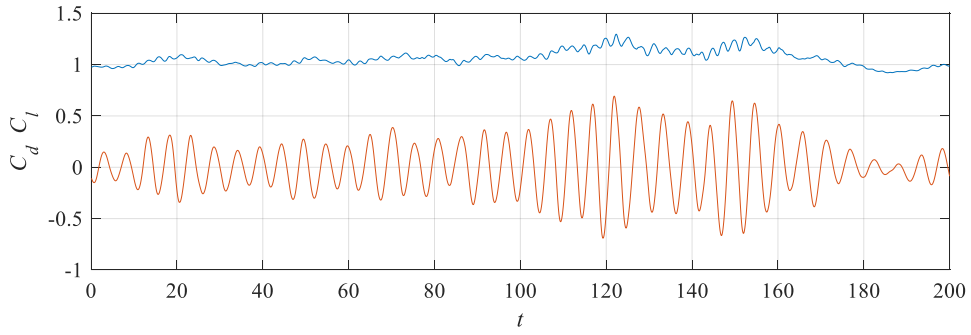


Figure 4.4 Space-averaged force coefficients (Case A1)  
(upper curve,  $C_d$  ; lower curve,  $C_l$ )

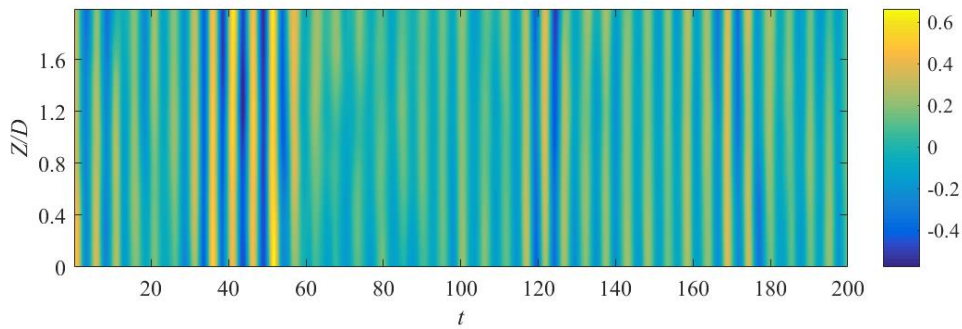
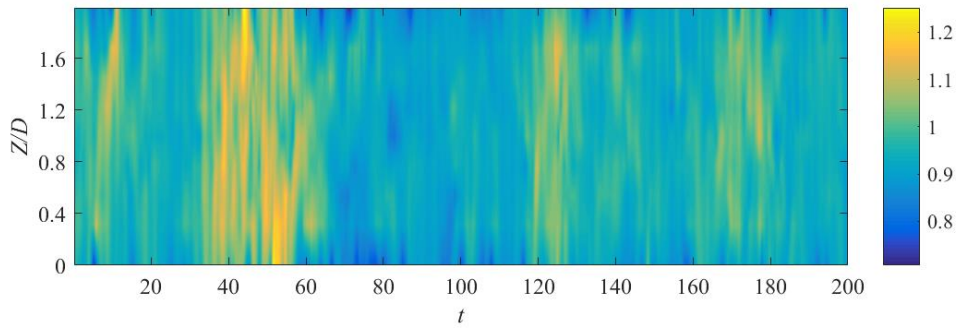


Figure 4.5 Spatial-temporal distribution of force coefficients (Case A2)  
(upper figure,  $C_d$  ; lower figure,  $C_l$ )

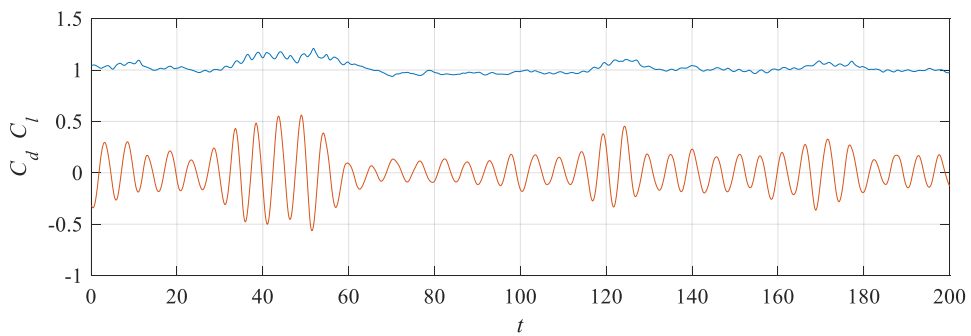


Figure 4.6 Time histories of force coefficients (Case A2)  
(upper curve,  $C_d$  ; lower curve,  $C_l$ )

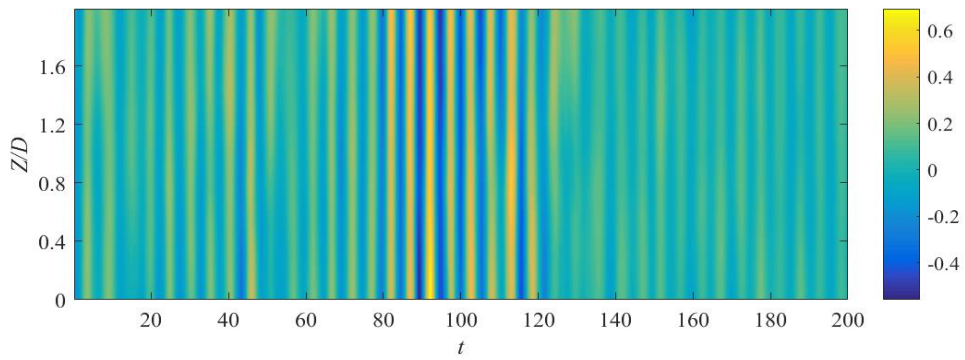
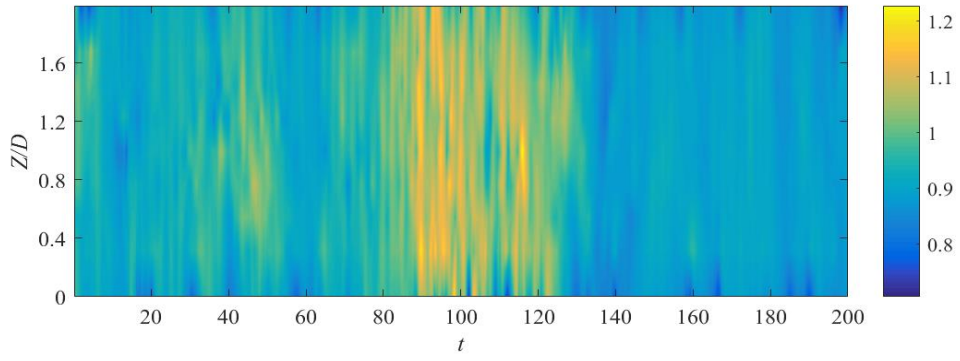


Figure 4.7 Spatial-temporal distribution of force coefficients (Case B1)  
(upper figure,  $C_d$  ; lower figure,  $C_l$ )

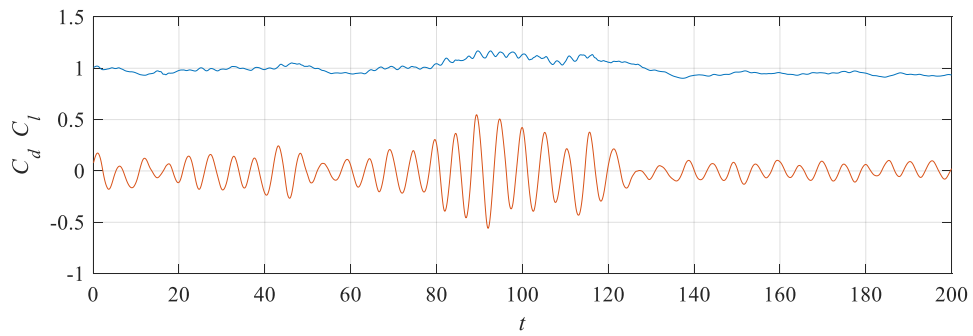
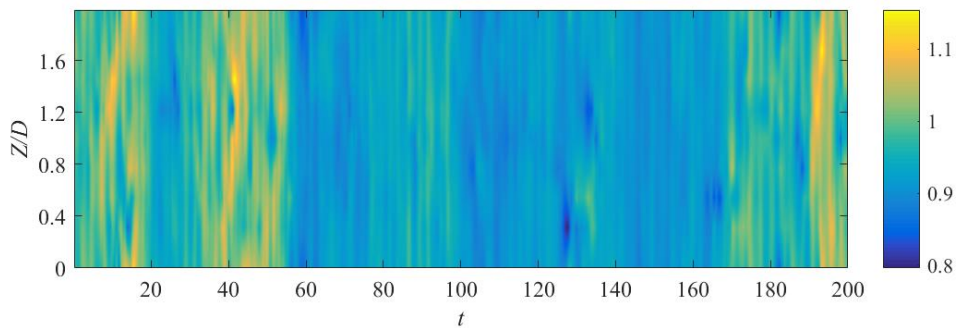


Figure 4.8 Time histories of force coefficients (Case B1)  
(upper curve,  $C_d$  ; lower curve,  $C_l$ )



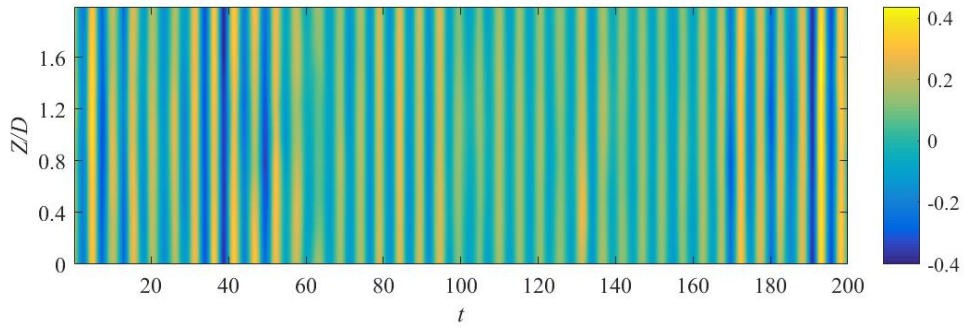


Figure 4.9 Spatial-temporal distribution of force coefficients (Case B2)  
(upper figure,  $C_d$  ; lower figure,  $C_l$ )

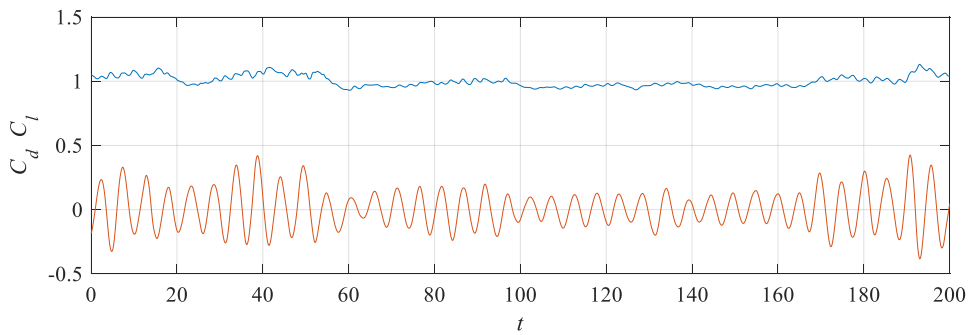


Figure 4.10 Time histories of force coefficients (Case B2)  
(upper curve,  $C_d$  ; lower curve,  $C_l$ )

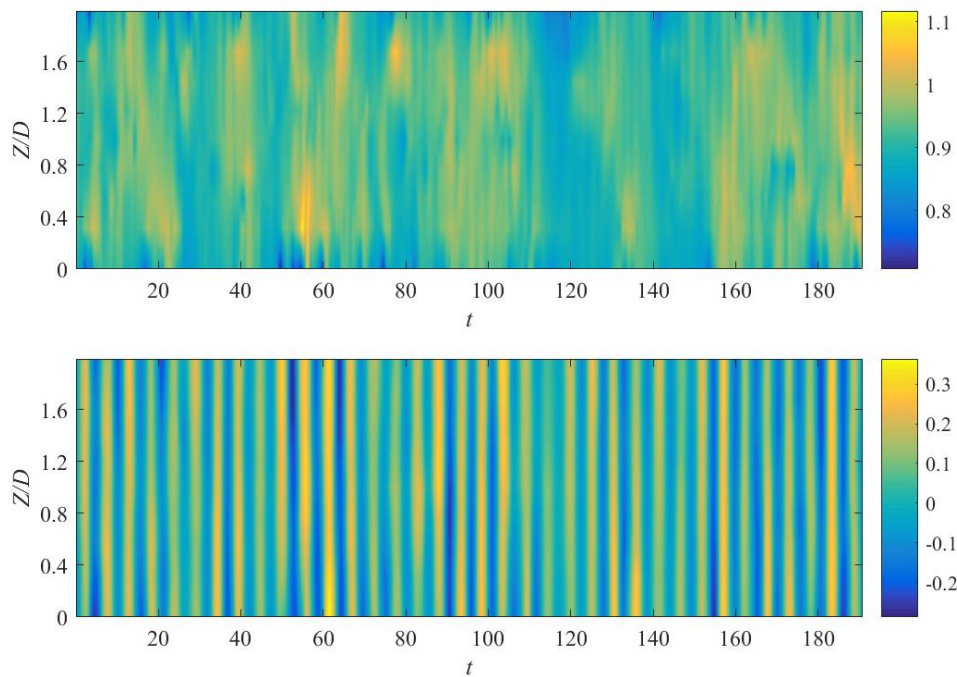


Figure 4.11 Spatial-temporal distribution of force coefficients (Case C)  
(upper figure,  $C_d$  ; lower figure,  $C_l$ )

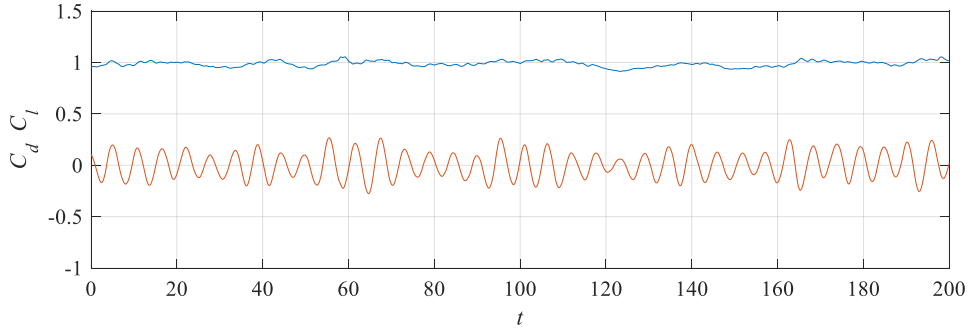


Figure 4.12 Time histories of force coefficients (Case C)  
(upper curve,  $C_d$  ; lower curve,  $C_l$ )

### 4.3.2 Pressures on cylinder surface

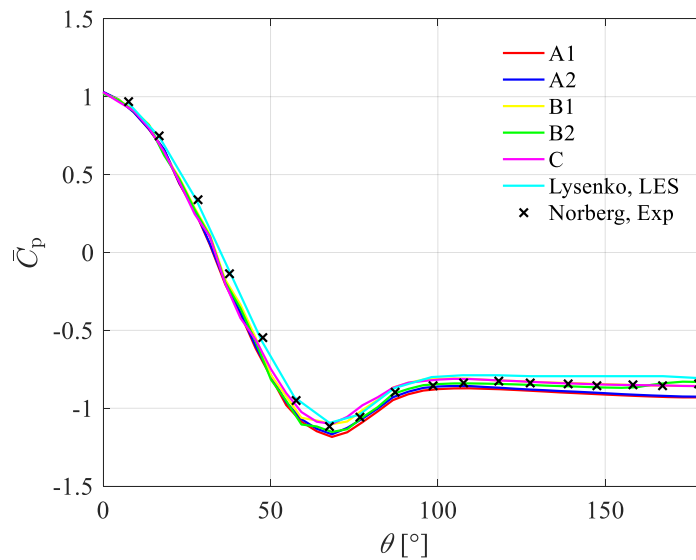


Figure 4.13 Time-averaged pressure coefficients on the cylinder surface

The distribution of pressure on the circular cylinder was further investigated according to the different span-wise length and grid refinements of the cylinders.

Figure 4.13 shows the time-averaged pressure coefficients of the cylinder circumference of five cases, LES work done by Lysenko et al. [41] and Experimental work done by Norberg [46] .

Distribution of the mean pressure coefficients in the five cases were slightly different from each other. Both trend and value of all the cases are in good agreements with references. At angle over  $100^\circ$ , there are some deviations between the Case Bs and LES done by Lysenko et al. [41] . However, the maximum deviations of the pressure coefficients on backward side of the cylinders is also limited with a value of around 4.5%.

### 4.3.3 Velocity distribution

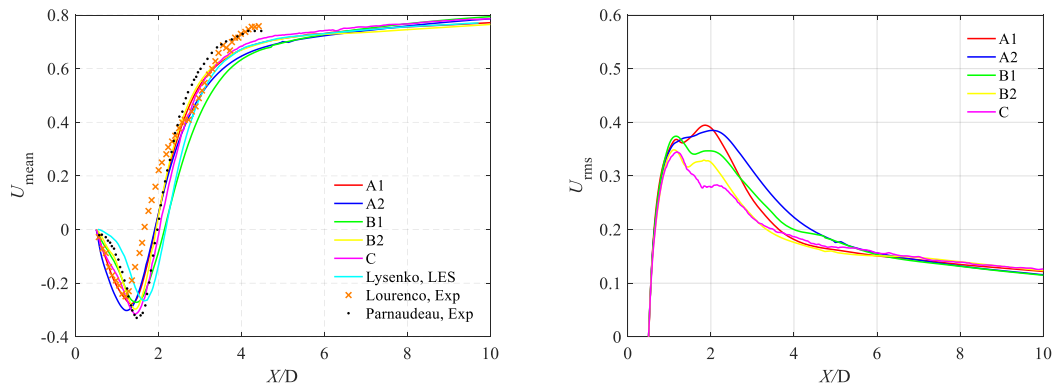


Figure 4.14 Mean stream-wise and r.m.s. velocity along wake center line

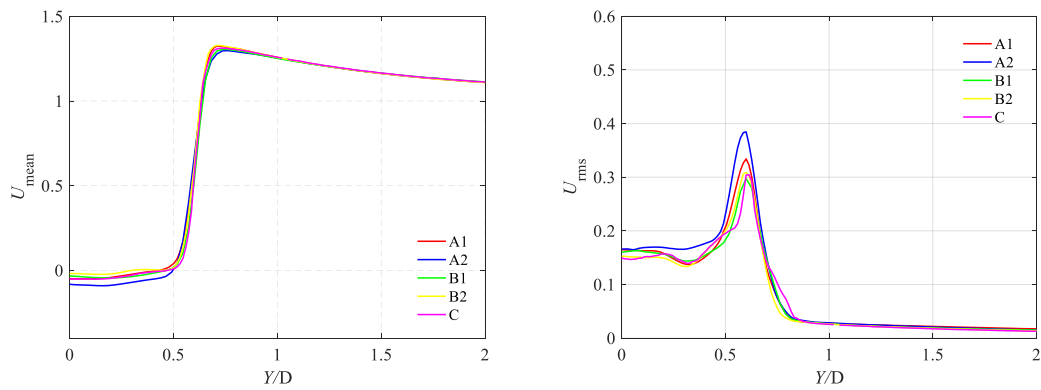


Figure 4.15 Mean stream-wise and r.m.s. velocity at  $x/D=0.6$

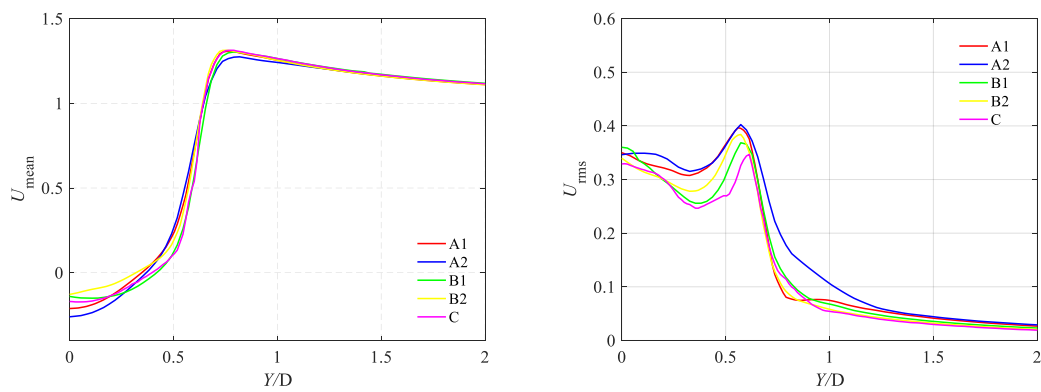


Figure 4.16 Mean stream-wise and r.m.s. velocity at  $x/D=1$

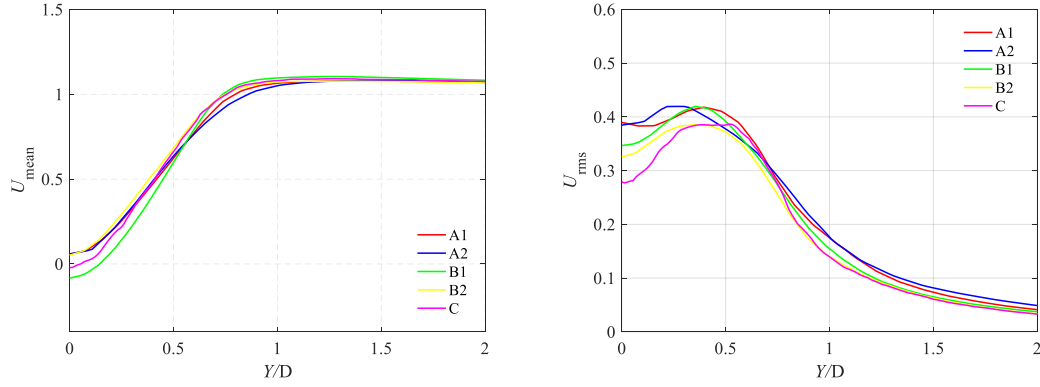


Figure 4.17 Mean stream-wise and r.m.s. velocity at  $x/D=2$

The mean stream-wise velocity and r.m.s fluctuating velocity are shown in Figure 4.14-4.17. We can observe that case B2, although having a coarser mesh refinement and smaller aspect ratio, produces fare agreement with the existing literatures in terms of the mean stream-wise velocity distributions. The results from the finer meshed and larger aspect ratio cases deviate only slightly from that of B2. On the other hand, less satisfying result is obtained for the r.m.s. fluctuating velocity distributions. Lysenko et al. [41] employed high spatial resolution ( $300 \times 300$  in the cross-section plane) and an aspect ratio of  $3.14D$  for LES of flow past a circular cylinder at 3900 Reynolds number, the results of *r.m.s* velocity was under-predicted. Thusly, we can say that predicting fluctuating velocity is much more challenging compares to mean values.

Table 4.4 Recirculation length of five cases

No.	A1	A2	B1	B2	C
$L_r/D$	1.42	1.41	1.64	1.45	1.52

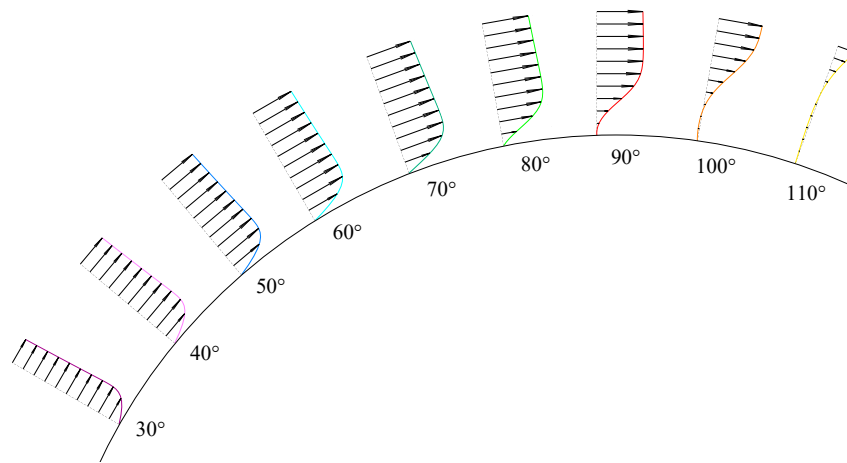
The difference between measurements and numerical calculations for the mean recirculation zone length  $L_r$  is significant and often subject to discussion. By definition, the recirculation length  $L_r$  corresponds to the distance between the base of the cylinder and the sign change of the centerline mean stream-wise velocity. The quality of  $L_r$  predictions may be considered as the deciding factor about the agreement between the experimental and numerical results.

Experimental data provided by Dong et al. [48] and Parnaudeau et al. [40], revealed a recirculation zone length  $L_r/D = 1.36-1.51$ . In the context of the numerical simulations that were performed supporting the above experiments (Dong et al. [48] and Ma et al. [49]), the length of the recirculation bubble was reported in the range 1.41-1.59. Further, a more extended recirculation bubble of  $L_r/D = 1.67$  and  $L_r/D = 1.64$  were reported by Lysenko et al. [41] and Franke and Frank [50], respectively.

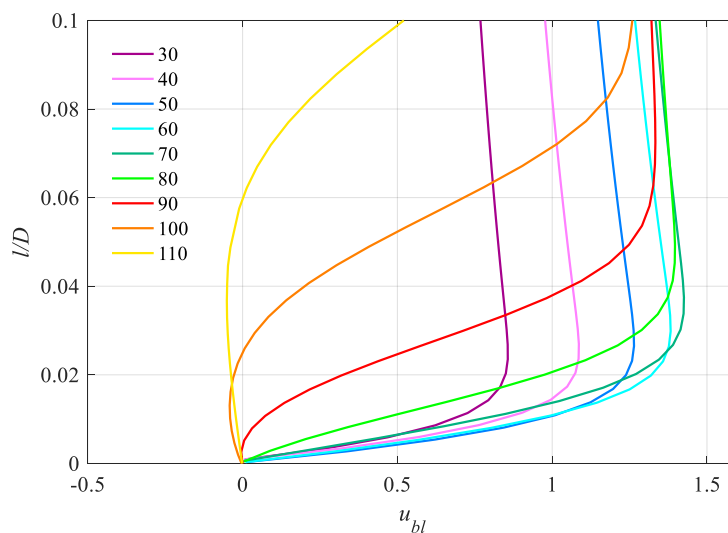
In the present LES on the one hand, the recirculation zone length was predicted as  $L_r/D = 1.41-1.64$ , which was in a fairly good agreement with data of both experimental

and numerical works.

### 4.3.4 Separation point



(a) Boundary layer profiles on the cylinder surface



(b) Boundary layer profiles of various angles

Figure 4.18 Boundary layer profiles of the circular cylinder.

Figure 4.18 presents the boundary layer profiles at different angular locations of the circular cylinder (model B2). By plotting the boundary layer profiles, the separation point could be identified. In Figure 4.18 (b),  $u_{bl}$  is the mean velocity tangential to the cylinder wall and  $l$  is the distance from the surface. From Figure 4.18 (a), it is obvious that the boundary layer gradually accelerates before  $\theta = 70^\circ$ . Between  $\theta = 70^\circ$  and  $90^\circ$ , the velocity is retarded near the surfaces and the boundary layer thusly thickens swiftly. The boundary layer profile shifts from an L shape to an S shape, which is an evidence of the existence of the inflection point. It is thus decided that the boundary layer separation point lies between this range. At  $\theta = 90^\circ$ , the reverse flow has already taken place, again indicating the separation has already occurred. The reverse flow is more clearly shown at  $100^\circ$  and  $110^\circ$ .



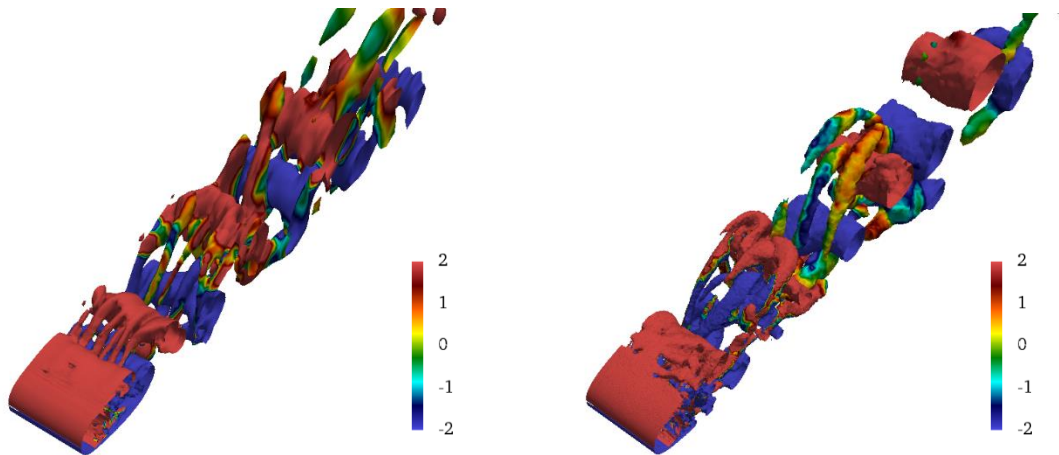
The above boundary layer profiling method is applied to find the separation points in this study. By observing the reverse flow of boundary layer, the separation point for the circular cylinder is  $\theta_{sep} = 88^\circ$ . As known from measurements [51] [45], the separation should take place at around  $\theta_{sep} = 86^\circ$ . On the other hand, the calculated values of  $\theta_{sep}$  from the most cited LES runs are in the range of  $\theta_{sep} = 87^\circ \sim 88^\circ$  [41] [43] [50]. The predicted  $\theta_{sep} = 88^\circ$  was slightly higher than the experimental results and were consistent with previous LES data.

### 4.3.5 Vortex flow structures

Figure 4.19 visualizes vortex flow structures around the cylinder in the cases with different aspect ratio and grid resolutions using an iso-surface of the second invariant  $Q$  of velocity gradient tensor  $u_{i,j}$  (Hunt et al. [52]):

$$\begin{aligned} Q &= \frac{1}{2}(\Omega_{ij}\Omega_{ij} - S_{ij}S_{ij}) \\ &= -\frac{1}{2}(u_{i,j}u_{j,i}) \end{aligned} \quad (4.2)$$

where  $\Omega_{ij} = 1/2(u_{i,j} - u_{j,i})$  and  $S_{ij} = 1/2(u_{i,j} + u_{j,i})$  are the rotation rate and the strain rate, respectively. The invariant  $Q$  describes the balance between pure strain and fluid rotation. The surface of positive  $Q$  represents the region where the rotation overcomes strain in strength. It identifies coherent vortex structures effectively. The  $Q$  value of an iso-surface in Figure 4.9 is 1.5 and the iso-surfaces are contoured by the vorticity in the local spanwise direction from -2 to 2 in order to roughly distinguish the vortices that shed from the one side from another.



(a) case B2

(b) case C

Figure 4.19 Iso-surfaces of  $Q = 1.5$  for the flow around the cylinder

In Figure 4.19, both cases show well-resolved Karman vortex-shedding and streamwise vortex flow structures as depicted. Although there is no big difference between the two cases, the cross-stream vortex flow structures in the case C in Figure

4.19 (b), however, dissipate at a higher rate downstream behind the cylinder while moving in the streamwise direction.

Based on the above discussions, it can be concluded that the discrepancy of case B2 and other refined cases is small. Particularly, case B2 qualifies an accurate prediction of flow variables such as mean velocity, aerodynamic forces, etc. Therefore, case B2 was adopted in the following study.

## 4.4 Summary

Flow characteristics for flow past a smooth cylinder were investigated by means of large eddy simulations (LES).

Spanwise extension of  $2D$  and  $3.14D$  were employed in this chapter. The flow around a  $2D$  cylinder do not show a big difference when compared to the  $3.14D$  case in terms of flow characteristics, such as pressures on the cylinder surface, drag and lift coefficients and flow velocity distributions.

Cases with different grid shapes (structured hexahedral meshes and unstructured polyhedral mesh) were also conducted to make a comparison. The results of unstructured polyhedral mesh case have only a small discrepancy with the other structured cases, though the cross-stream vortex flow structures dissipate at a slightly higher rate downstream behind the cylinder, which may not have a remarkable influence on the flow characteristics near the cylinder.

The results of numerical simulations are proved to be reliable. Thusly the methods for three-dimensional flow and associated forces on the circular cylinder normal to the flow is adopted in the following parts.

# Chapter 5 Simulation of Flow Past Cylinders with uniform indented surface

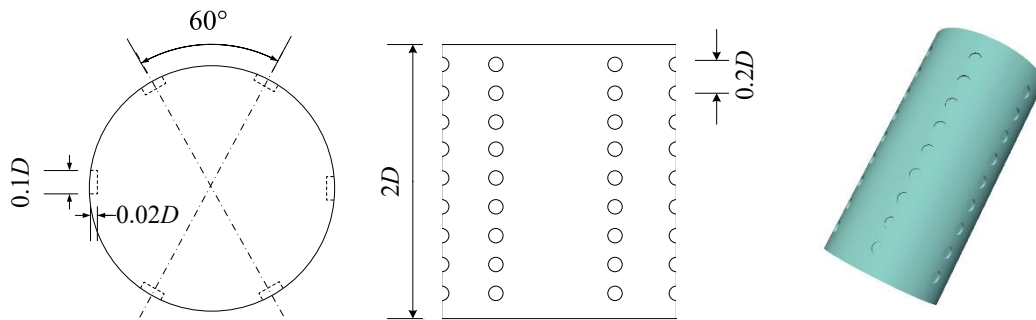
In this chapter, circular cylinders with two uniform-indented densities, i.e., 6 and 8 rows of indentations along the circumference are used in the LES simulations of the flow around the cylinders at Reynold number 3900.

Based on the reliable results of the smooth cylinder presented in the former chapter, those numerical conditions are therefore used. The simulation employ a spanwise length of  $L_z = 2D$ , a radial extension of  $20D$  and spanwise periodic boundary conditions. The effect of cylinders with uniform indented surface on the flow characteristics are investigated.

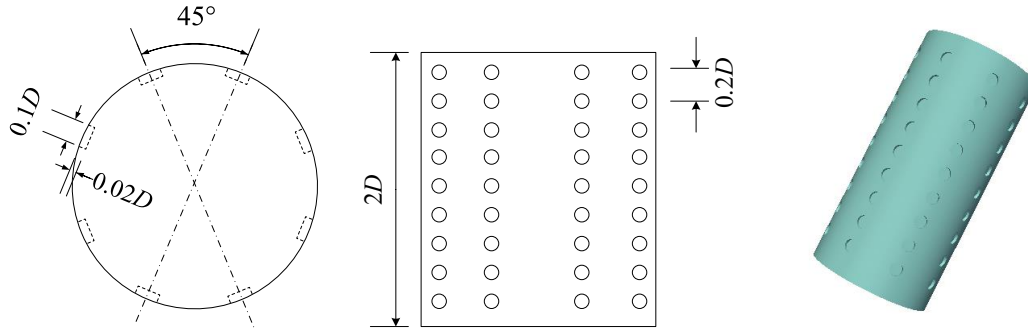
## 5.1 Case setup

### Geometry

The design picture of the uniform-indented cylinders is shown in Figure 5.1. All of the models are fully covered with indentation. The indentations are laid out with two indented densities, i.e., 6 and 8 rows of indentations along the circumference. The diameter ( $d$ ) and depth ( $k$ ) of the indents were 11 mm ( $d/D = 0.1D$ ) and 2.2 mm ( $k/D = 0.02$ ), respectively. The center-to-center spanwise distance between indentations was 22 mm ( $0.2D$ ). Figure 5.1 shows detailed dimensions of the uniform-indented cylinders.



(a) Cylinder with 6 columns of indentations along the circumference



(b) Cylinder with 8 columns of indentations along the circumference

Figure 5.1 Schematics of the cross-sectional and side views of the indented cylinders

## Meshing

Table 5.1 The covered simulated cases

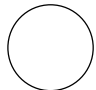


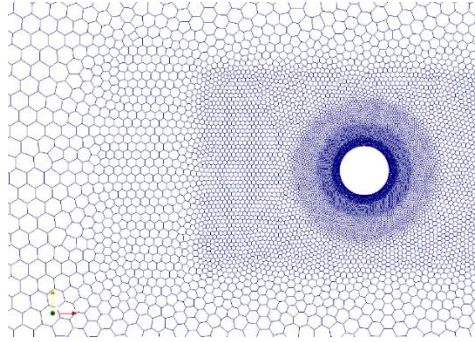
sketch	Test description	Cells ( $\times 10^6$ )	Remark	CPU time (days)
→ 	Smooth	1.15	ORI	5
→ 	6 rows of indentation	2.11	IND6	20
→ 	8 rows of indentation	2.12	IND8	20

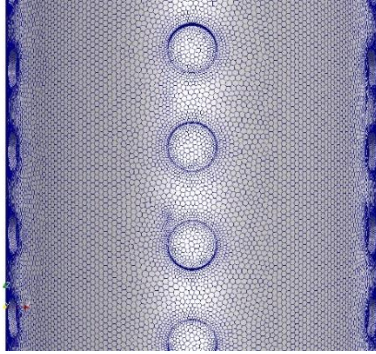
Table 5.1 presents the cases that are used in this chapter for the uniform-indented circular cylinders at  $Re = 3900$ . Among them, case 1 is the original smooth circular cylinder which has been discussed in the previous chapter. Case 2 and case 3 are uniform-indented circular cylinders with various indented densities.

For all the cases, the first grid spacing normal to the wall of the cylinder was positioned at less than (or equal to)  $y_+ \Delta$  of 1. In this study, the first grid spacing is set to be  $0.0025D$  away from the cylinder wall.

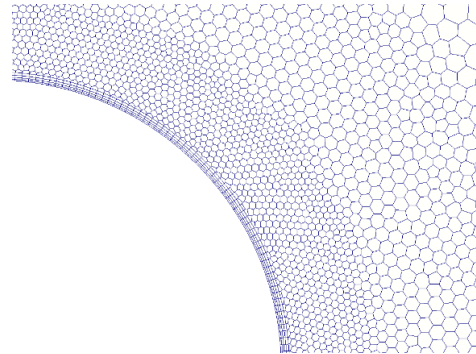
Unstructured polyhedral mesh has been adopted for all the uniform-indented cases, Figure 5.2 shows the grid of the indentations and around the uniform-indented circular cylinders.



(a) grids of computational domain



(b) grids of indentation



(c) grids around the cylinder

Figure 5.2 Meshing

## Numerical methods

The same boundary conditions and numerical methods were employed in the current cases, i.e., uniform-indented cylinders, including the condition  $\max Co < 2$  to determine the time-step, a pre-run of 100 non-dimensional seconds and 200 non-dimensional seconds for about 40 vortex shedding cycles.

The boundaries are the same as shown in Figure 4.1. At the inlet boundary, the constant velocity  $u=1$  m/s along the x-axis. Periodicity is also employed in front and back faces.

## 5.2 Aerodynamic forces

Table 5.2 Aerodynamic forces of three models

No.	$C_d$	$C_{l, rms}$	$St$
ORI	0.999	0.136	0.213
IND6	0.987	0.147	0.212
IND8	0.969	0.119	0.210

Table 5.2 shows the aerodynamic forces of three models and their Strouhal Numbers. The average drag force coefficient for IND6 and IND8 decrease a bit when compare to ORI. The reduction is 1.2% and 3.0%, respectively. For the fluctuating lift force

coefficient, the value of IND8 decreases 14% when compare to ORI. The Strouhal Number ( $St$ ) of all the three cases are almost the same, which is near the constant value 0.210.

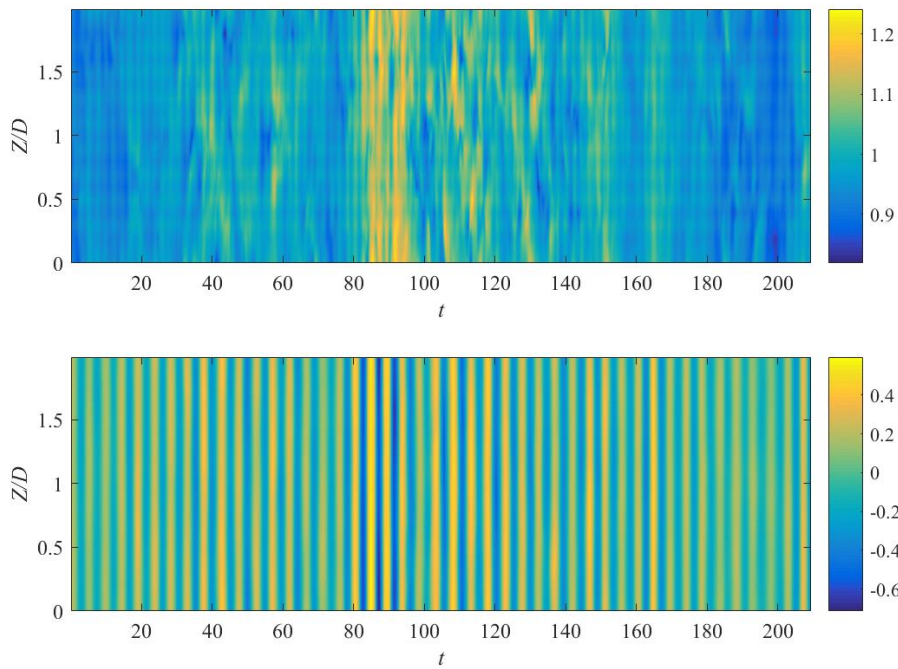


Figure 5.3 Spatial-temporal distribution of force coefficients (Case IND6)  
(upper figure,  $C_a$  ; lower figure,  $C_l$ )

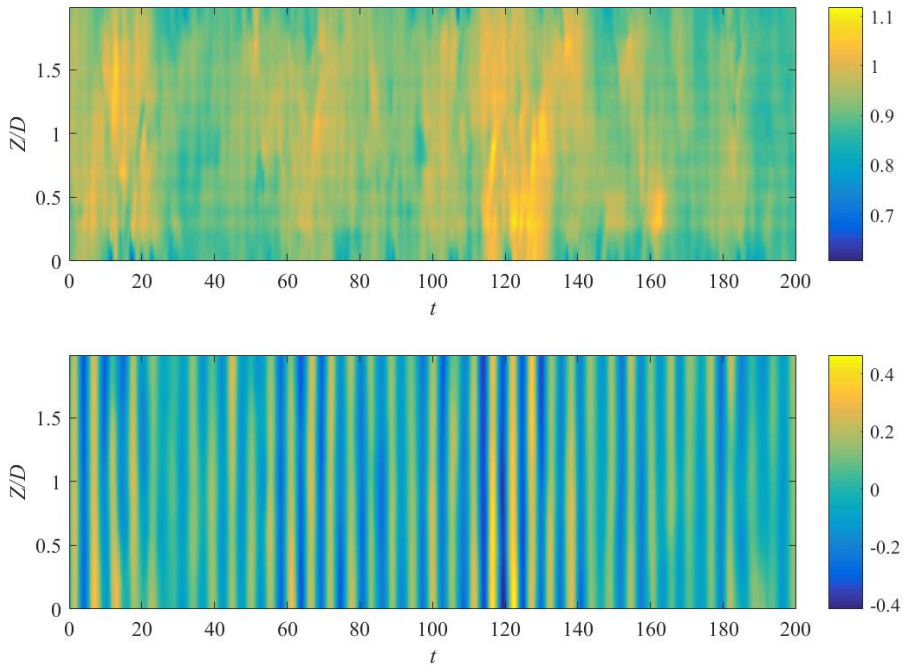


Figure 5.4 Spatial-temporal distribution of force coefficients (Case IND8)  
(upper figure,  $C_a$  ; lower figure,  $C_l$ )

Owing to the three-dimensional nature of the indented geometry, it is also interesting to examine the span-wise distributions of the force coefficients. Figure 5.3 and Figure

5.4 present the spatial temporal distribution of drag and lift force coefficients for IND6 and IND8, respectively.

The drag force coefficient contours of both indented cylinders are quite different from the smooth one (shown in Figure 4.10). The value is slightly reduced in the place where the indentations locate compared with the plain surface without indentation. This kind of phenomenon is continuous in the time histories. Therefore, a parallel stripe pattern is observed for indented geometries. It seems that these indentations divided the cylinder into small blocks.

The same phenomenon does not be detected in the contour of lift force coefficient contours. It reveals that indentations on circular cylinders may only have influence on drag force coefficients.

In the following sections, statistics on the cylinder surfaces, along the cylinder's circumference and around the cylinders will be discussed to reveal the effects of indentations on the flow past a circular cylinder.

## 5.3 Statistics on the cylinder surface

### 5.3.1 Pressure distributions for the whole cylinder

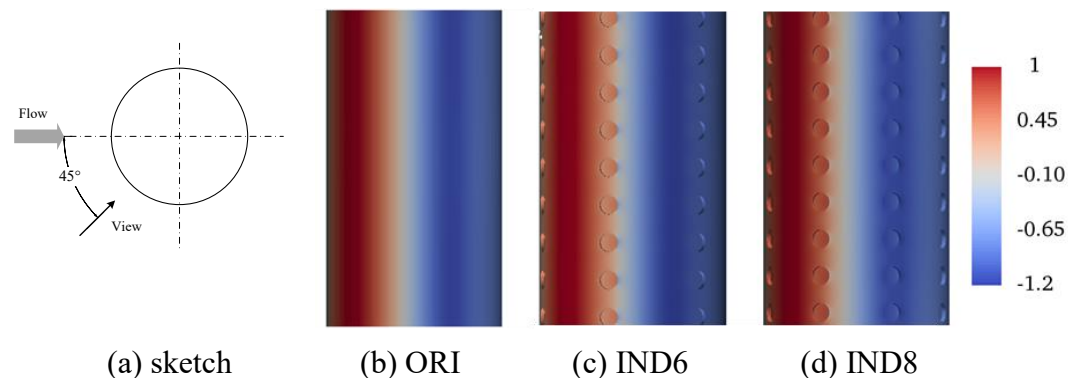


Figure 5.5 Mean pressure coefficient on cylinder surface (from a view of  $45^\circ$ )

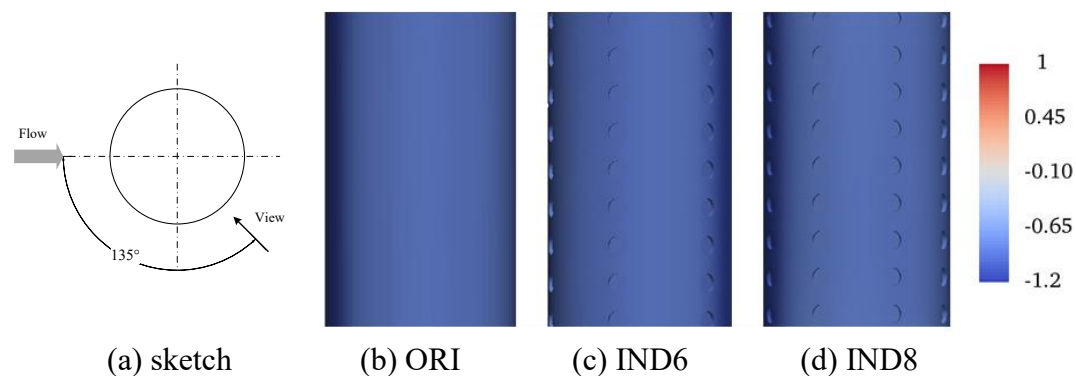


Figure 5.6 Mean pressure coefficient on cylinder surface (from a view of  $135^\circ$ )

Figure 5.5 and 5.6 show the mean pressure coefficient contours on cylinder surfaces for three cases from a view of  $45^\circ$  and  $135^\circ$ , respectively. All the geometries show the similar distribution pattern: the positive pressures turn into negative ones at an angle of

around  $35^\circ$ . Then the negative pressures decrease to the minimum value and slightly increase and reach to a stable negative value behind the separation point. The maximum and minimum value of smooth cylinder and indented cylinders are almost the same, ranging from -1.2 to 1.0.

On the leeward side of the cylinders (from the view of  $135^\circ$  (Figure 5.6)), the pressure distribution of three geometries do not have much difference in terms of both value and pattern.

On the other hand, some differences can be detected in Figure 5.5 ( $45^\circ$ ). The pressure contour on the surface of smooth cylinder seems to have a parallel distribution along the z axis. While the pressure contours of indented cylinders seem to have some abrupt changes. Those changes may have strong relationships with the location of indentations.

Therefore, in order to reveal the differences between the pressure distribution of those indentations, mean pressure coefficient contours and curves of indentations located between  $0^\circ$  to  $90^\circ$  are presented in Figure 5.7 to 5.10.

### 5.3.2 Pressure distributions near the indentations

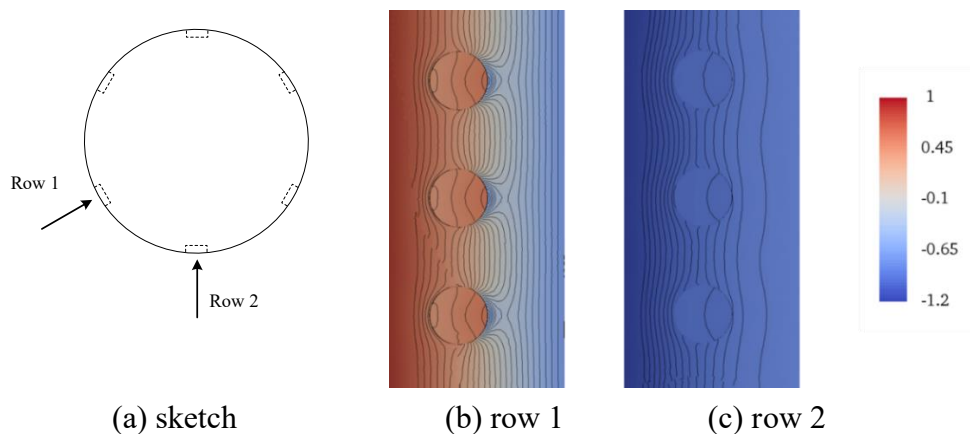
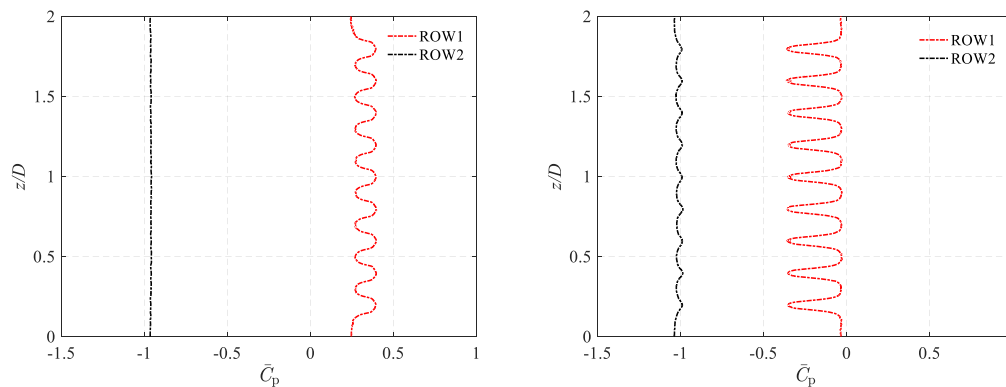


Figure 5.7 Distribution of mean pressure coefficient near the indentation for IND6



(a) along the center line of indentations (b) along the trailing-edge line of indentations

Figure 5.8 Distribution of mean pressure coefficient for IND6



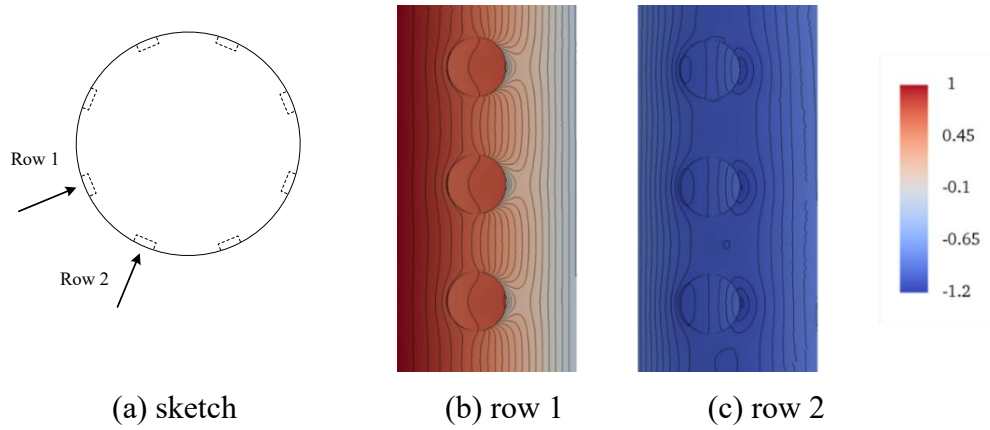
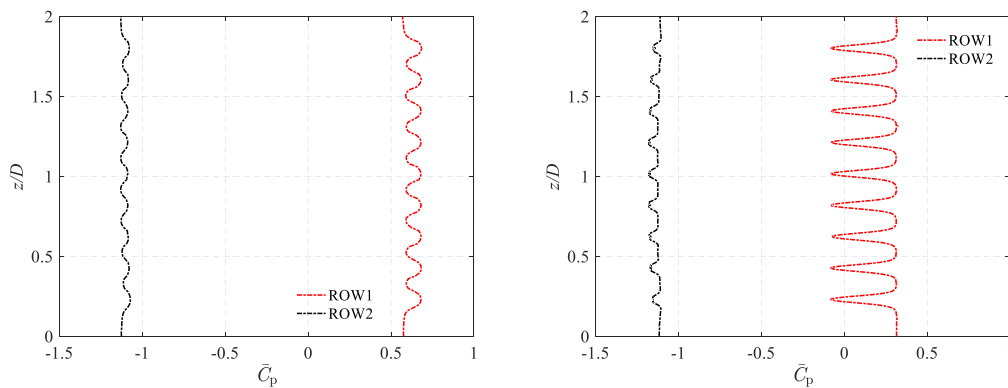


Figure 5.9 Distribution of mean pressure coefficient near the indentation for IND8



(a) along the center line of indentations (b) along the trailing-edge line of indentations

Figure 5.10 Distribution of mean pressure coefficient for IND8

A sketch of the location of indentation row 1 and row 2 for IND6 is presented in Figure 5.7 (a). From Figure 5.7 (b), (c), it is obvious that zigzag contour lines are observed near and inside the indentation other than parallel lines. Those contour lines seem to be guided by the indentations.

Row 1 is located at an angle of  $30^\circ$ , negative pressures are detected on the indentation sides. Inside the indentation, the pressures increase slightly. This may be resulted from the sinking inflow and its impact. Row 2 is located at an angle of  $90^\circ$  which is near the separation point. Although wavy contour lines are also observed, the pressure values inside the indentation do not have a large deviation from the smooth one. In contrast, the pressure curve along the trailing-edge line of indentation row 2 (Figure 5.8 (b)) shows greater negative pressures near indentation side.

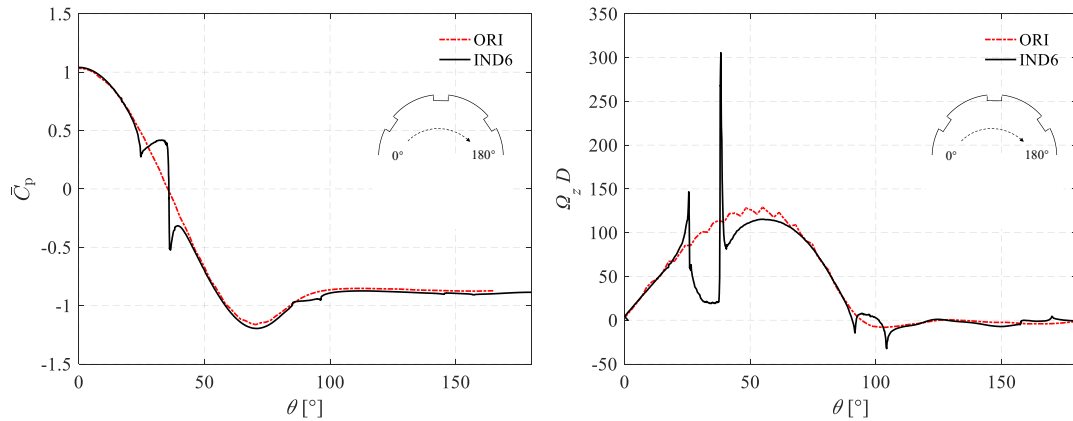
For IND8, wavy contour lines are also detected on both indentation rows (Figure 5.9). Row 1 is located at an angle of  $22.5^\circ$ , the changes of pressure are almost the same with IND6. A greater reduction is detected on indentation rear edge, turning the positive pressures into negative ones.

Row 2 is located at an angle of  $67.5^\circ$  where the minimum negative pressure occurs. The gradient of pressure curves is larger than that of IND6 row 2. Moreover, contrary

to IND6, smaller negative pressures are observed near the indentation rear edge. Therefore, the indentation located behind the place where the minimum negative pressure occurs seem to have a certain effect on the pressure changes.

## 5.4 Statistics along the circumference of cylinder

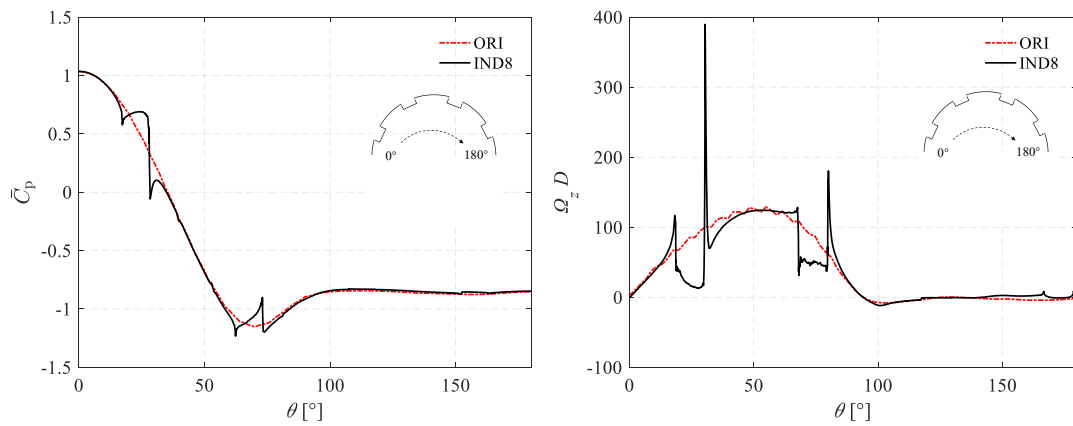
### 5.4.1 Pressures and span-wise vorticity



(a) Pressure coefficients

(b) Span-wise vorticity

Figure 5.11 Comparison results of cylinder circumference for ORI and IND6



(a) Pressure coefficients

(b) Span-wise vorticity

Figure 5.12 Comparison results of cylinder circumference for ORI and IND8

Figure 5.11 (a) and 5.12 (a) show the pressure coefficients as a function of the azimuthal angle  $\theta$ . The span-wise vorticity results are shown in Figure 5.11 (b) and 5.12 (b). Note that  $\theta=0^\circ$  corresponds to the leading edge of the cylinder while  $\theta=180^\circ$  corresponds to the trailing edge.

The pressure coefficient curve of ORI shows a smooth variation, while the profiles of the indented cylinders show sharp spatial variations consistent with their physical geometries. For those indentation located before the separation point, the pressure

coefficients are lowest at the edge of indentations and largest at the pit. After  $\theta = 90^\circ$ , as the boundary layer has completely separated, the pressure coefficients remain almost unchanged, with their values being close to that of the unmodified cylinder.

Also, the span-wise vorticity on the indented cylinder surface differs considerably from the smooth one. Contrary to the pressure coefficients, the span-wise vorticity is smallest at the pit and largest at both side of the indentation.

This behaviour of pressure coefficients and span-wise vorticity is resulted from the acceleration of flow at the edge of indentations and deceleration inside the indentation. Although the maximum vorticity is much larger than the smooth cylinder, the overall integrated effect of span-wise vorticity for indented-cylinders is smaller than the smooth one, which may contribute to a smaller viscous drag force. While the variation of drag coefficient between IND6 and IND8 may due to the second row of indentations. The reduction of span-wise vorticity at row 2 is absent for IND6.

## 5.4.2 Boundary layer profiles of velocity

### Inside the indentation

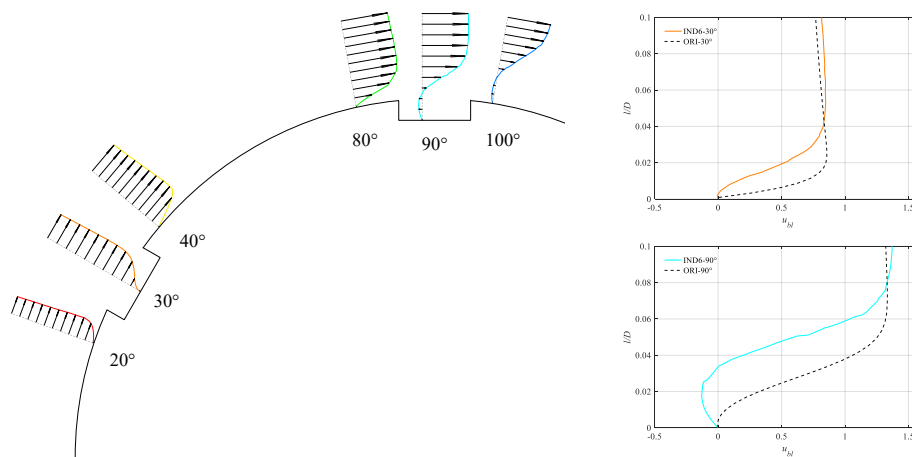


Figure 5.13 Boundary layer profiles near the indentation of IND6

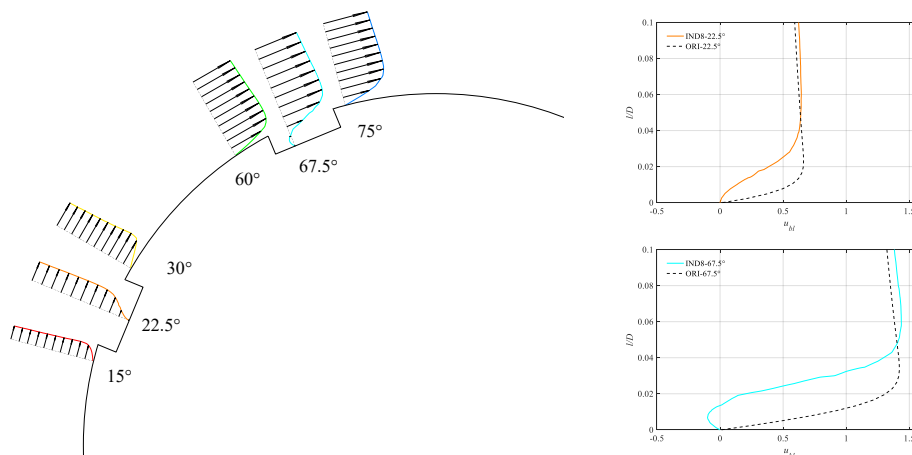


Figure 5.14 Boundary layer profiles near the indentation of IND8

By plotting the boundary layer profiles, the velocity near the cylinder surface and

indentation could be identified. Depicted in Figure 5.13 and 5.14 is the boundary layer profiles at different angular locations of indented cylinders. For each boundary layer profiles at the location of indentation, the one of smooth cylinder is also plotted (the dash line).

The boundary layer profiles at those pits show great difference with the smooth one. For row 1, the velocity outside the indentation is observed to accelerate while the velocity reduces to zero swiftly inside the indentations. It means that the indentation is filled with the quiescent flow. For row 2, the boundary layer profile for both geometries shifts from an L shape to an S shape, indicating the occurrence of the reverse flow inside the indentations. While the boundary layer profiles at indentation sides show the same pattern with the smooth one.

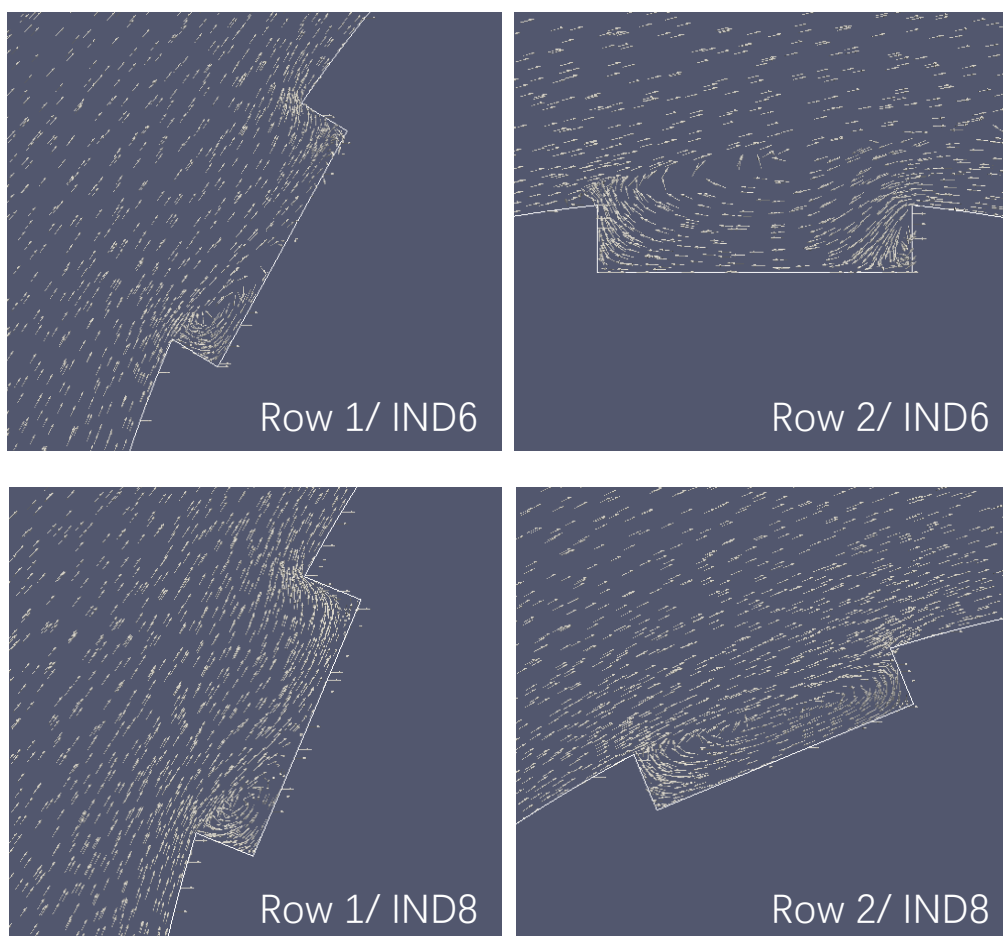


Figure 5.15 Vector plot showing flow within the indentations

It appears that the flow pattern near the surface changes significantly due to the presence of indentations. Figure 5.15 presents velocity vectors near those indentations for IND6 and IND8, respectively. Since the indentations located in the backward of the cylinder do not have much effects according to the pressure distribution, here only indentation Row 1 and Row 2 are plotted.

For Row 1, the velocity seems to sink down into the indentation with a much smaller

velocity value. A small bubble near the front side is detected and this is due to the separation near the leading edge of the indentation.

On the other hand, an obvious recirculation zone within the indentation can be observed for row 2. The ‘S’ shape boundary layer is also resulted from the reverse flow in this recirculation zone.

This kind of phenomenon is quite similar with the one of cactus-shaped cylinders. The indentations create recirculation zones filled with low momentum quiescent flow. These quiescent recirculation zones within the indentations lead to lower velocity gradient which decreases the contribution of viscous forces [29]. This mechanism is absent in a smooth cylinder.

### At the edge of indentation

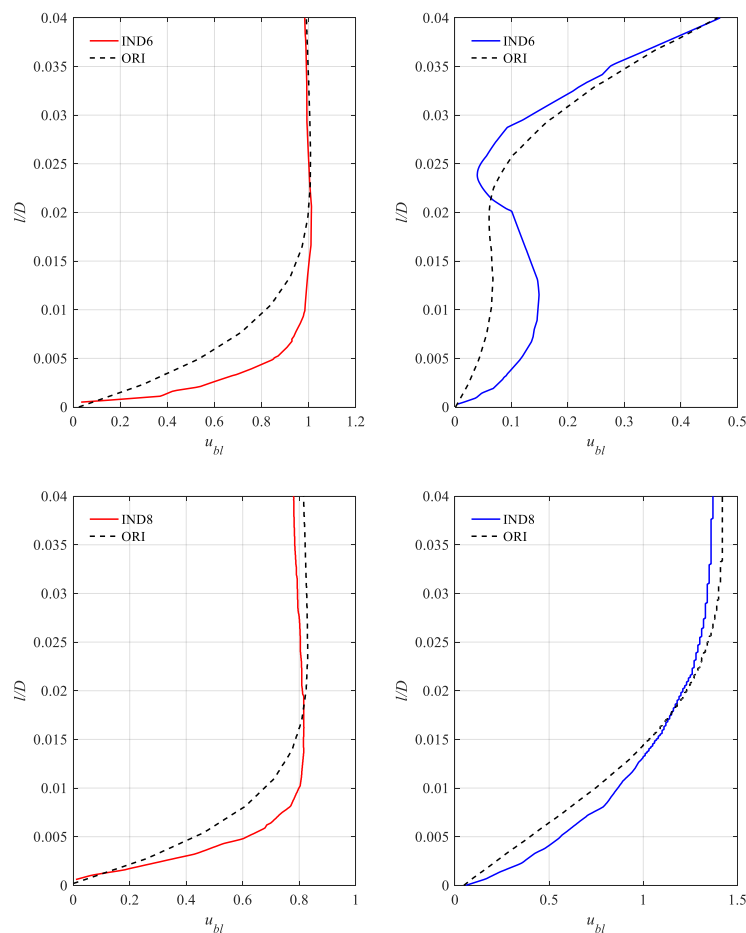


Figure 5.16 Boundary layer profile of velocity at the trailing edge of indentation (left: row 1, right: row 2)

The boundary layer profiles of velocity at the trailing edge of row1 and row2 of indentations for two indented cases are presented in Figure 5.16, where the results at the corresponding angle of the smooth cylinder are also shown for comparison. The figure shows that for both two cases, the velocities near the bottoms of the boundary layers at the trailing edge of indentation are larger than that of smooth cylinder for both

two rows.

The vorticity contours at the indentations are shown in Figure 5.17. As explained in the former section, the vorticity just downstream of the indentations are also much larger than that of smooth cylinder.

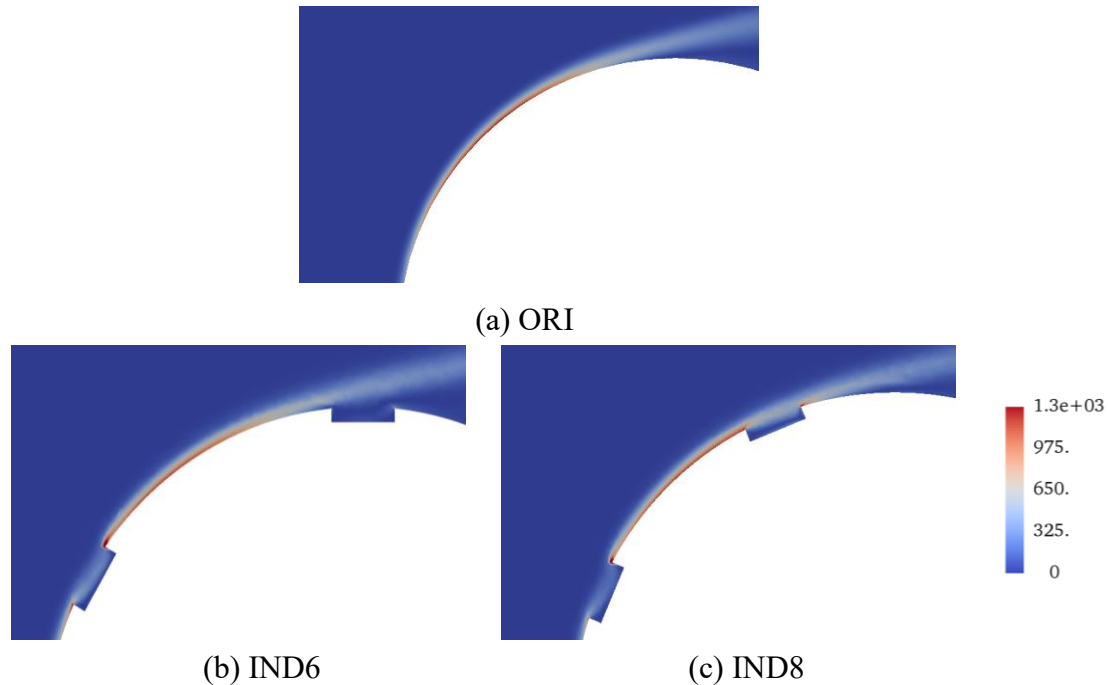


Figure 5.17 Vorticity distributions at the indentations

Similar features have also been identified by Kimura and Tsutahara [26] . In their work, a two-dimensional single groove on the surface of a circular cylinder at Reynolds number of a few thousand are studied. Their results show that the flow near the wall is more energetic just downstream of a groove or shallow cavity and therefore the boundary layer can travel slightly farther against an adverse pressure gradient before separating. One of the main differences between our and the cited one is that our model is three dimensional while the cited one is a two-dimensional one. As they mentioned in the paper, a closed circulation cavity flow can exist stably in the two-dimensional flow while it is hard to reach in three-dimensional dimples.

As depicted in Figure 5.15, though a closed circulating flow is also observed inside the indentations which shows similar features to the dimpled one. However, Figure 5.15 was depicted by a 2-D slice in the center line of indentations. In the actual cases of three-dimensional indentations, the vorticity will form in the shape of horseshoe vortices. Figure 5.18 presents the horseshoe vortices at the second row of indentations, where the closed circulating zone was detected with the aid of Figure 5.15. Clearly horseshoe vortex in each indent is identified for the indented case. It's argued that these horseshoe vortices are the main cause for the transition of the laminar boundary layer to a turbulent one [26] .

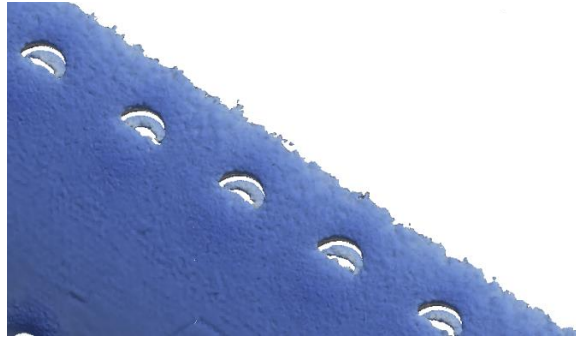


Figure 5.18 Three-dimensional horseshoe vortices for IND8

Then the mechanism for the earlier drag crisis of indented or dimpled cylinders can be explained as follow: for the indent locates at the frontal part of cylinders, vortices are trailed back from each indent or dimple [27] . These vortices can help to energize the cylinder's boundary layer. The disturbance introduced by the indentation promotes the transition of laminar boundary layer to a turbulent one at higher Reynolds number more easily than smooth cylinder, thus delaying the separation causes an earlier drag crisis.

## 5.5 Region division

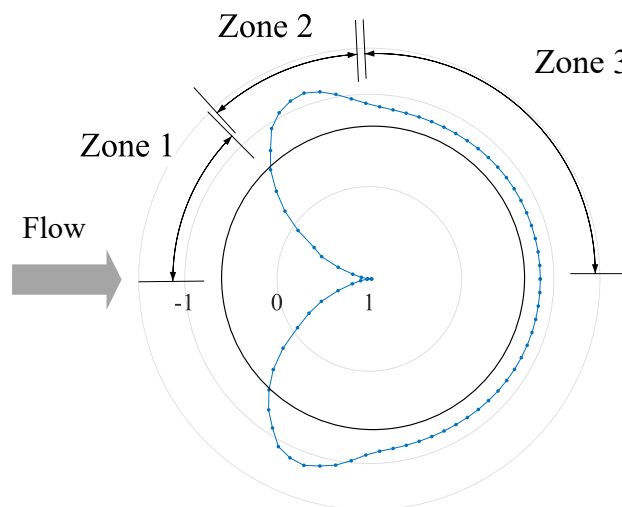


Figure 5.19 Region division of indentation locations

As discussions shown in the above sections, the location of indentation has various effects on the pressure distributions and boundary layer profiles, etc. According to different behaviors and results of indentations, three regions can be divided along the circumference of a semi-circle. The sketch of divided regions thus is presented in Figure.5.19.

Zone 1 is the region with positive pressures. In this region, pressures near the trailing edge of indentations shift from positive to negative. Inside the indentation, the pressure increases slightly and the pit is filled with quiescent flow.

Zone 2 is the region starts from the location where negative pressure starts to appear to separation point. Larger negative pressures are observed at indentation sides. The ‘S’ shape boundary layer profile is detected, indicating the occurrence of reverse flow inside the indentations. For both Zone 1 and Zone 2, the span-wise vorticity reduces greatly due to the indentation.

Zone 3 represents the wake region behind the separation point. The indentations located in this region do not have effects on pressures or velocity.

## 5.6 Statistics of fields around the cylinder

### 5.6.1 Velocity results

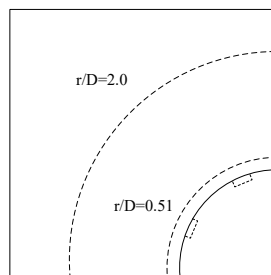
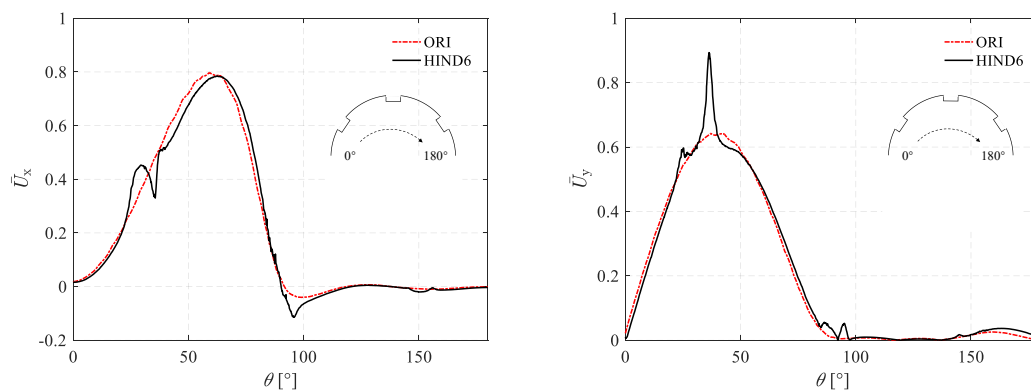


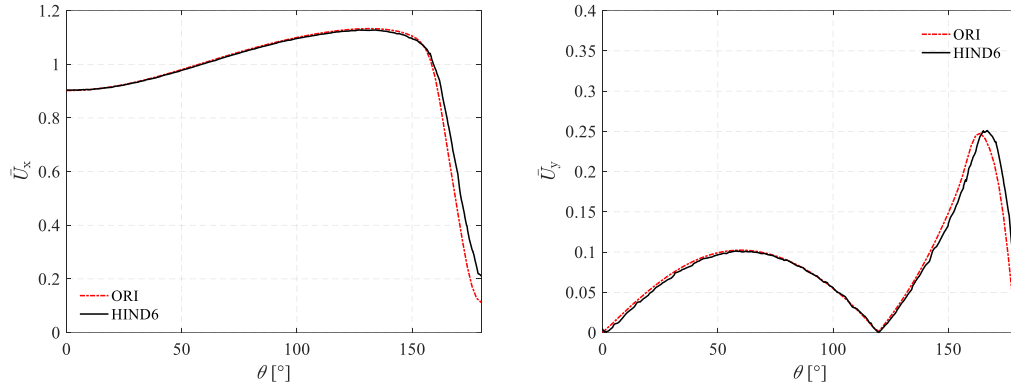
Figure 5.20 Schematic of cylinder surface showing the two azimuthal profiles

The time-averaged statistics of velocity is observed in the fluid domain near the cylinder’s surface for all the geometries and presented in Figure 5.21. These profiles are shown as a function of  $r/D$  (the radial distance from the center of cylinders). There are two  $r/D$  values were adopted, 0.51 and 2, respectively. As presents in Figure.5.20,  $r/D$  of 0.51 is closer to surface of the cylinders while 2.0 is closer to the free-stream. In this way, the effect of the indentations on the near-field and free-stream can be studied.

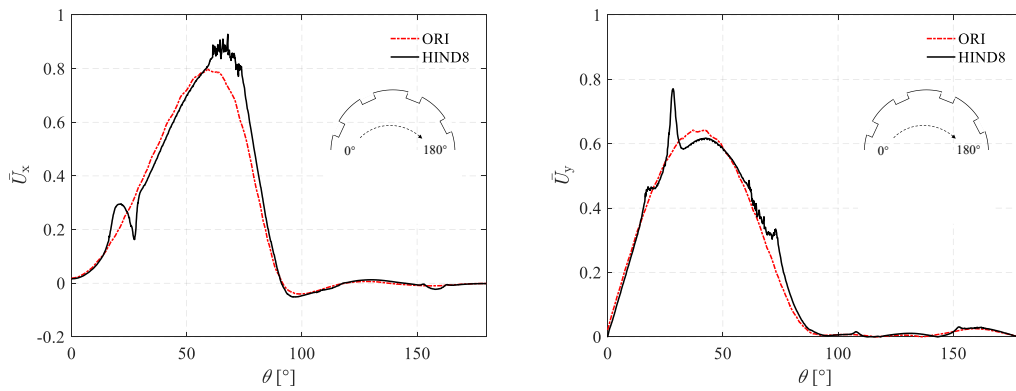


(a) Velocity statistics for IND6 at  $r/D=0.51$

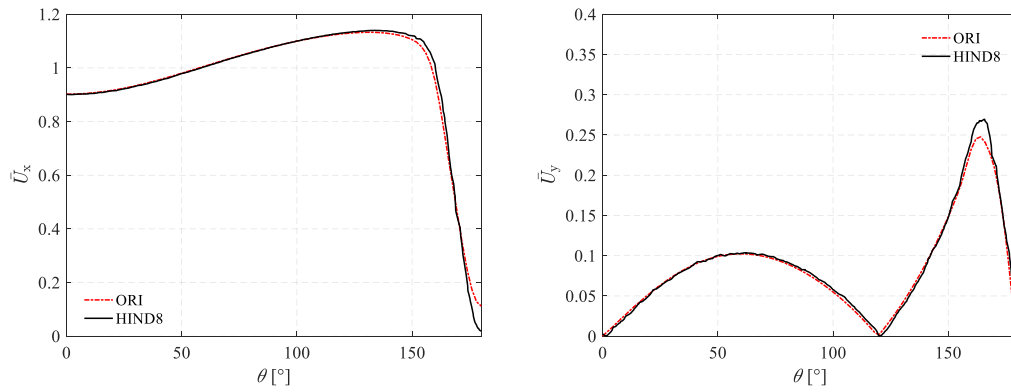




(b) Velocity statistics for IND6 at  $r/D=2$



(c) Velocity statistics for IND8 at  $r/D=0.51$



(d) Velocity statistics for IND8 at  $r/D=2$

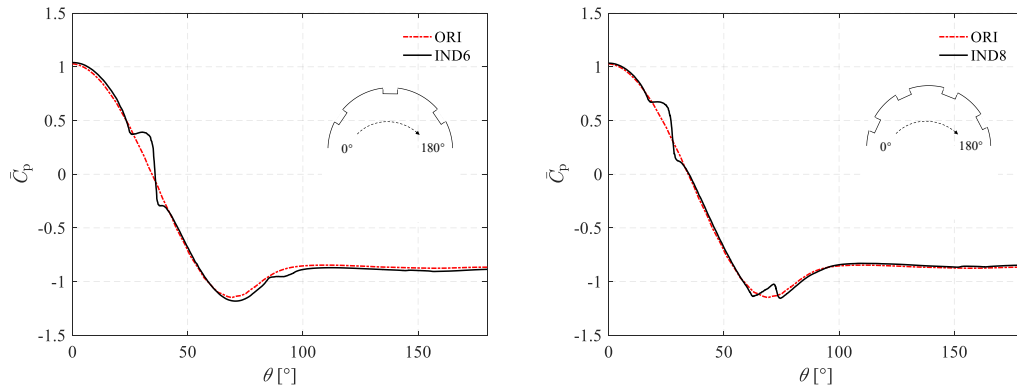
Figure 5.21 Comparison of velocity statistics of three models

Figure 5.21 (a) and (c) show that mean valued of velocities in both x and y directions for a smooth cylinder and indented cylinders are similar in both patterns and values. However, some obvious differences can be observed near the indentations at  $\theta < 90^\circ$  (before the separation point). For both models, the mean velocity in y direction near the indentation side increases sharply, while in the middle of indentation the value seems to be the same as the smooth cylinder. As for the x-direction velocity, the value decreases in to a 'v' shape at the indentation for first column of both models and second column of IND6. While the velocity for second column of IND8 is a bit higher than the

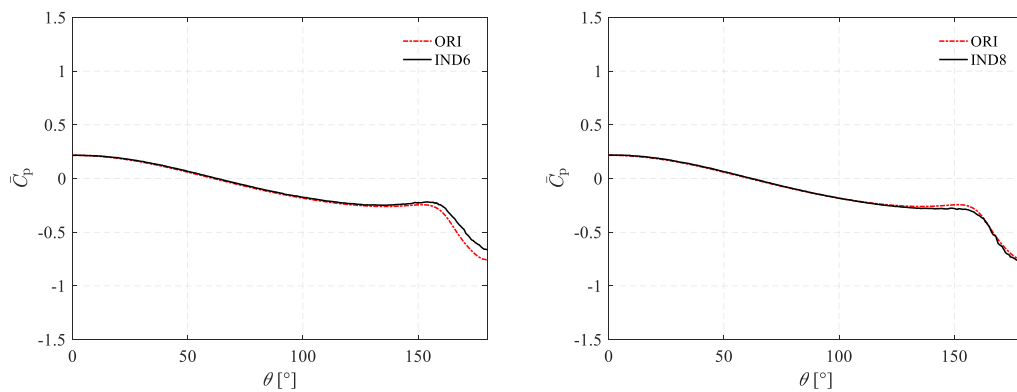
smooth cylinder and makes the curve much rougher.

Farther away from the surface ( $r/D=2$ ), the mean velocity for both models appear to collapse into a single profile except for some slight differences at the wake region.

### 5.6.2 Pressure results



(a) Pressure statistics at  $r/D=0.51$ .



(b) Pressure statistics at  $r/D=2$

Figure 5.22 Comparison of pressure statistics of three models

Statistics of pressure fields are shown in Figure 5.22.

In Figure 5.22, the azimuthal profiles are seen to be quite different for the mean pressure coefficients closer to the cylinder surface. The mean pressure coefficient of both geometries shows the same trend as the surface ones (Figure 5.11 and 5.12). However, no more pronounced difference is observed for the azimuthal profiles at  $r/D=2.0$ .

Following the above discussion, it can be concluded that the different forces acting on the indented cylinder appear to be a surface phenomenon rather than induced behavior by the wake region.

### 5.6.3 Vortical structures

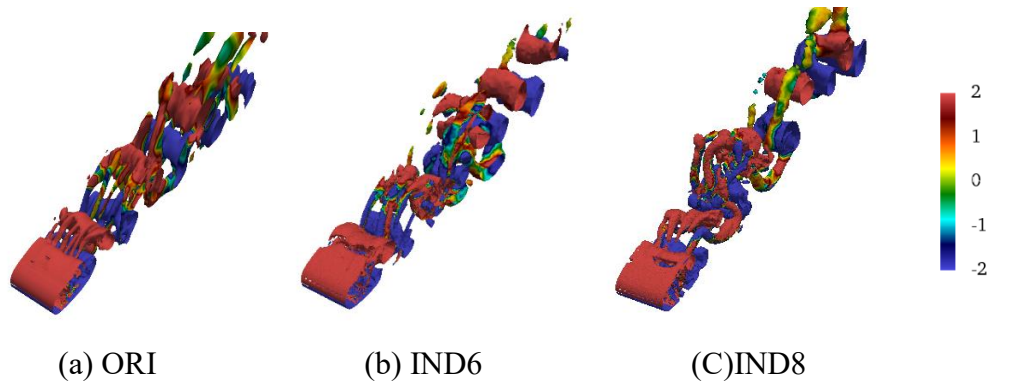


Figure 5.23 3-D vortical structures for three geometries

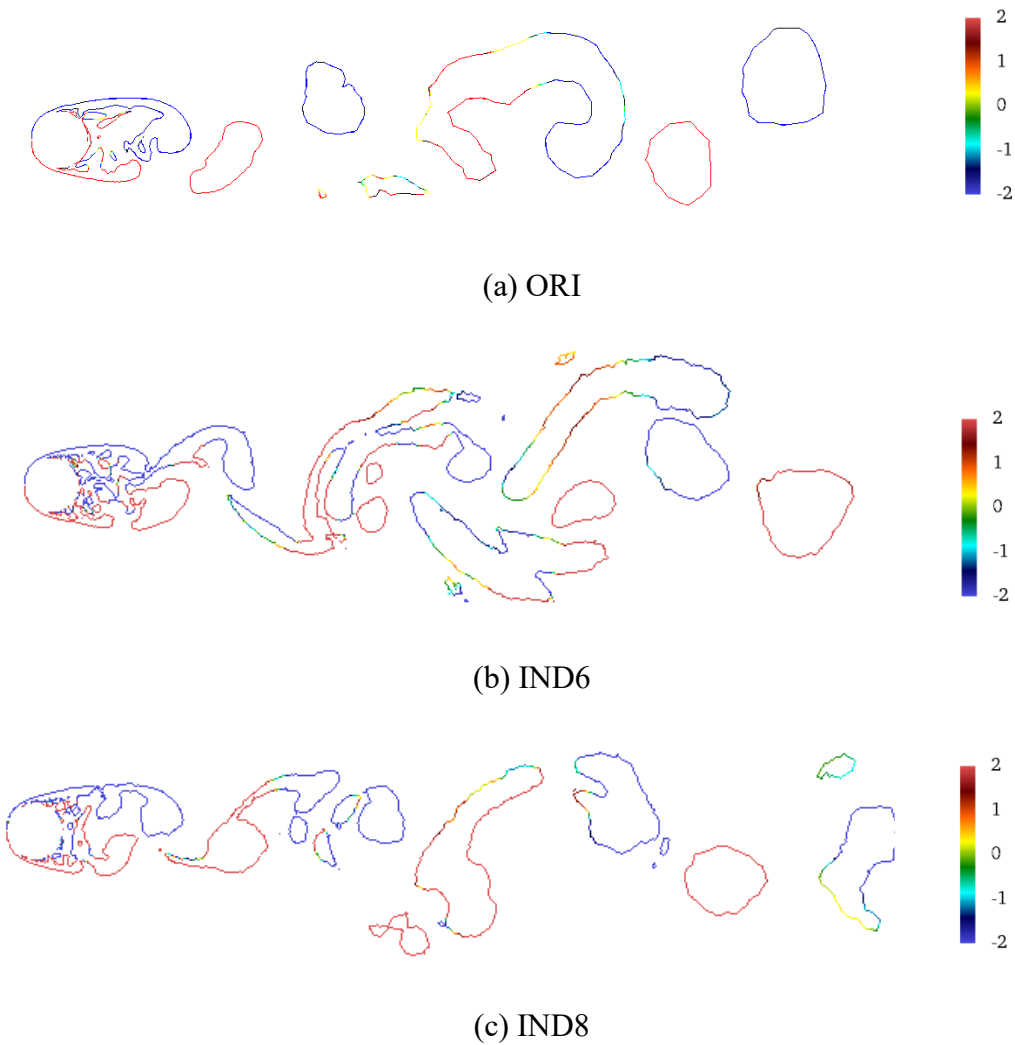


Figure 5.24 Contour lines of stream-wise vorticity

Figure 5.23 shows three-dimensional vortical structures and Figure 5.24 shows the contour lines of stream-wise vorticity in the X-Y plane for all the three geometries. All

the figures were contoured by the vorticity in the local spanwise direction from -2 to 2 as mentioned in Session 4.3.5.

The three-dimensional vortical structures of three geometries show well-resolved Karman vortex-shedding phenomenon and streamwise vortex flow structures as seen in Figure 5.23. The coherent vortex structures move downstream behind the cylinder with moderate dissipation.

Williamson [53] presents a detailed review of the instabilities in cylinder wakes for a wide range of Reynolds. For Reynolds = 1000 to 200000, the developing instability of the separating shear layers from the sides of the body as depicted in Figure 5.24 for all the three geometries. The decrease in formation length in this regime is also observed in Figure 5.24, which is originally demonstrated by the visualization of Unal & Rockwell [54]. It appears that although indentation alter the flow near the cylinder surface, they do not change the nature of flow in the wake region.

## 5.7 Summary

In this chapter, Large Eddy Simulation have been conducted on two uniform-indented circular cylinders at  $Re = 3900$ . Two indented cylinders have 6 rows and 8 rows along the circumference. In addition, the normal cylinder has also been included for the comparison purpose. The simulation results are interpreted from various aspects such as the aerodynamic forces, statistics on the cylinder surfaces, along the cylinder's circumference and around the cylinders are discussed to reveal the effects of indentations on the flow past a circular cylinder. The main conclusions in the current research are summarized as follows.

1. The indentations have a significant effect on drag force rather than lift force. The average drag force coefficient for IND6 and IND8 decrease 1.2% and 3.0% when compare to ORI, respectively. The drag force is slightly reduced in the place where the indentations locate compared with the plain surface without indentation. A parallel-stripe pattern is observed for the indented geometries.

2. Based on the different behaviors of indentations with various locations. three regions can be divided along the circumference of a semi-circle. Indentations located in positive pressure areas is defined as Zone 1. In this region, pressures near the trailing edge of indentations shift from positive to negative. Inside the indentation, the pressure increases slightly and the indentation is filled with quiescent flow. Zone 3 represents the wake region behind the separation point where the indentations do not have effects on changing the flow. Zone 2 is the region between Zone 1 and Zone 3. Larger negative pressures are observed at indentation sides. The 'S' shape boundary layer profile is detected, indicating the occurrence of reverse flow inside the indentations.

3. By examining the boundary layers just downstream of indentations, it is revealed that the velocity and vorticities both increase in Zone 1 and Zone 2. It means that the indentation could energizing the boundary layer and make it easier for the transition from laminar to turbulence happens. Thusly a lower critical Reynolds number for an indented cylinder than the smooth one. These features are similar to that of dimples or

grooves on the surface of circular cylinder.

4. The indentations have a significant influence on the near-field velocity and pressure values. Farther away from the surface, the velocity and pressure curves for both indented cylinders appear to collapse into a single profile. The different forces acting on the indented cylinder appear to be a surface phenomenon rather than induced behavior by the wake region. By identifying the vortical structures in the wake region, it appears that although indentation alters the flow near the cylinder surface, they do not change the nature of flow in the wake region.

# Chapter 6 Simulation of Flow Past Half-Indented Circular Cylinders

## Circular Cylinders

In this chapter, numerical investigations on aerodynamic characteristics of flow around half-indented circular cylinders were studied.

In the first section, simulations on cylinders with uniform indentation locates in the frontal part were conducted. To identify the effect of indentation's size on the flow characteristics, three cylinders with various indentation diameters and depths were taken into concerns. In the second section, cylinders with different indentation arrangements were set up to investigate their aerodynamic characteristics. The aerodynamic forces, pressure coefficient distribution, correlation coefficients and wake properties were studies to reveal the mechanism of indentations.

### 6.1 Half uniform-indented circular cylinders with various indentation sizes

#### 6.1.1 Case setup

In this section, three circular cylinders with different indentation sizes (width and depth) are used. The size of indentations is shown in Figure 6.1. Among them, Medium size indentation (M2) has the same width ( $0.1D$ ) and roughness height  $k$  ( $0.02D$ ) with the fully uniform-indented cylinder used in Chapter 5. Based on the size of M2, small size indentation (S1) and big size indentation (B3) were depicted with expand ratios of 0.75 and 1.5, respectively. Thus, the roughness coefficient  $k/D$  for three cases are 0.015, 0.02 and 0.03, respectively.

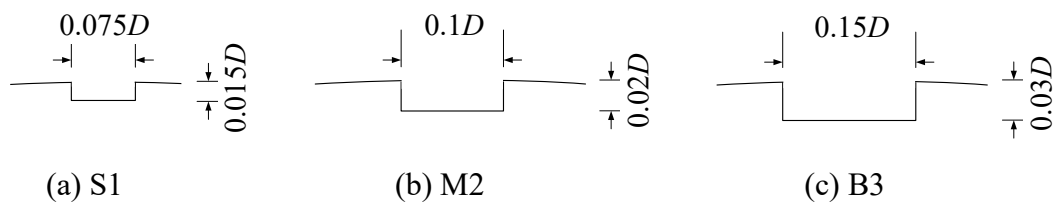


Figure 6.1 Different sizes of indentation

The design picture of the half uniform-indented cylinders is shown in Figure 6.2. There are 8 rows of indentations locate on the frontal part of the cylinders. Those indentations are arranged at an equal angle interval of  $22.5^\circ$ . A center to center span-wise distance between two adjacent indentations is  $2w$ , which equals to two times of width for indentation in different models. The 3-D models of three cylinders are shown

in Figure 6.3.

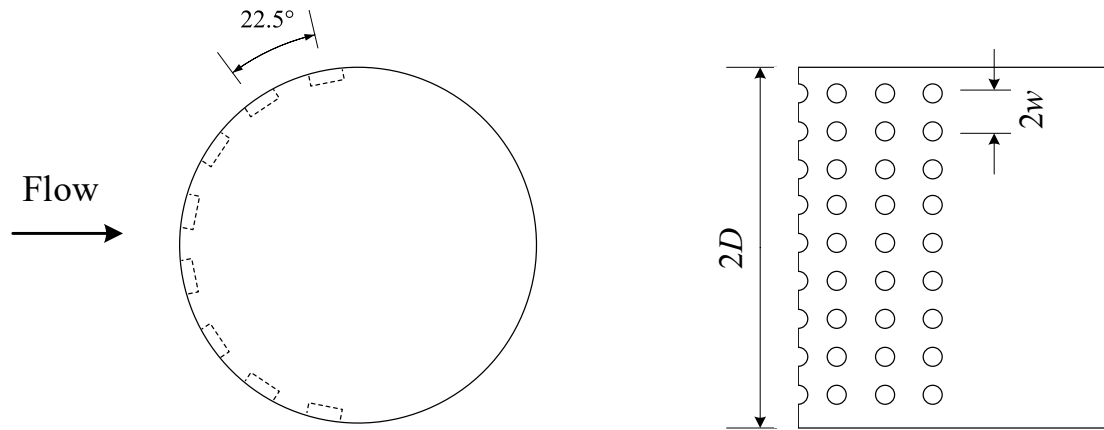


Figure 6.2 Geometry of the half uniform-indented circular cylinder

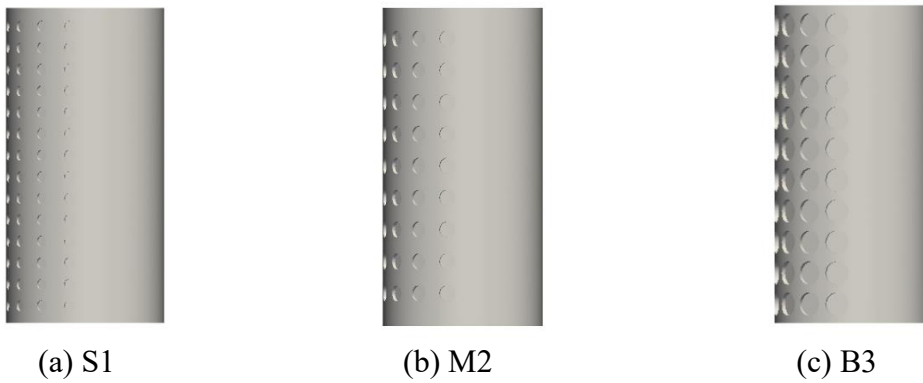


Figure 6.3 Geometries of the cylinders with various indentation sizes

For all the cases, unstructured polyhedral mesh has been adopted. The meshing size such first grid spacing, global and local mesh setting are the same with Chapter 5.1. The 3-D LES numerical details and boundary conditions are both the same with former Chapter. Therefore, the introduction of numerical methods is omitted here.

### 6.1.2 Aerodynamic forces

Table 6.1 Aerodynamic forces of three models

No.	$C_d$	$C_{l, rms}$	$St$
ORI	0.999	0.136	0.213
S1	0.963	0.131	0.216
M2	0.977	0.148	0.215
B3	0.968	0.103	0.212

Table 6.1 shows the aerodynamic forces of four models (including the smooth cylinder) and their Strouhal Numbers. Reductions of average drag force coefficients for three half-uniform indented cylinders are identified when compared to ORI. The reductions

for S1, M2 and B3 models are 3.6%, 2.2% and 3.1%, respectively. Compared with the results of fully indented cylinders, the reduction of drag forces here is slightly larger due to different indented densities and indentations size.

For the fluctuating lift force coefficient, a much smaller value of 0.103 on B3 model is achieved. However, the ones of S1 and M2 models do not show great mitigation, indicating that a larger size of indentation may result in a smaller lift force. The frequency of the lift force, expressed by the Strouhal number ( $St$ ), is quite stable at a constant value of around 0.21 for all the cases.

Figure 6.4 to 6.6 presents the spatial temporal distribution of drag and lift force coefficients of three half-uniform indented models. Similar to the fully uniform-indented models, parallel filaments of darker blue perpendicular to z-axis in drag force plots is observed along the time histories. These filaments are the places where indentations locate, indicating a mitigation of drag force. The  $C_l$  plots of all the cases are mainly consisted of repeated filaments of red and blue, with each taking a band width of around 2.5 non-dimensional seconds, which represents the periodic lift force acting upon the cylinder.

As discussed above, great variations of the force coefficients are observed in the span-wise direction due to the existence of indentations. Therefore, the spatial-temporal distributions of the force coefficients (Figure 6.4, 6.5 and 6.6) are condensed by taking the temporally averaged (for  $C_d$ ) or rms values (for  $C_l$ ) for each span-wise section. The results are presented in Figure 6.7.

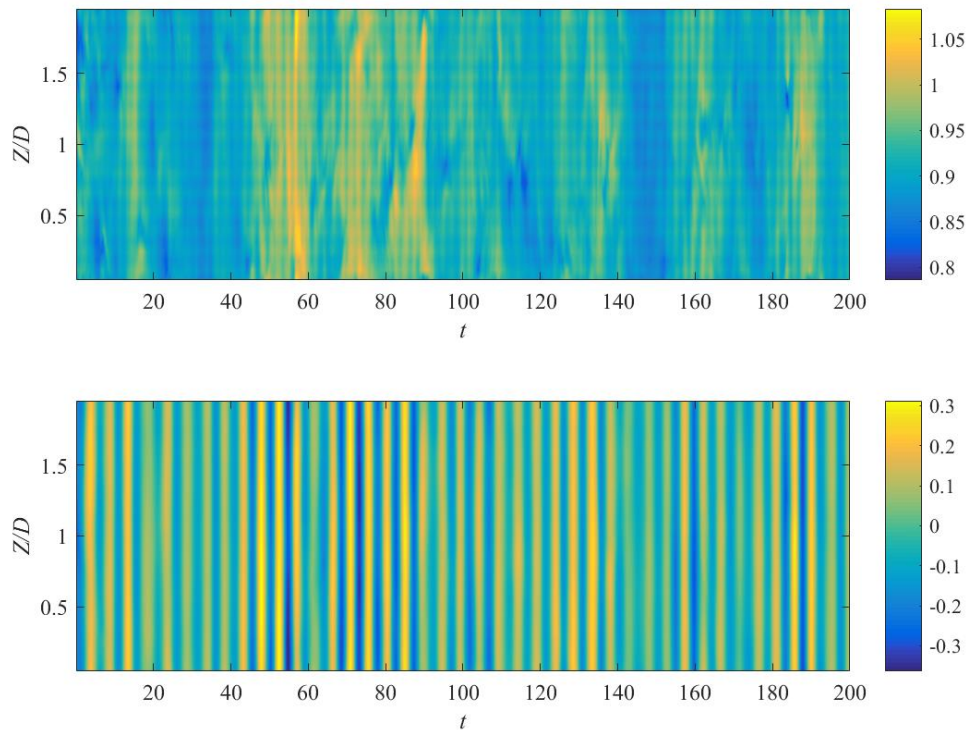


Figure 6.4 Spatial-temporal distribution of force coefficients (Case S1)  
(upper figure,  $C_d$  ; lower figure,  $C_l$  )



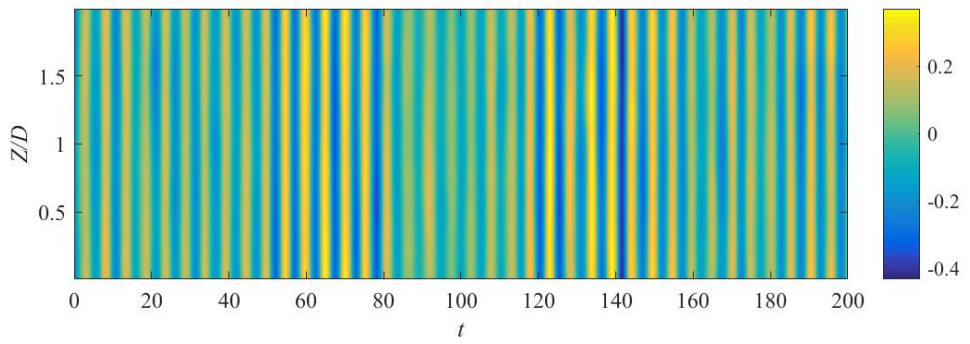
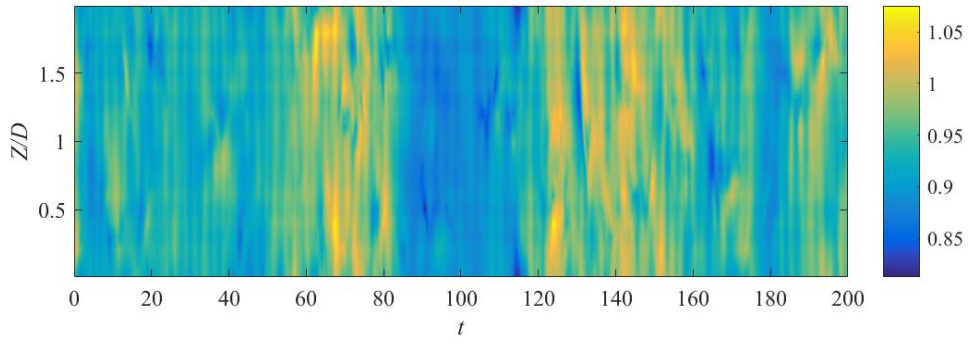


Figure 6.5 Spatial-temporal distribution of force coefficients (Case M2)  
(upper figure,  $C_d$ ; lower figure,  $C_l$ )

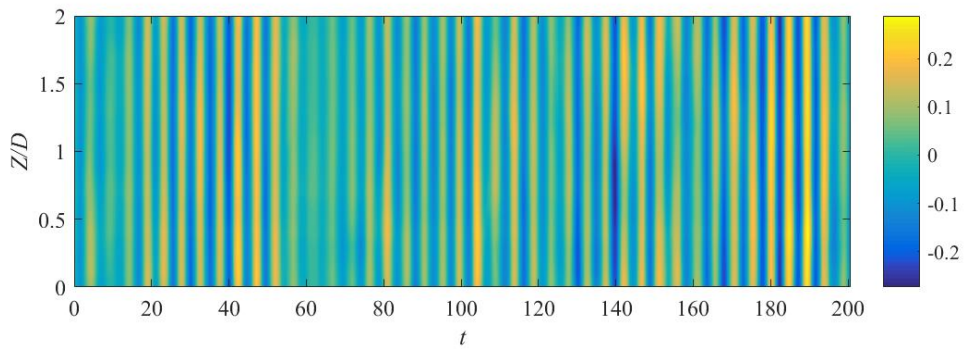
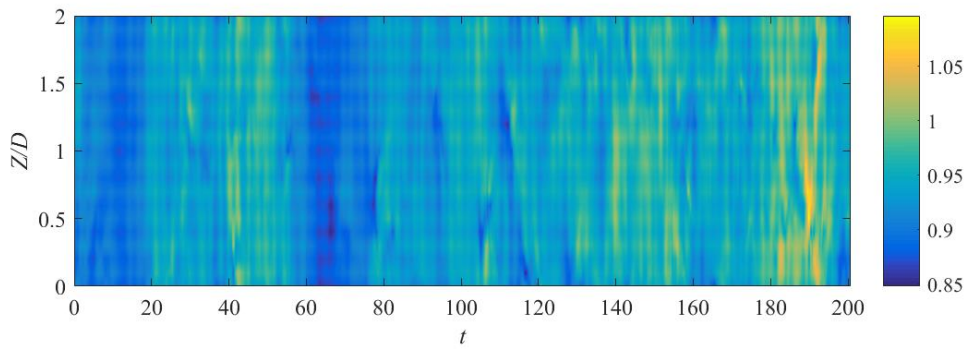
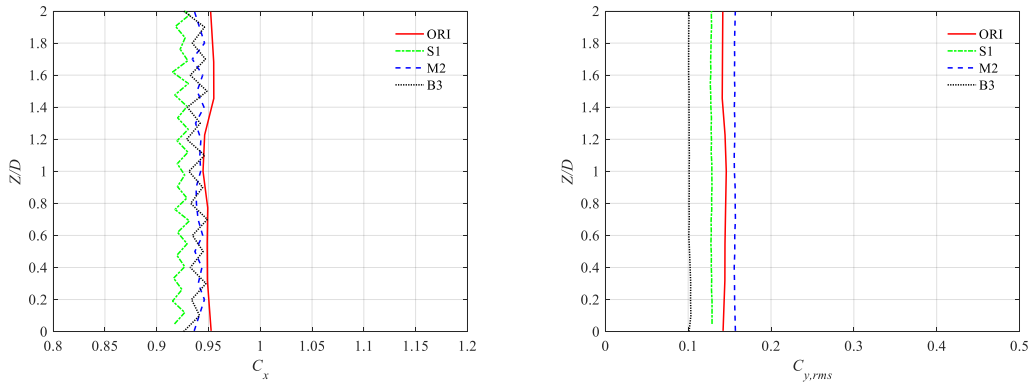


Figure 6.6 Spatial-temporal distribution of force coefficients (Case B3)  
(upper figure,  $C_d$ ; lower figure,  $C_l$ )



(a) Average drag forces coefficients (b) rms lift forces coefficients

Figure 6.7 Sectional forces coefficients

A general trend to notice is the zigzag variations in the sectional  $C_d$  of indented models when compared to the constant value of smooth cylinder. For the indented cases,  $C_d$  reaches its maximum at the smooth surface and falls to the minimum at the indentations. Among the three models, the fluctuation of drag forces is greatest for B3 due to a larger size of indentation. Unlike drag force, constant values of sectional  $C_l'$  for all the cases are detected.

### 6.1.3 Pressure distributions

Since the drag and lift force coefficients are calculated from pressure coefficient  $C_p$ , it is instructive to have a look at the pressure distribution around the cylinder and along the cylinder circumference.

#### Pressure distributions around the cylinder

Figure 6.8 presents the mean pressure coefficients (hereinafter  $C_p$ ) at the wake region and near field of cylinders.

In the wake region, minimum negative  $C_p$  is detected at about 1D to the center of cylinder for all the cases. The minimum negative  $C_p$  increase to -1.04 and -1.05 for M2 and B3 models when compared to the value of -1.16 for ORI.

In the near field of cylinders, distinctive features could also be noted. The  $C_p$  of ORI model decreases from highest positive  $C_p$  at the stagnation point and reach its minimum before the separation point. The pressure changes smoothly without abrupt increase or decrease. As for the indented models, the contour lines of  $C_p$  gather at the edge of indentations. The pressures seem to be partitioned by the indentations, especially in the case with larger indentation sizes (M2 and B3).

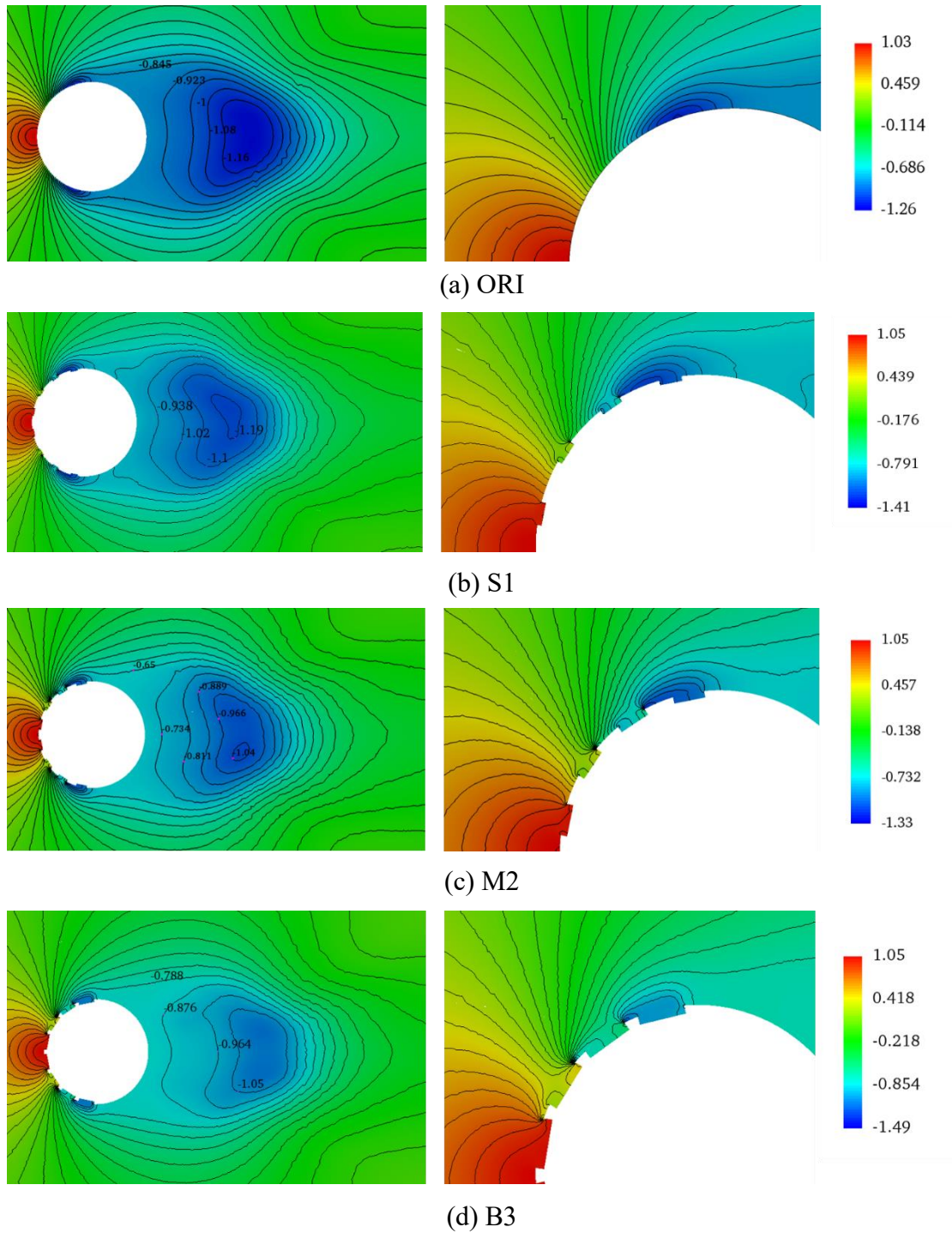


Figure 6.8 Pressure distributions around the cylinders (left: wake region, right: near field of cylinder)

### Pressure distributions along the cylinder circumference

Surface pressure distributions from a view of  $45^\circ$  are shown in Figure 6.9. For all the cases, a zig-zag distribution of  $C_p$  guided by the indentations could be seen in the frontal side of cylinders. In terms of the  $C_p$  value, same maximum  $C_p$  of 1.05 is detected on three models due to the same inflow condition. However, the minimum  $C_p$  of indented

cylinders is noticeably smaller than ORI (a value of -1.2, Figure 5.5).

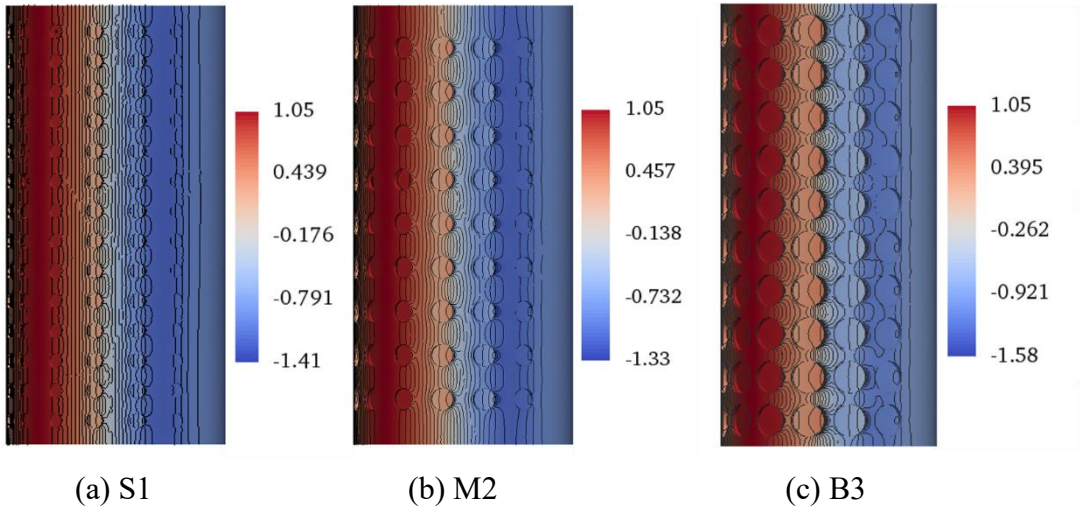
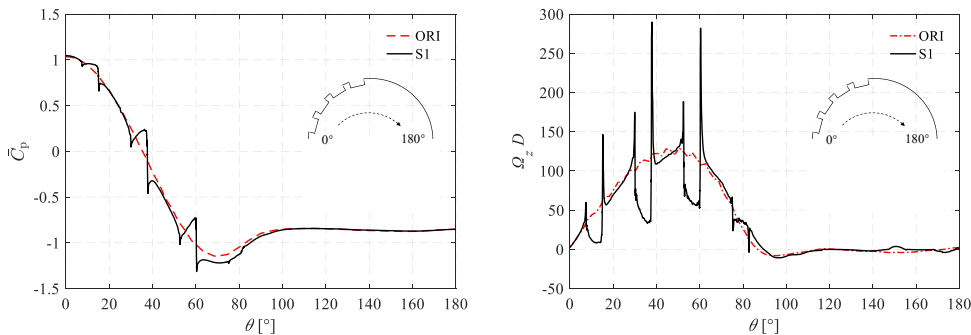


Figure 6.9 Pressure distribution on cylinder surfaces

Depicted in Figure 6.10 are the mean  $C_p$  and span-wise vorticity of different cylinders and at different characteristic locations.

Some interesting features could be noticed in Figure 6.10. Firstly, Similar to the fully indented cylinders, a zig-zag pressure distribution could be seen in the wind-ward side, and the oscillations in the zigzags exacerbate as  $\theta$  increases. This behavior seems to be sensitive to the indentation sizes. For example, lower negative pressure is detected at the edge of indentations with the increasing indentation size, resulting in a greater pressure recovery. Such features are similar to the cactus surface cylinders, which is studied by Talley et al [55] and Talley & Mungal [56] In their work, a total of 24 V-shaped cavities along the cylinder circumference with three different cavity depths were studied at high Reynolds number ( $2 \times 10^4$  to  $2 \times 10^5$ ). The pressure recovery appeared to increase with increasing roughness of the cavities, which is similar to the current study.

The qualitative trends are similar to the fully indented cylinders in terms of span-wise vorticity discussed in section 5.4. The increase of span-wise vorticity at the edges and reduction at the pits are detected for all the cases. The main difference among the three indented cases is that the reduction range is wider for a larger width of indentations. That is to say, the integrated value of B3 model is smaller than the other two, indicating a mitigation to viscous drag force.



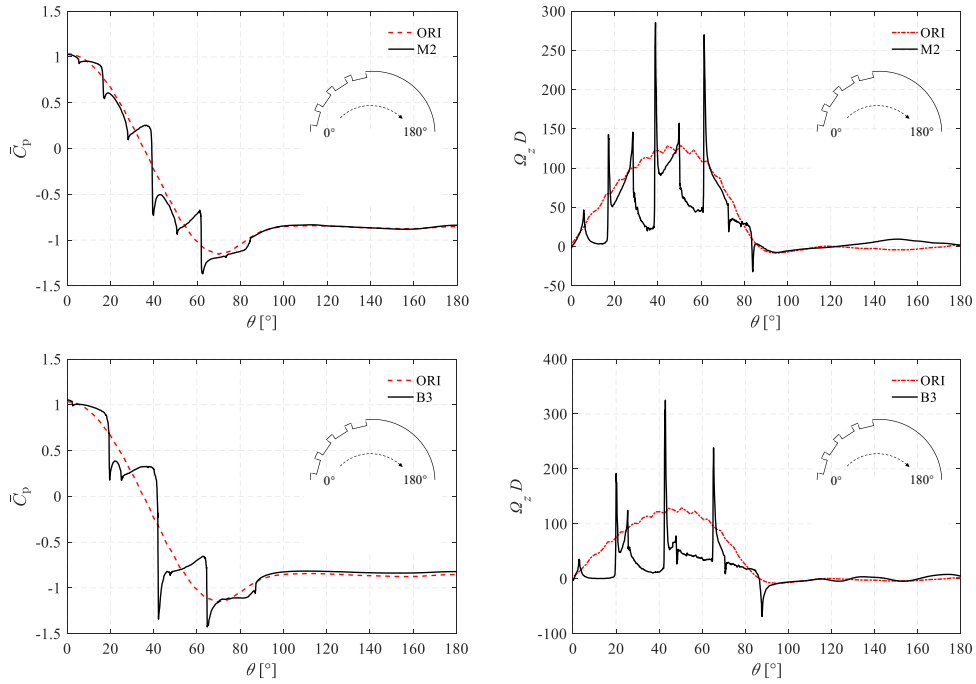


Figure 6.10 Comparison results of cylinder circumference  
(left: pressure coefficients, right: span-wise vorticity)

## 6.1.4 Correlation coefficients

In this section, the span-wise and stream-wise correlation of the flow variables, such as the pressure coefficients, aerodynamic force, are important measurements of the 3-dimensionality of the flow.

The correlation coefficient is defined by:

$$\rho(z_1, z_2) = \frac{E[(z_1 - \mu_{z_1})(z_2 - \mu_{z_2})]}{\sigma_{z_1} \sigma_{z_2}} \quad (6.1)$$

in which  $\mu_x$  and  $\sigma_x$  are the average and standard deviation of the variable  $x$ . Here,  $z_1$  and  $z_2$  present the force coefficients at any two different locations.

### Stream-wise correlation coefficients

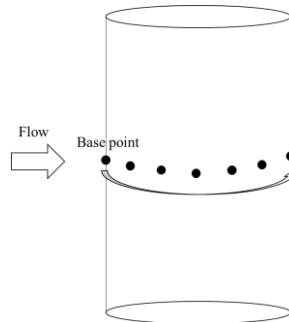


Figure 6.11 Sketch of pressure taps and reference tap

Figure 6.11 shows a sketch of the pressure tap locations. Wind is applied from left to

right. For each section, the reference tap locates at the foremost point of the cylinder. The stream-wise correlation coefficients between the other taps on side face of cylinders and the reference tap were calculated. Then the contour of correlation coefficients on the side faces were plotted, as depicted in Figure 6.12.

The stream-wise correlation of ORI decreases gradually as the flow evolves and reaches to 0 at the leeward side. As for the three indented cases, the correlation decreases significantly at the leading side of cylinder. The correlations are weakened due to strong impingement, flow separation and recirculation at those indentations.

In the span-wise direction, the contours of indented models are partitioned into dark blue and light blue bands. Wider bands are detected for B3 models, owing to a larger distance between two adjacent indents. While no big correlation variations are observed for ORI model.

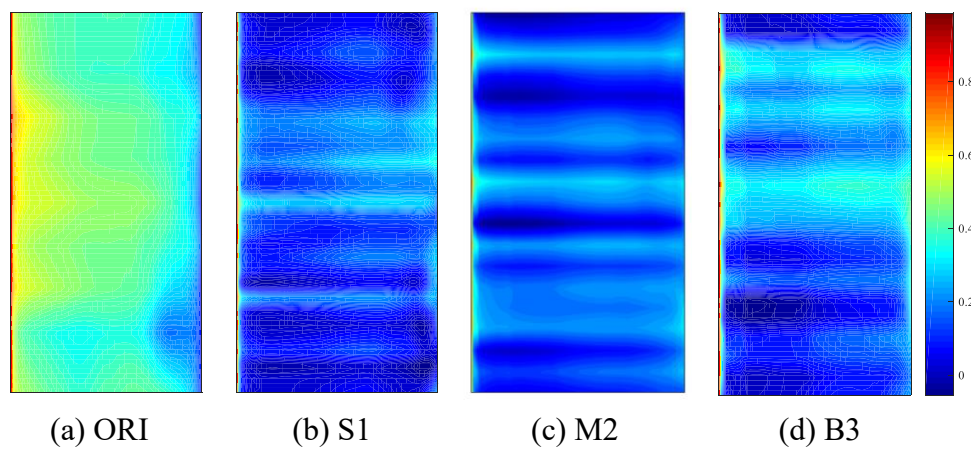


Figure 6.12 Stream-wise correlation contour of  $C_p$

### Span-wise correlation coefficients

As discussed in section 6.1.2, strong zig-zag variations of sectional drag force coefficients are detected for indented cylinders. It is thus interesting to inspect the differences in the correlations in span-wise direction.

Taking the cylinder bottom end as the reference point, the sectional  $C_d$  and  $C_l$  correlation coefficients  $\rho$  of the four cylinders are shown in Figure 6.13.  $\rho(0, 2)=1$  is a reflection of the periodic boundary condition used in the span-wise direction, which means that only half of the cylinder length could be used for correlation coefficient analysis.

The smooth cylinder is best correlated in drag force, its correlation coefficient staying as high as 0.7. Considerably lower correlation coefficients of 0.6 are observed in the three indented cylinders. Among them, the correlations of larger indented cylinders, such as M2 and B3, decrease more sharply when compared with S1.

The correlation coefficients of lift forces for all the four cases are similar, with a well correlated value of over 0.95. Since the lift forces are related to the vortex shedding process along the span-wise direction. It is thus clear that the surface indentation does not have profound effects on the vortex shedding process of flow past a circular cylinder

at  $Re=3900$ .

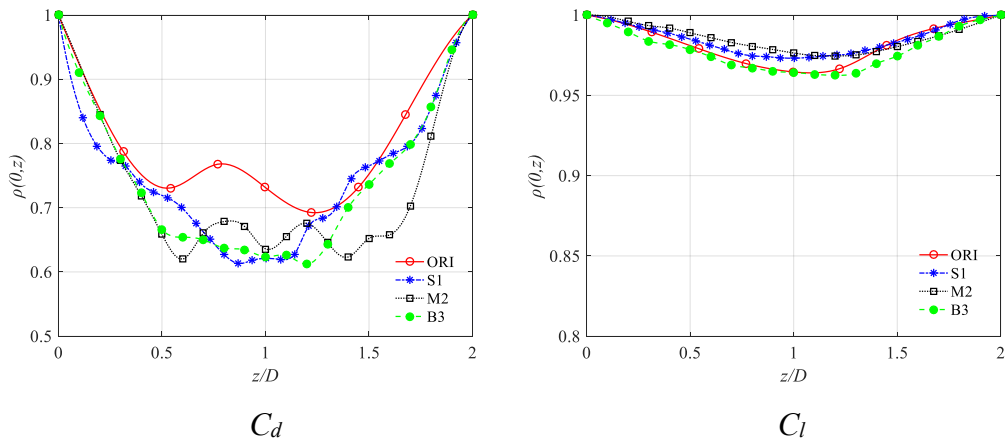
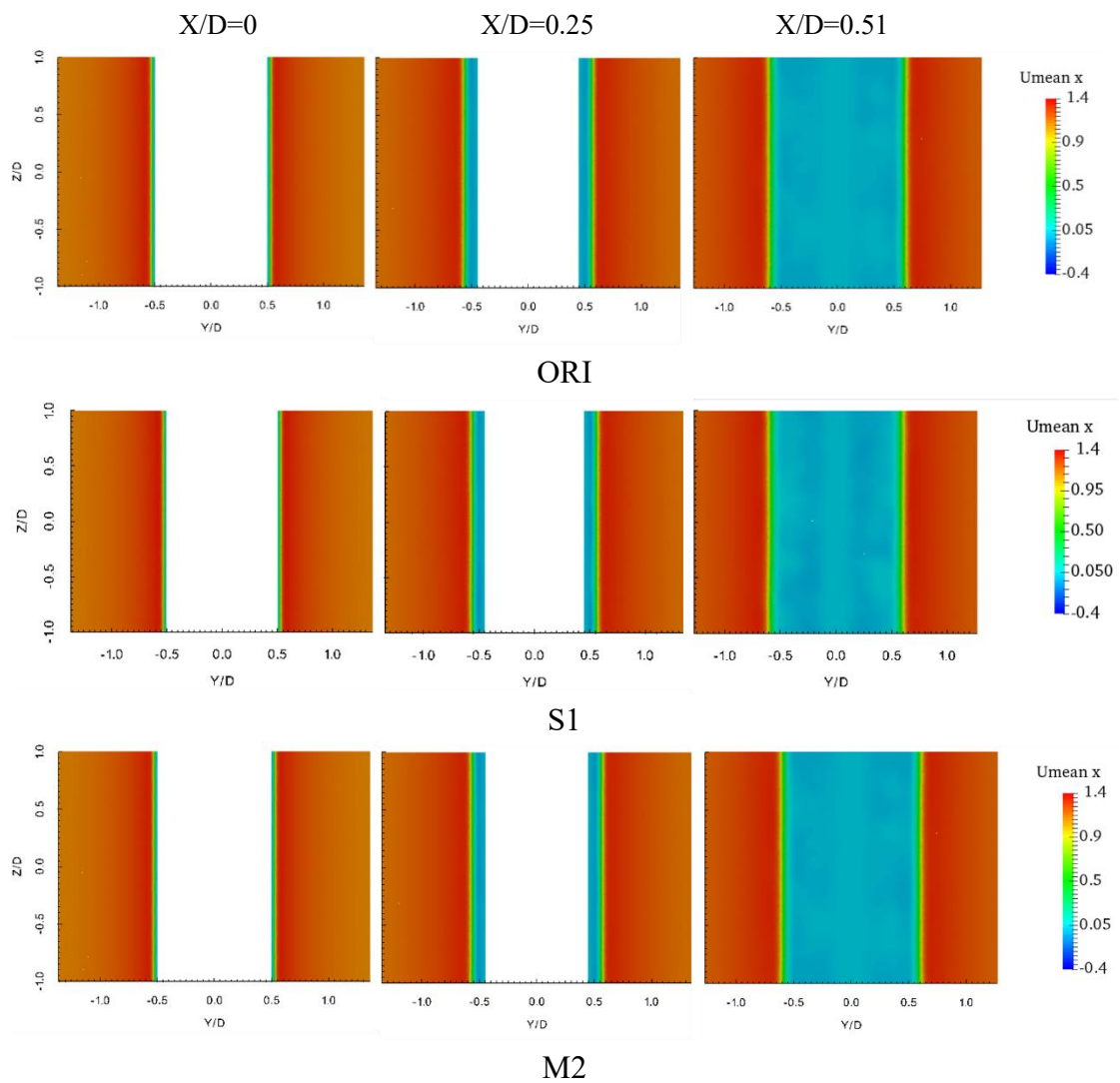
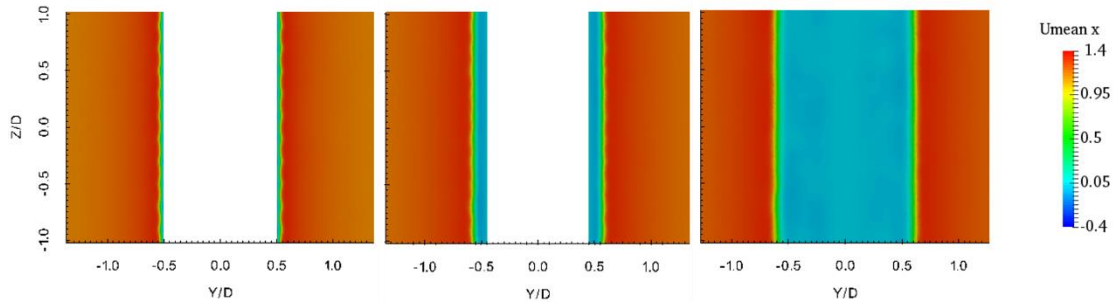


Figure 6.13 Span-wise correlation coefficients of force coefficients

### 6.1.5 Wake properties

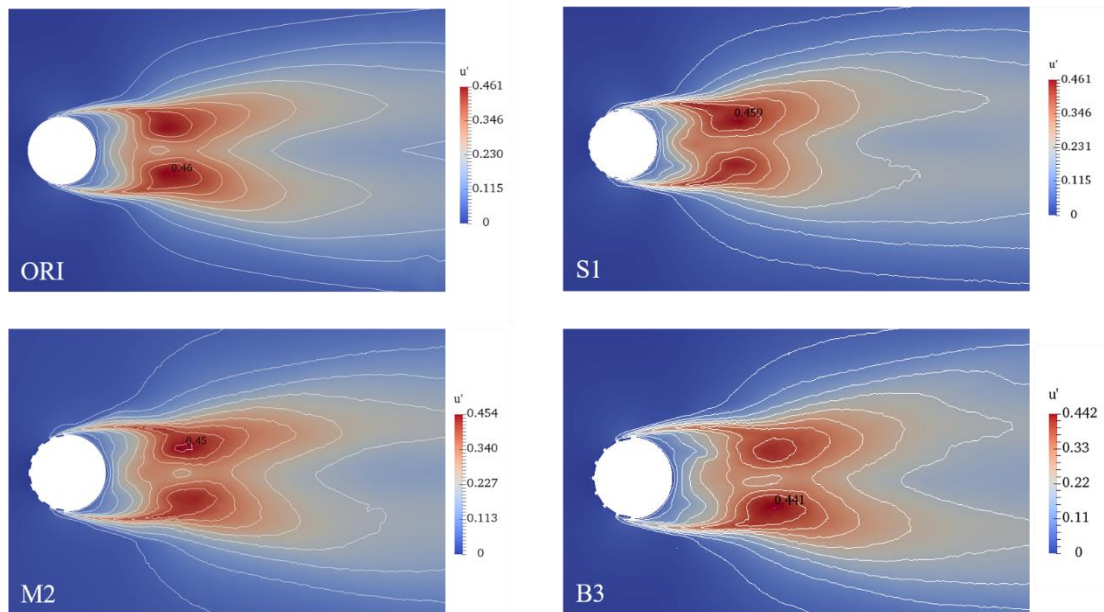




B3

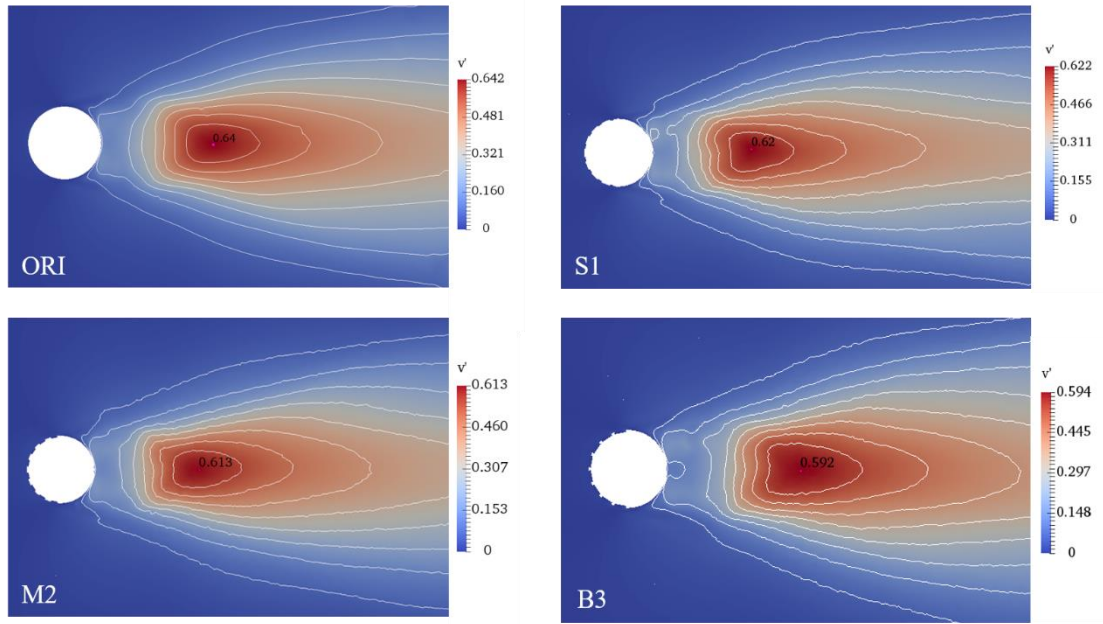
Figure 6.14 Mean stream wise velocity in the y-z planes for the indented cylinders

Figure 6.14 presents the evolution of the mean stream-wise velocity in the y-z planes at several locations after the separation points for smooth cylinder and three indented cylinders. It could be observed that velocity profiles show considerable changes as the slice position shifts to the downstream locations. Similar to ORI, parallel smooth shear layers can be identified at different slice positions. In case of B3 model, Unlike the other two indented cases, the shear layers are strongly distorted near the vicinity of large size of indentations. At  $X/D=0.25$ , the effect of indentations is felt less and the undulation becomes diminishing small at  $X/D=0.51$ . This is a proof that the indentation does not have profound effect on the wake topologies.



(a)  $u'$





(b)  $v'$

Figure 6.15 The root mean square of velocity contours in the wake region

Although the wake topologies are not changed by the indentations, as discussed in the former section that the lift force decreases for B3 model significantly. It is thus interesting to investigate the velocity distributions in the wake region. The root mean square of the x-velocity,  $u'$ , and the y-velocity,  $v'$ , were calculated, as shown in Figure 6.15. The maximum value of each figure was also marked.

The  $u'$  contour of four cases are in similar pattern and values. In terms of  $v'$ , the velocity fluctuations of indented models are lower than that in the smooth cylinder. The maximum value also decreases with an increasing indent size. The reduction of B3 model reaches 7.5%, indicating a mitigation in lift force (section 6.1).

### 6.1.6 Boundary layer profiles

As shown in the former Chapter, the indentation we used in this study has the similar effect with dimple or groove on energizing the boundary layers. It is thus suggested that the influence of roughness (here the size of indentation) may be similar to that of dimpled or grooved ones. A lot of researches haven been done to reveal the effect of roughness coefficient on reducing the drag crisis of circular cylinders [26] [32] [57]. It was proved that higher roughness coefficient could contribute to an earlier drag crisis for both grooves and dimples.

Therefore, a similar method on boundary layer profiles of velocities used in section 5.4.2 is adopted here. Unlike section 5.4.2, the boundary layer profiles of three cases cannot be compared directly due to the different width of indentations. It is thus decided that boundary layer profile at each indentation are compared to the corresponding one of the smooth cylinder. Depicted in Figure 6.16, The boundary layer profile of a smooth

cylinder and the increased one of an indented cylinder are plotted together, then the shadowed area is the difference between them.

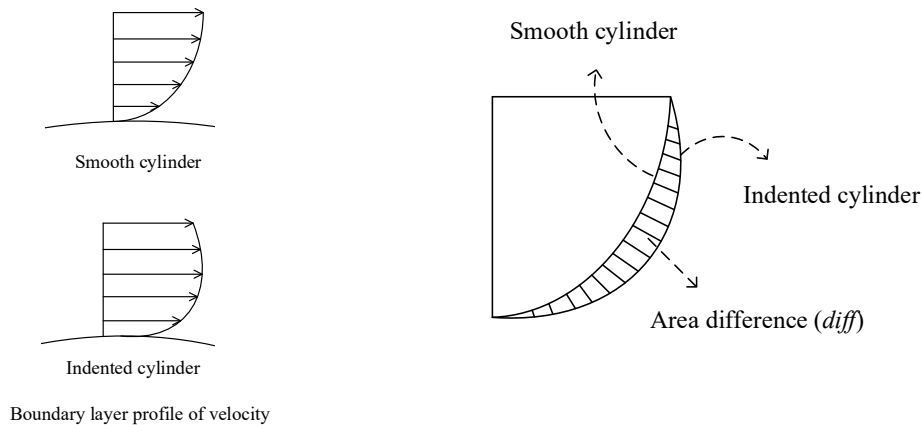


Figure 6.16 The sketch of calculation about the area difference of boundary layer profiles between a smooth cylinder and an indented one

The non-dimensional difference  $diff$  is defined by:

$$diff = \frac{A_{ind} - A_{ori}}{A_{ori}} \times 100\% \quad (6.2)$$

in which  $A_{ori}$  and  $A_{ind}$  are the integral areas of smooth cylinder and indented cylinder, respectively.

Thusly, a larger positive  $diff$  corresponds to larger velocities, implying a more energetic boundary layer. The results are shown in Figure 6.17. For indentations at row1 and row2, higher  $diff$  value is identified with an increasing roughness. At row3, the value of  $diff$  for B3 is slightly lower than M2, while the smallest remains S1.

As for row4, the  $diff$  value decreases sharply for rougher cylinders M2 and B3. This feature could be explained with the aid of Figure 6.14. The flow detaches at the trailing edge of indents and reattaches at the downstream surface in terms of small indent size (S1). Thusly the  $diff$  value of S1 case keeps increasing as flow evolves. However, since the location of row4 is quite closed to the separation point, the detached flow could not reattach to the surface owing to a larger size of indent (M2 and B3). Consequently, the reverse flow takes place at row4 and decreases the  $diff$  value significantly.

The above results could proof that the boundary layers are much more energized by larger sizes of indentation, which could trigger the transition for boundary layers from laminar to turbulence easier and delay the separation. Thusly the drag crisis happens at a lower critical Reynolds number.

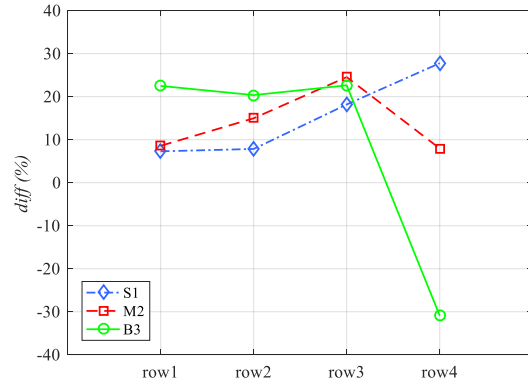


Figure 6.17 Difference of boundary layer profiles

## 6.2 Half-indented circular cylinders with various indentation arrangements

### 6.2.1 Case setup

In this section, three circular cylinders with different arrangements of indentation are used. The indentation sizes of three cases are the same with M2 cases used in section 6.1, with a roughness height and width of  $0.02D$  and  $0.1D$ , respectively. Figure 6.18 shows the top view and side view of models with different indentation arrangements.

Among them, the case with vertical interval indentation distribution is named as MV. The other two cases, on which the indentations are horizontal interval distributed, with sparse and dense indents are named as MH and MHD, respectively. The 3-D models of three cylinders are shown in Figure 6.19. For all the cases, unstructured polyhedral mesh has been adopted as section 6.1.

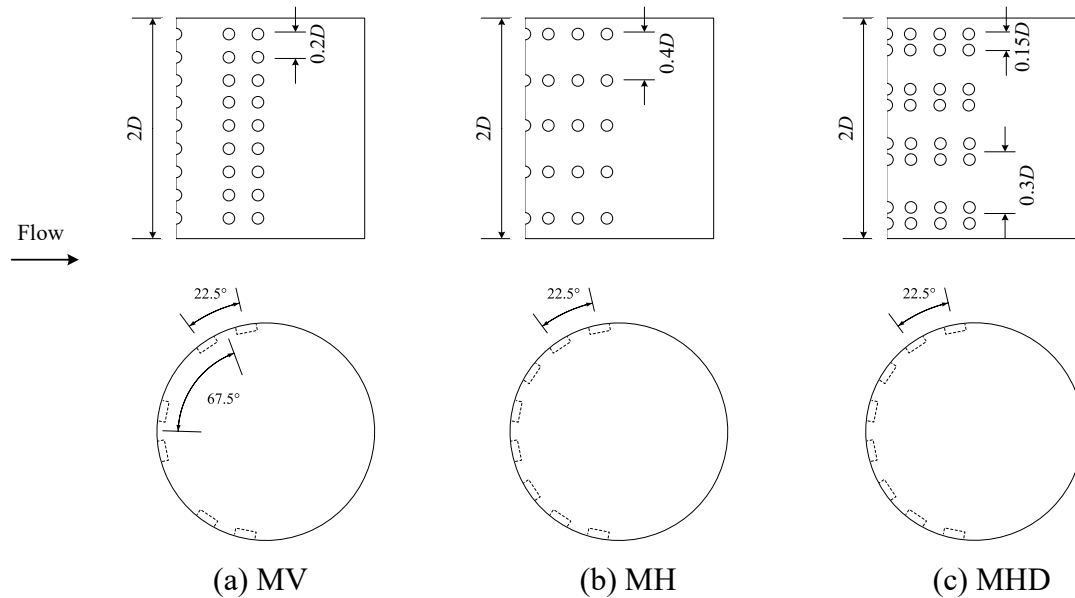


Figure 6.18 Different arrangement of indentations

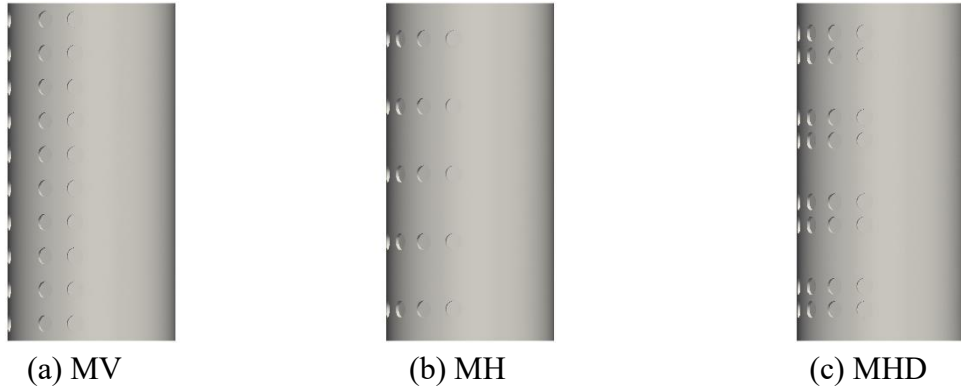


Figure 6.19 Geometries of the cylinders with various indentation arrangements

## 6.2.2 Aerodynamic forces

Table 6.2 Aerodynamic forces of three models

No.	$C_d$	$C_{l, rms}$	$St$
ORI	0.999	0.136	0.213
M2	0.977	0.148	0.215
MV	0.990	0.178	0.214
MH	0.985	0.160	0.215
MHD	0.983	0.151	0.219

Table 6.2 shows the aerodynamic forces of five models (including the smooth cylinder and M2 cases for comparison) and the Strouhal Number. The reduction of average drag force coefficients of MH and MHD models are limited, with mitigations of 1.4% and 1.6%, respectively. The drag force for MV case is almost the same with the smooth cylinder. For all the three cases, the drag values are larger than that of M2 case, owing to fewer indents on the surface. The similar trend to drag force also happens in lift force coefficients.

Figure 6.20 to 6.22 presents the spatial temporal distribution of drag and lift force coefficients of three half-uniform indented models. The span-wise averaged drag force coefficient curves are also plotted in Figure 6.23.

Similar to the M2 case, parallel filaments of darker blue color perpendicular to z-axis in drag force plots is observed along the time histories for all the cases. The distance of dark blue filaments is larger for MH and MHD, owing to the correspond distance between two adjacent indents. This is one of the results of the indent arrangements.

From Figure 6.23, the aforementioned features can be identified clearly. The sectional drag force curve of MV case shows a similar pattern to M2 case. Since the indentation distributes uniformly in the z-axis, the decrease at the indent and increase at the plain surface, making the curve into a zigzag one. For the other two cases, MH

has a larger distance between two indents and MHD has unevenly distributed indents. Thusly at the indentations, the abrupt decrease in the drag curve can be identified clearly. When compared to MV case, the drag reduction at the indents are more significant for MH and MHD cases. This is because less indentations (3 rows) are arranged on the circumference of MV, while the other two models have fully distributed indentations on the circumference.

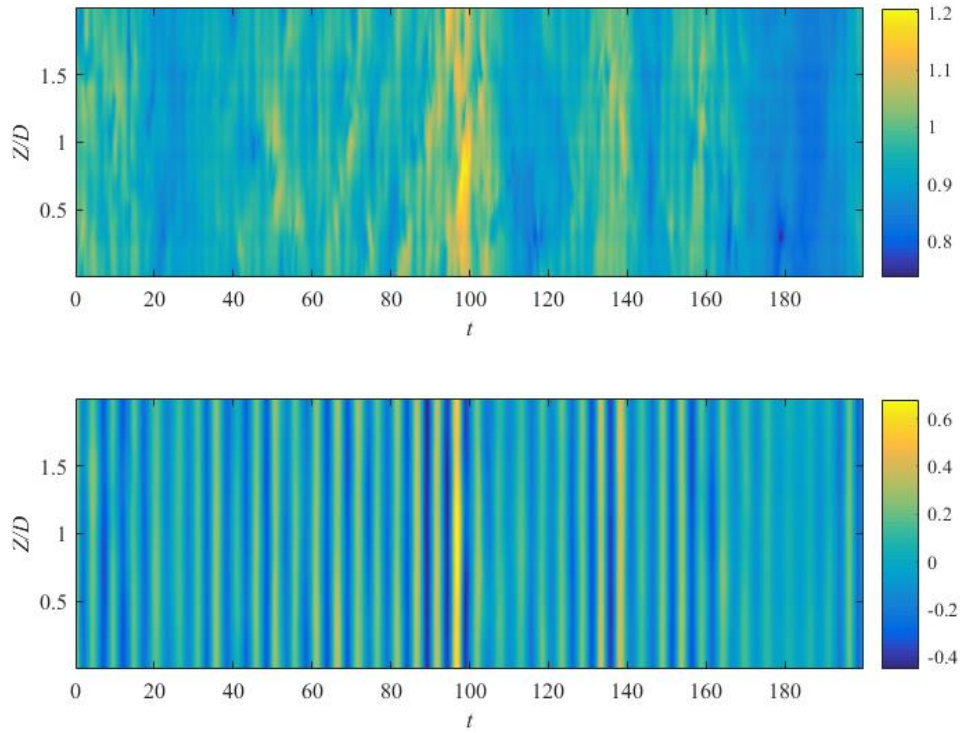
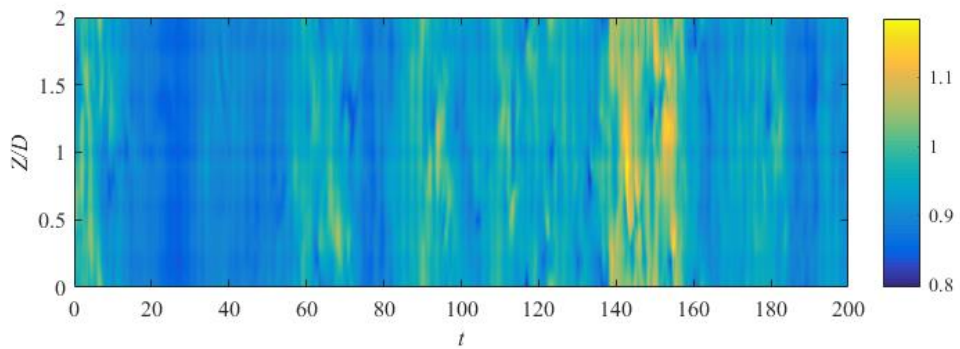


Figure 6.20 Spatial-temporal distribution of force coefficients (Case MV)  
(upper figure,  $C_d$  ; lower figure,  $C_l$ )



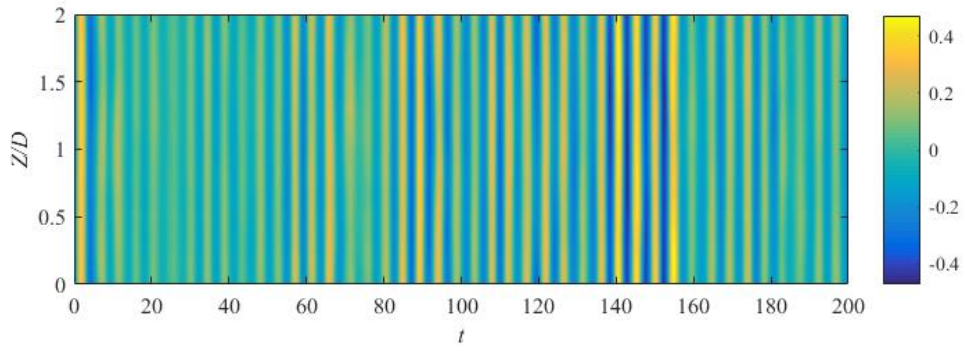


Figure 6.21 Spatial-temporal distribution of force coefficients (Case MH)  
(upper figure,  $C_a$  ; lower figure,  $C_l$ )

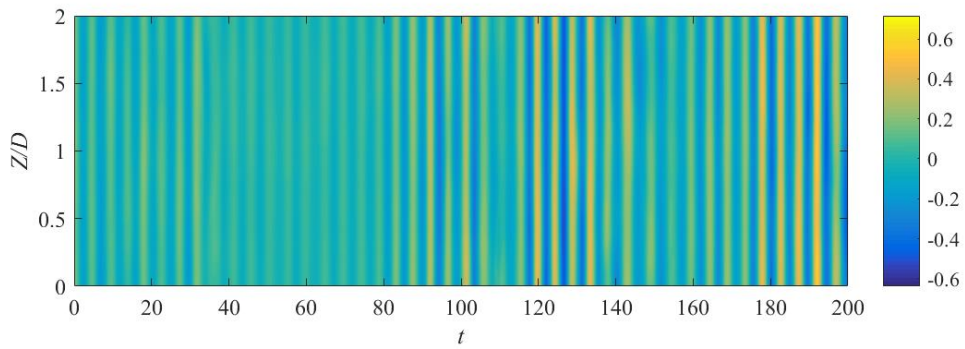
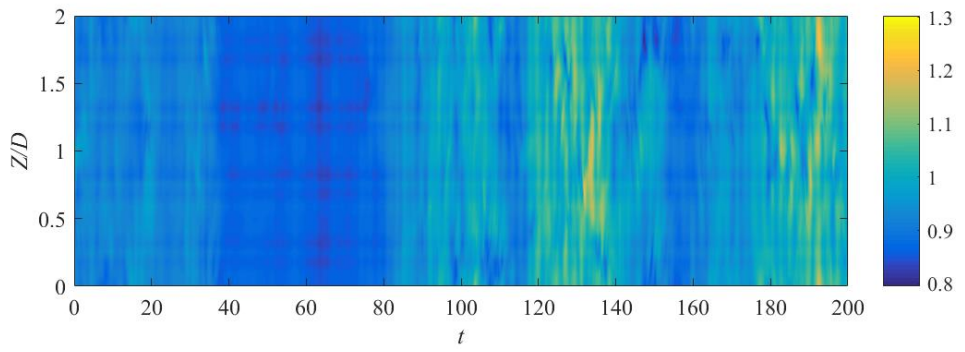


Figure 6.22 Spatial-temporal distribution of force coefficients (Case MHD)  
(upper figure,  $C_a$  ; lower figure,  $C_l$ )

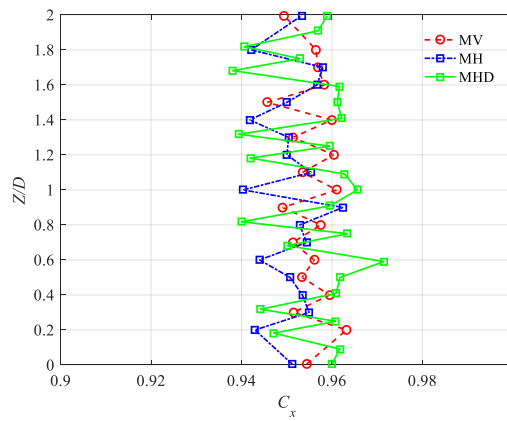


Figure 6.23 Sectional drag forces coefficients

### 6.2.3 Pressure distributions

Surface pressure distributions from a view of  $45^\circ$  are shown in Figure 6.24. For all the cases, a zig-zag distribution of  $C_p$  guided by the indentations could be seen in the frontal side of cylinders. It can be clearly observed that for the plain surface the contour lines of pressure coefficients are parallel distributed and perpendicular to the flow, such as the area between two rows of indentations in MV case. Since the indentations are arranged various in horizontal and vertical direction, the pressure coefficient distributions along the circumference and in span-wise direction are taken into concern separately.

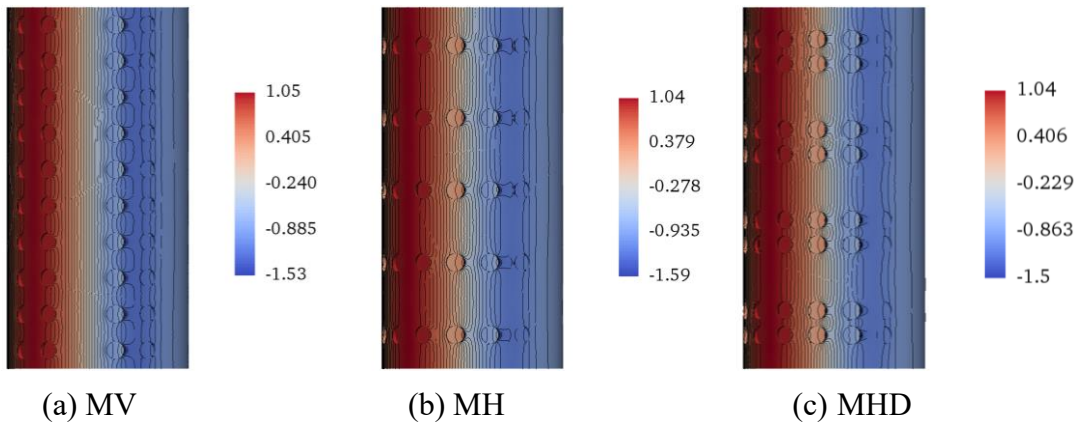


Figure 6.24 Pressure distribution on cylinder surfaces

Depicted in Figure 6.25 and 6.26 are the mean  $C_p$  and span-wise vorticity of different cylinders and at different characteristic locations. For comparison, the results on both plain and indented surfaces of indented models are plotted, as well as the results of the smooth cylinder.

For both  $C_p$  and span-wise vorticity curves, the pattern and value of MH and MHD cases are similar to that of M2. While the results on the plain circumference is close to that of smooth cylinder. It seems that the plain surfaces on the indented cylinders have the similar characteristics with a smooth cylinder. As for MV case, the  $C_p$  and vorticity curves become smooth between 20 and 45 degree, owing to the absence of indentation at this location. Thusly, the reduction of integrated vorticity is not significant when compared to the other two cases.

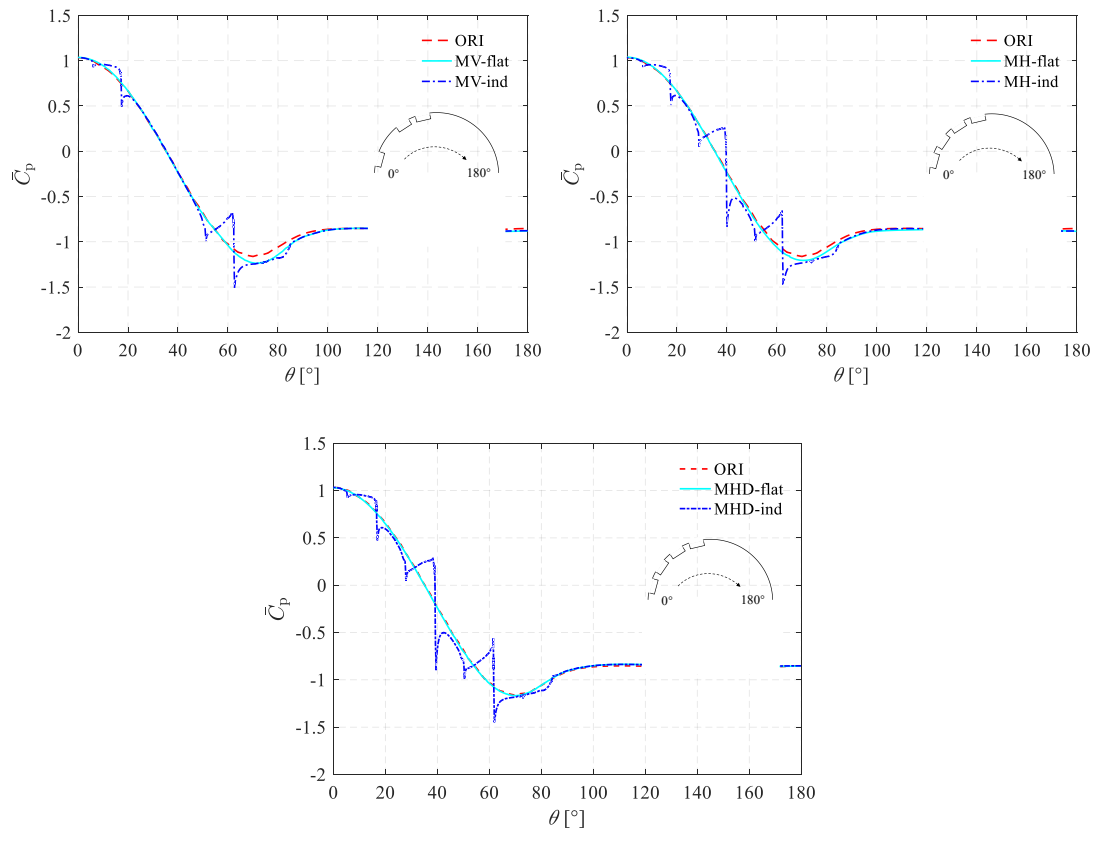


Figure 6.25 Mean pressure coefficients of cylinder circumference

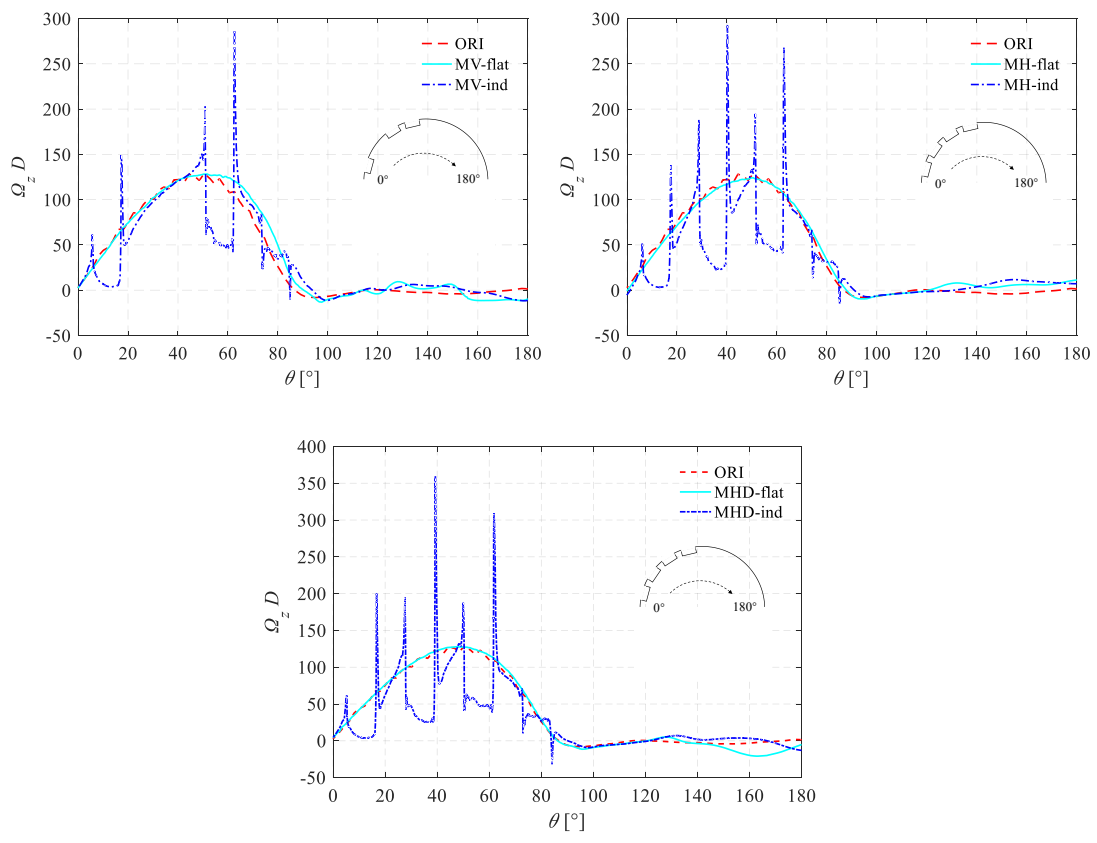
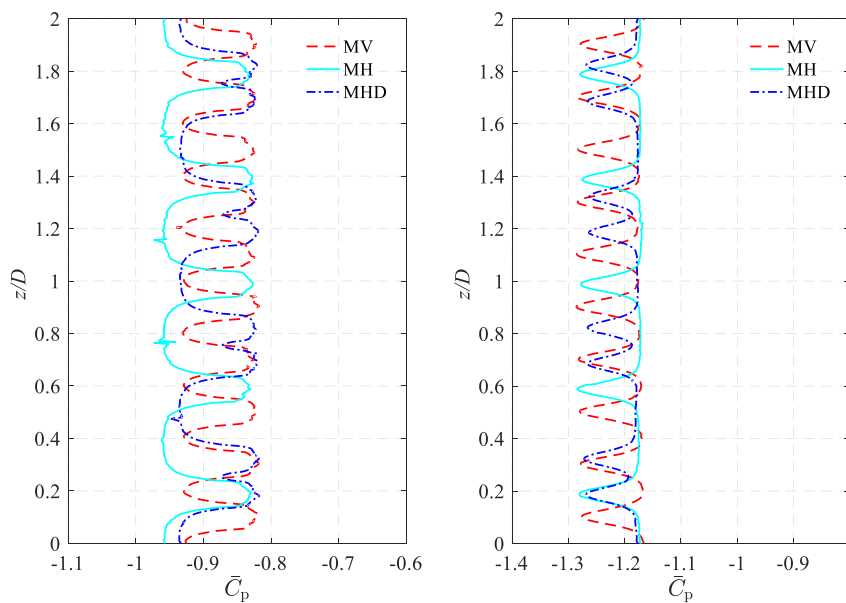


Figure 6.26 Span-wise vorticity of cylinder circumference



In span-wise direction, since the distances between two adjacent indents are different for three cases, thusly it is interesting to identify the effect of this parameter. Figure 6.27 presents the mean pressure coefficient at the centerline and trailing edge of indentations row3 for three models (it is row2 for MV cases).



(a) centerline of indent

(b) trailing edge of indent

Figure 6.27 Span-wise mean pressure coefficients at indentation row 3

At the centerline of indents, the  $C_p$  is lowest at the plain surface and largest at the center of indents. A zig-zag curve along the  $z$ -axis are observed for all the cases. The maximum  $C_p$  values are almost the same for the three cases. In terms of the minimum  $C_p$ , the smallest value is detected on MH with a largest distance  $0.4D$  between two adjacent indents. The largest one is identified at the narrower space between two indents of  $0.15D$  for MHD. The  $C_p$  for the wider space ( $0.3D$ ) of MHD and that of MV (with a space of  $0.2D$ ) lies between the above ones. The aforementioned features can be explained as: the deceleration of flow at the indents results in the increase of pressure. The narrower span-wise space between two adjacent indents, the harder recovery of flow velocities happens. Thusly, a larger pressure coefficient occurs at these narrow spaces.

However, similar features are not significant at the trailing edge of indents. Little disparity could be observed in the curve of  $C_p$  from Figure 6.27 (b) regardless of maximum or minimum values.

## 6.6 Summary

Large Eddy Simulation have been conducted to study the flow over the half-indented circular cylinders at  $Re = 3900$ . For section 6.1, three half uniform-indented cylinders with small, medium and large indentation sizes, namely S1, M2 and B3 have been taken into consideration. For section 6.2, three half indented cylinders with vertical,

horizontal and dense horizontal indentation arrangements, namely MV, MH and MHD have been taken into consideration. The flow characteristics in various aspects such as aerodynamic forces, pressure distributions, correlation coefficients and boundary layer profiles, etc. are studied. Specifically, the main findings of the current work are summarized as follows.

1. Compared to the smooth cylinder, reductions of average drag force coefficients for S1, M2 and B3 are 3.6%, 2.2% and 3.1%, respectively. For the sectional drag force,  $C_d$  reaches its maximum at the smooth surface and falls to the minimum at the indentations for the three indented cases. Among them, the fluctuation of drag forces is greatest for B3 due to a larger size of indentation. Similar zig-zag pressure distributions on the cylinder surface are also detected. The pressure oscillations are stronger for a larger indentation size. Meanwhile, the overall integrated effect of span-wise vorticity also decreases with increasing indentation size, resulting in a larger reduction of viscous drag force.

2. The stream-wise correlation for indented cylinders decreases significantly at the leading side of cylinder when compared to the smooth one. The correlations are weakened due to strong impingement, flow separation and recirculation at the indentations. In the span-wise direction, considerably lower correlation coefficients of 0.6 are observed in the three indented cylinders when compared to the smooth one (0.7). Among them, the correlations of larger indented cylinders, M2 and B3, decrease more sharply when compared with S1.

3. Generally, the boundary layer profiles of velocity are more energetic for a larger indentation size, which could lead to a lower critical Reynolds number. The influence of roughness (the size of indentation) are similar to that of dimpled or grooved ones. Furthermore, strongly distorted shear layers are detected near the vicinity of B3 case, which is absent for the other cases. The largest reduction of 7.5% in cross-fluctuating velocity also happens in B3, resulting in a mitigation in r.m.s. lift force.

4. The discrepancy among the cases with different indentation arrangements is minor. While some interesting features can be noticed here. The sectional drag force decreases at the indents, making the abrupt reduction in the drag force curve for MH and MHD cases. Due to the larger space between two adjacent indents in span-wise direction, the correlation value is higher than fully indented model. The pressure value is also related to the distance between two adjacent indents. Larger pressures occur at the narrower spaces, owing to a slight velocity recovery.

# Chapter 7 Indentations on circular cylinders with different locations and shapes

## 7.1 Case setup

### Geometry

In the former Chapters, the indented cylinders had a smooth surface. In the real case, however, when the indentation is created by pressing into the surface, a small bump will be formed at the edge of indentation. Figure 7.1(a) shows the indentation and its edge bumps on an actual cable adopted in Tataru Bridge. In order to investigate the minor difference on the small bump, two different types of indentations were taken into consideration in this Chapter. The design picture and geometry models of these indentations is shown in Figure 7.1 (b) & (c).

The first type of indentation (*IND*, Figure 7.1 (b)) has the same configuration as the one in Chapter 5. The bumped model has the same indentation size with *IND* model. The bump is created by a semicircle ( $r=0.8\text{mm}$ ) sweeping along the edge of indentation (*BIND*, Fig 7.1 (c)).

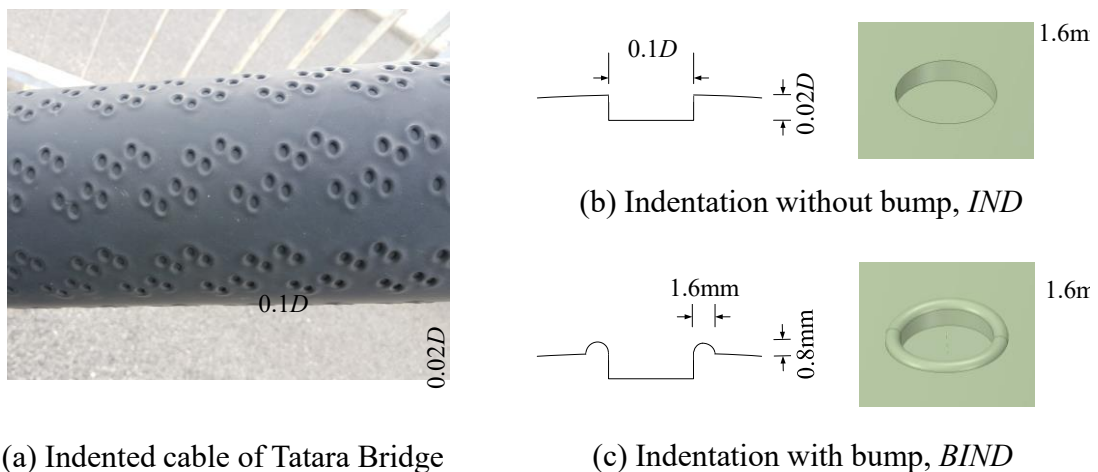


Figure 7.1 *Left*: Indented cable of Tataru Bridge;  
*Right*: Design sketch and 3D models of indentation

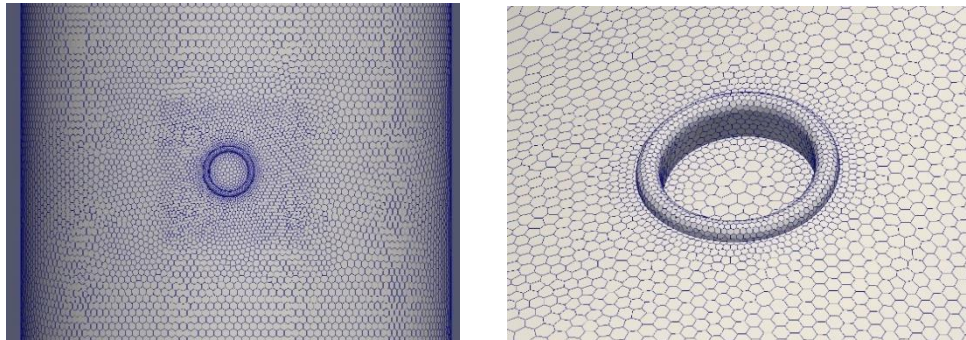
On the cylinder surface, only one indentation is located on one side of the cylinder, so that the geometry is asymmetric with respect to the flow direction. The positions of the indentation are represented by an angle  $\theta$  measured from the foremost point of the cylinder, as usual.

A span-wise length of  $1D$  was employed in the simulation to save the computational

cost. The cylinder aspect ratio was not large enough here. Thusly, the pressure and drags on the cylinder were not obtained in the present simulation. However, for estimating the effect of single indentation qualitatively or relatively, these models were sufficient because all the simulation were conducted under the same methods with the former Chapters.

## Meshing

For two types of indentation, unstructured polyhedral mesh has been adopted. The meshing size of IND is the same with those in Chapter 5. In terms of BIND, two more density boxes are added around the indentation owing to the small size of the bump. To describe the curved surface, the minimum mesh size on the convexity is about 1/5 of the bump's diameter. The grids of and around the indentation (BIND model) are presented in Figure 7.2. The cell number of IND and BIND cases are around  $4 \times 10^5$  and  $7 \times 10^5$ , respectively.



(a) density boxes around the indentation      (b) grids of the bump

Figure 7.2 Meshing of indentation with bumps (BIND)

## 7.2 Different locations and shape of indentations

### Boundary layer profiles

As discussed in Section 6.1.6, it is investigated that the boundary layer profiles of stream-wise velocity at the downstream location of indentation increase when compared to the smooth cylinder. Thusly, the same method is adopted for the different shapes of indentation here. Figure 7.3 presents the non-dimensional difference *diff* between the smooth cylinder and the indented models. The variable *diff* is defined in Equation 6.2.

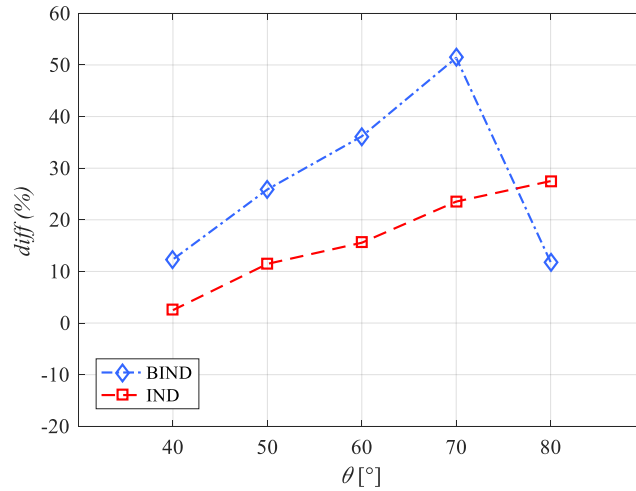


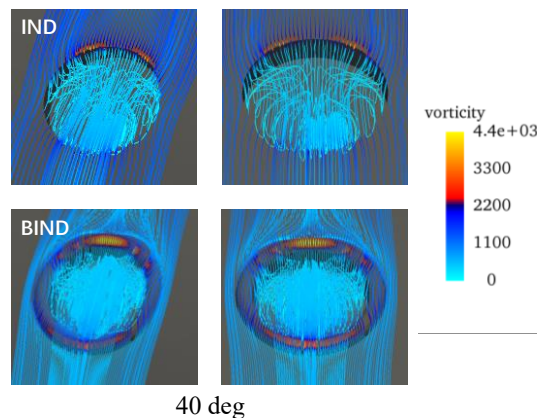
Figure 7.3 Difference of boundary layer profiles of velocity

For both types of indentation, positive *diff* is detected at all the angles, indicating larger velocities at the downstream surfaces of indentation. Larger *diff* values are identified with an increasing angle except for BIND at 80 deg.

Between  $\theta = 40$  and 70 deg, the *diff* value of BIND is around 2 times larger than IND and the difference between them is larger with an increasing angle. At  $\theta = 80$  deg, the *diff* value of BIND drops to 12%, which is about half of IND. The reason for the sudden drop of BIND case is considered later.

The above results show that both IND and BIND can energize the boundary layer near the downstream surface of indentation. Before  $\theta = 80$  deg, the indentation with small bump is much more effective in making the boundary layer energetic. To understand the different flow mechanisms between these two cases, more detailed visualization near the indentations are investigated in the following sections.

## Flow visualizations



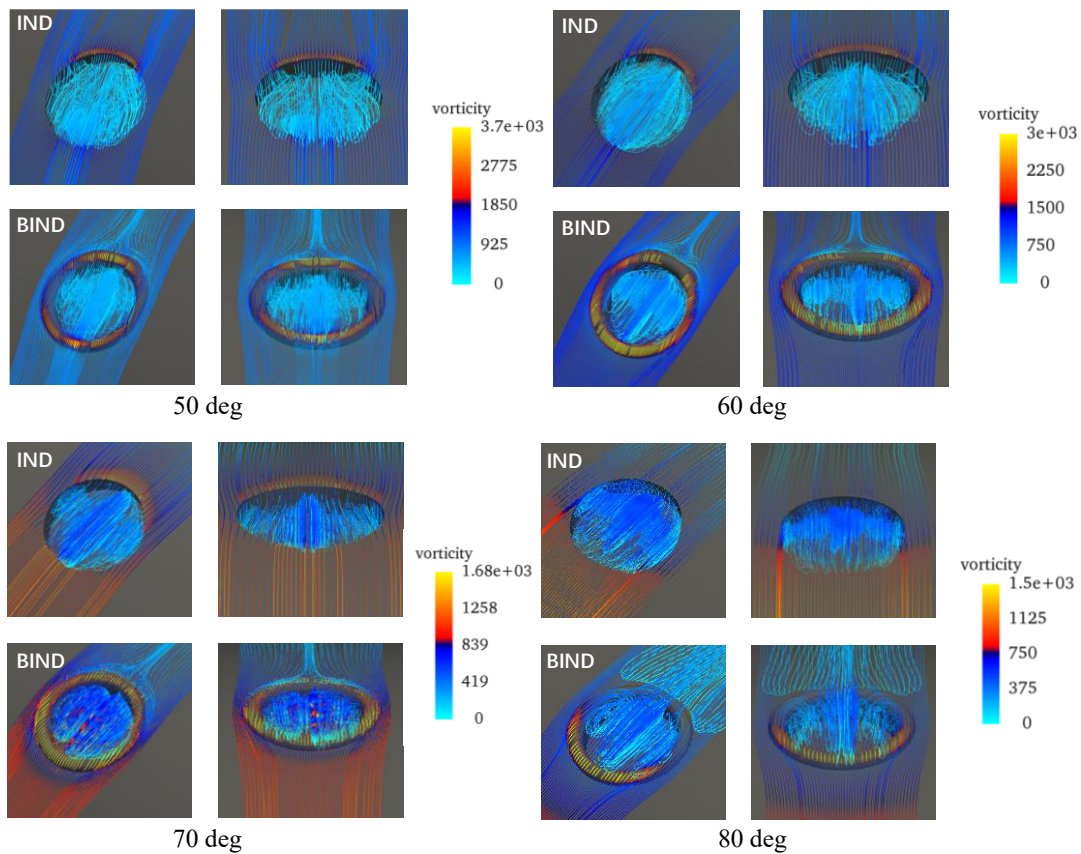


Figure 7.4 The mean streamlines of two models at various angles

The mean streamlines of two models at various angles are presented in Figure 7.4. The snapshots are taken at oblique and front view, respectively. The figures are rendered with the vorticity magnitude.

It is obvious that a closed circulating cavity flow is formed inside the indentation for both two cases with low vorticity. It seems that the separating streamline detached at the leading edge and reattached at the surface downstream. Thusly a closed circulating cavity flow is formed in the indentation. This phenomenon is similar to groove or dimple [26] [60].

For IND model, the flow mechanism is similar at different positions. Higher vorticity values are only detected at the trailing edge of indentation. Conversely, the increase is not that significant at leading edge where the flow separates.

For BIND model, significant vorticity values are detected at both leading and trailing edge (bumps) between  $\theta = 40$  to  $70$  deg. Besides the cavity flow inside the indentation, some small vortices are also generated at the location just downstream of the trailing bump. At  $\theta = 80$  deg, the separated flow failed to reattach at the downstream surface thus increased vorticity is not detected at the trailing bump.

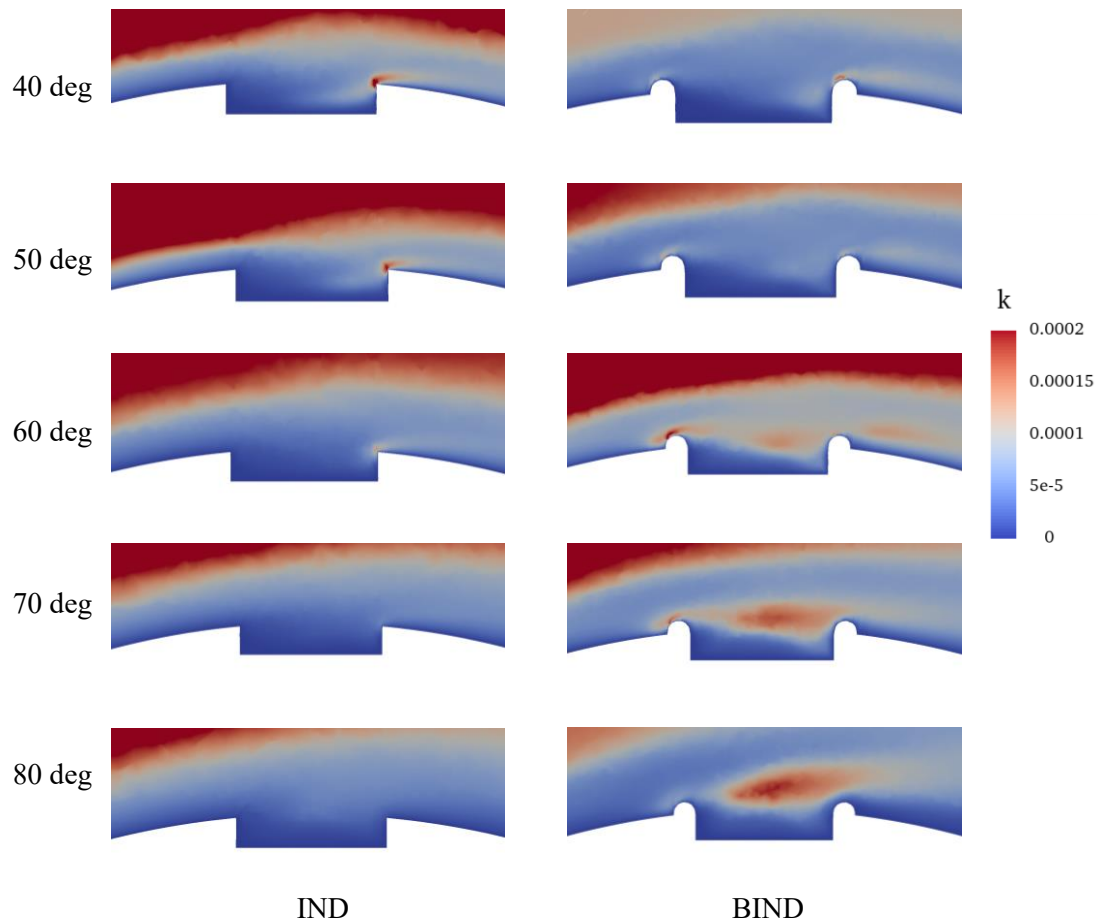


Figure 7.5 turbulent kinetic energy near the indentation at various angles

Figure 7.5 presents the average turbulent kinetic energy ( $k$ ) near the indentation at different angles. The slice is taken at the center plane of the indentation.

For IND, large  $k$  value is detected only at the trailing edge which is consistent with the vorticity distribution. This is due to the impact of detached flow on the trailing edges, thusly resulting in the acceleration of velocity and higher energy downstream the indentation.

The  $k$  value for BIND increases at both front and back bumps between  $\theta = 40$  to 70 deg with significant vorticity magnitude. The region with higher energy downstream of the bumps are much wider when compared with IND. It is worth noticing that the area right above the indentation near the back bumps is also filled with high value of  $k$ . This phenomenon indicates that the flow separated from the front bump generates the cavity flow with high energy. As the angle increases, the energized region above the indentation becomes broader, which contributes to a larger velocity at both sides of the bumps. As  $\theta = 80$  deg, the circulating cavity flow moves upward from the center of indentation with strong motion. This upwash region does not reattached due to the uplift of bumps.

## Flow mechanisms

As the abovementioned flow visualization results showed, the mechanism and effect of two types of indentation is somehow different. The difference lies in the two models are explained as follow. The flow patterns at the indentation are sketched and shown in Figure 7.6.

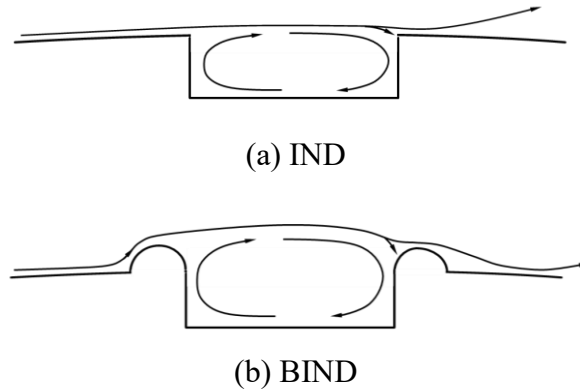


Figure 7.6 Sketch of flow at the indentations

For the IND case, the flow detaches at the front edge and crashes into the trailing edge. Some fluid reattaches to the surface with high energies and moves downstream. The other downward fluid moves into the indentation and forms the circulating cavity flow.

For the BIND case, the flow first run into the front bump and it is lifted by it with the acceleration of velocity. When the fluid travels downstream and meets the back bump, some also reattaches and evolves downstream and some forms the separation bubble inside the indentation. It is worth noticed that owing to the convex of the bump, the net depth of indentation is larger than IND. Thusly, the size of circulating cavity flow is somehow thicker. This contributes to a greater acceleration to velocity near the surface as shown in Chapter 6.

The main differences between the two models can be concluded as follow:

The BIND case includes concave and convex parts, which equals to a larger surface roughness to some extent, i.e., the additional convex parts and the deeper size of indentation. The twice impacts on the convex when the fluid travels bring more energies to the boundary layers. Together with the disturbances existing in the larger separation bubble, it results in a larger velocity near the surface downstream. Thusly, the indentation with bump energizes the boundary layer much more effectively than the one without bump.

## 7.3 Discussions

### Indented cylinder at a higher Reynolds number

As far as a smooth circular cylinder is concerned, the boundary layer control method



changes the boundary layer flow characteristics from laminar to turbulent and thus delays the main separation, resulting in drag reduction. To delay the main separation, the near-wall streamwise momentum should be enhanced to overcome the adverse pressure gradient formed in the rear part of the cylinder.

This idea has bred several kinds of aerodynamic modifications such as surface roughness, dimples, axial grooves and indentations, etc. The abovementioned modification methods can be classified into two groups, direct boundary-layer transition to turbulence or through early separation and reattachment before the main separation [60]. Obviously, the method of indentation investigated in this study belongs to the second type.

As discussed in this Chapter, the indentation causes local flow separation and empowers the boundary layer. Thusly the reattachment to the surface with higher momentum near the wall downstream of indentation.

The flow Reynolds number in this study was only a few thousand and the boundary layer was kept laminar. The relatively low Reynolds number (3900) was chosen is mainly due to the computational resources. A low-Reynolds-number flows are easier to calculate, and the drag coefficient does not vary that much for the subcritical Reynolds numbers.

In this study, two more cases with the same indentations located at  $\theta = 60$  deg at  $Re=1.5 \times 10^4$  are conducted by means of LES. The fluctuating stream-wise velocity ( $U_{rms}$ ) contours near the indentation of two cases as well as the smooth cylinder at two Reynolds numbers are depicted in Figure 7.7.

For  $Re=1.5 \times 10^4$ , though the Reynolds number is still a subcritical one, the velocity fluctuations strongly increase along the separating shear layer due to the shear layer instability. The increased fluctuation not only detected above but inside the indentation as well. However, the similar phenomenon is not observed at lower Reynolds number (3900). Choi et al. [58] conducted experiments on a golf ball with dimples and observed a rapid increase in turbulence intensity above the dimples, which causes the flow to reattach on the surface with a higher momentum near the wall and thus delay the separation. Although the current cases are conducted at a lower Reynolds number, the similar turbulence intensity above the indentations is also detected even when the boundary layer remains laminar.

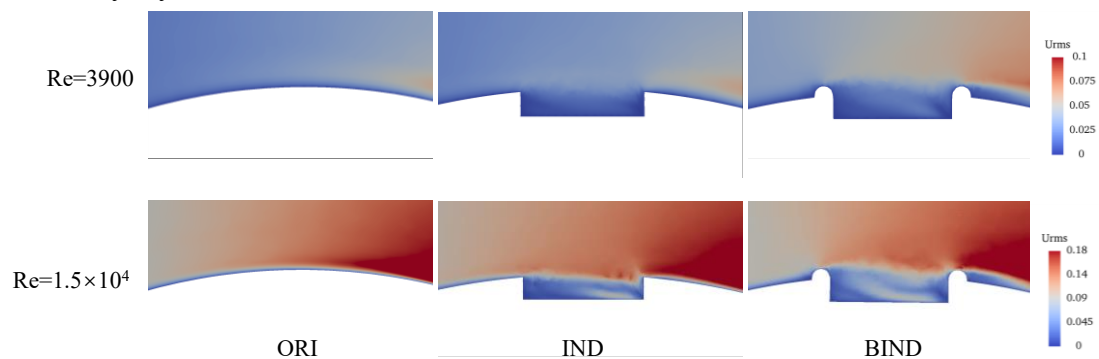


Figure 7.7 The fluctuating stream-wise velocity at the indentation

That is to say, the effects of the indentations, as a result of cavity flows inside them, will still work at higher Reynolds number flows in which the boundary layer ahead of the indentations is turbulent, because the circulating cavity flow will apparently be formed in such flows. Furthermore, for the so-called trans-critical Reynolds number, which are much higher than the critical ones, the indentation will still be effective. In the actual case, the structures usually suffer huge aerodynamic forces at this Reynolds number region and thusly drag reduction under this circumstance is very effective in reducing costs.

## Usages of indentation

Up till now, the investigations of indentation are focused on the circular cylinder. However, it is interesting to know this kind of modification on other objects. Thusly, in this section, the application range of indentations on other bodies will be discussed.

## Separation points

Although there are many different shapes of bluff bodies, we propose to classify them into two main categories with or without fixed separation points. The first class is the bluff bodies having a fixed separation point such as rectangular prism, bluff bodies with a blunt trailing edge, etc. The ones having a movable separation point such as circular cylinders and spheres are the representative 2D and 3D bluff bodies, respectively. The boundary-layer control method of indentations is applied to bluff bodies having a movable separation point. For those having a fixed separation point, the direct-wake control which directly modifies the wake characteristics, can be applied [59] [60].

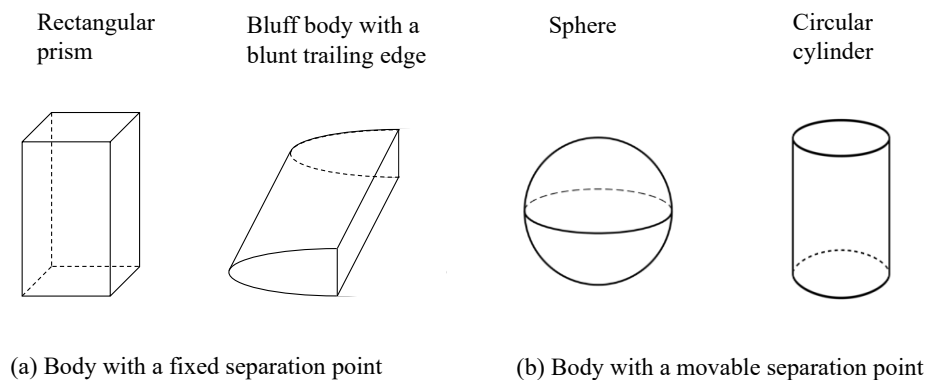


Figure 7.8 Sketch of bodies with and without a separation point

## Shape of bodies

The drag force of viscous flow past a body consists of two components, i.e., the skin friction drag ( $D_f$ ) and the pressure drag ( $D_p$ ).

$D_f$  is the drag mainly attributed to skin friction, that is, the component in the drag

direction of the integral of the shear stress over the body. Conversely, the pressure drag is mainly resulted from flow separation, the component in the drag direction of the integral of the pressure distribution over the body [61] .

The indentations enhance the near-wall streamwise momentum by early separation and reattachment to delay the main separation. It results in a significant pressure drop on the rear surface of the body and thusly the drag reduction is achieved. As presented in the previous sections, the influence of friction drag is obviously more significant at the surface of indentations compared with the smooth one. However, for the case of circular cylinder, the percentage of friction forces was estimated to be less than 3%, which is negligible in comparison with the pressure drag [25] . Thusly, the drop of pressure drag is much more effective in reducing the drag.

However, does it mean that indentations are effective for all the bodies with a movable separation point? The answer is apparently not. It depends on the shape of the body.

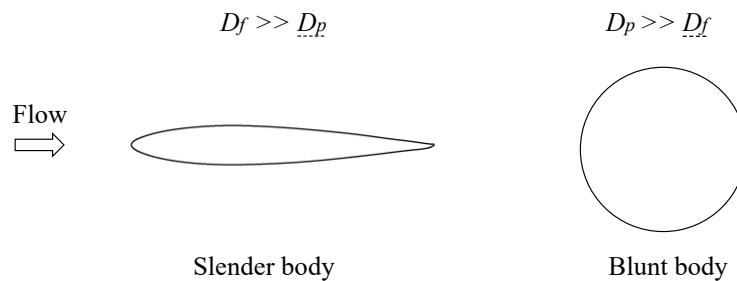


Figure 7.9 Shape of slender and blunt bodies

As sketched in Figure 7.9, if the body is slender or streamline such as the airfoil, water drop shape, etc., the friction drag is much greater than pressure one. Laminar boundary layer is preferable because the friction is obvious smaller for laminar than turbulent. For this case, the indentation is not desirable. In contrast, if the body is blunt such as sphere or circular cylinder, circular cone, etc., the pressure drag is much greater. The indentation as well as dimples, grooves are desirable due to the reason discussed above.

Therefore, for any given body, the aerodynamic virtues of laminar versus turbulent flow must be assessed before using the indentation. In the current status, the experiments should be a more preferable mean to assess the given body due to the expensive computational cost to calculate the indented cases. However, as the development of computer, such as quantum computer which can solve many problems faster than classical computers, it may be possible to assess the indented body cheaply in the future.

## 7.4 Summary

In this chapter, LES have been conducted on a circular cylinder with only one indentation at various positions on the surface. Two different types of indentations are taken into consideration, i.e. the indentation with and without bumps along the edges.

The flow patterns are investigated, and further discussion are considered. The main conclusions are listed as follows.

1. Before  $\theta = 80$  deg, the near-wall streamwise velocity downstream the indentation of BIND model is much larger than the one of IND at  $Re=3900$ . By the streamline visualization, a closed circulating cavity flow are formed inside the indentation for both types. However, the fluid passing through the BIND generated more energy with high vorticities owing to the skin friction of bumps. Wider empowered regions at the bump, downstream and above the indentations are detected on BIND. The larger roughness attributed from the bump and deeper indentation may results in a larger drag reduction at a higher Reynolds number.

2. The flow Reynolds number (3900) in this study was only a few thousand and the boundary layer was kept laminar due to the computational resources. By investigating the same cases at a higher Reynolds number ( $1.5 \times 10^4$ ), results show that higher energies are observed at the region above and downstream the indentations for both types. Thusly, it is believed that for a trans-critical Reynolds number, the indentation will still be effective, because the circulating cavity flow will also be formed in such flows.

3. The indentations are not desirable for all the given bodies. In general, the drag attributed from the pressures are much larger than the friction one for the blunt bodies with a movable separation point such as sphere, circular cylinder, etc. Thusly turbulent boundary layer is preferable to delay the main separation. For these cases, the indentation can be adopted. However, for other given bodies, the assessments should always be conducted before using the indentations.

# Chapter 8 Final Remarks

## 8.1 Conclusions

In this report, investigation of the flow characteristics and the resulting forces on various indented circular cylinders has been presented by the means of large eddy simulation at a Reynolds number of 3900. This report aims at investigating the difference in flow characteristics and its mechanisms on the indented cylinders and finally to improve the understanding of flow mechanism in drag mitigation at higher Reynolds numbers.

The first goal was to simulate reliably and effectively for the flow around a circular cylinder. By using the three-dimensional LES simulation, the process of verification and validation were done. The results show that the flow past a smooth cylinder was successfully simulated.

The second objective is achieved by investigating the different aerodynamic performances which depend on the indentation positions. It is revealed that the indentations located at the frontal part of cylinder surface is effective to reduce the viscous drag. The drag force reduces at the indentations, making the drag force curve zigzag in the span-wise direction. It is identified that the closed circulating flow is formed at the frontal indentations, which is filled with low momentum quiescent flow. By studying the flow characteristics at the location right downstream of indentations, both velocities and vorticities are larger than that of the smooth cylinder, making the boundary layers more energetic and thusly transit from laminar to turbulence at a lower Reynolds number.

Based on the above region division, numerical simulations are conducted on half frontal-indented cylinder with various indentation sizes. For the different sizes of indentations, lower negative pressure is detected at the edge of indentations with the increasing indentation size, resulting in a greater pressure recovery. By the comparison of boundary layer profiles of velocities at place where the minimum pressure locates (just downstream of indentation), it is revealed that larger size of indent leads to a greater increase in velocities. While the lower span-wise correlation is detected for a larger indent size. It can be concluded that the rougher the surface, the more energetic the boundary layer, thusly the lower critical Reynolds number. The features observed above is similar to the dimpled and grooved one, which is quite effective in reducing the drag force in post-critical regime.

In order to simulate the indentation adopted on the actual cables, two types of indentation with and without edge bump are also conducted by means of LES. It is found that the indentation with bump empowers the near-wall velocity profiles greater than the IND. By investigating the flow visualization of two types indentation, the flow mechanism can be concluded as the follow: the bump increases the surface roughness as well as deepen the indentation, thusly the skin friction increases and results in an

acceleration of velocity. More discussions on the effect of indentation at a higher Reynolds number and the potential usages on other bodies are listed. As a conclusion, the indentation can be adopted for blunt body with a movable separation points such as sphere, circular cylinder, etc. For any certain body, the assessments must be done to judge whether the indentation is of positive effect or not.

Besides the above conclusions, the current studies should trigger more interesting research topics into the indentation roughness.

## **8.2 Prospects for future researches**

Although the roughened cylinders have been widely and deeply studied in the past decades and its efficiency on flow control and vibration suppression has been recognized, we clearly realize that still a lot of unknown issues need to be disclosed. Thusly, here some ideas are listed which might be worth research effort in the near future.

- Until now, all the investigations on the indented cylinders at super critical or trans critical Reynolds number have been conducted by wind tunnel tests or field studies. The three-dimensional numerical simulation must be helpful in understanding the mechanism of drag reduction at post-critical regime. However, the resolution of this kind of model is extremely computationally expensive. Thusly, future development of computer science might make it easier to fulfil.
- All the cases considered in the current thesis are subjected to the normal incoming flow. In the actual case, the flow is not always perpendicular to the structures, thus it is worthwhile to investigate the aerodynamic characteristics when the flow is inclined to the cylinder. However, due to the small size of indentation, the mesh number needed for simulation is quite large. In that case, a span-wise length of 2D is not enough, indicating a more expensive computational cost.
- It is also interesting to know the efficacy of the combination of passive flow control and active flow control. For example, indented cylinder with span-wise distributed forcing (Kim and Choi [59] ). This kind of combination could work more effectively to flow control or not is of great interests to civil engineers.

## Bibliography

- [1] Hojo, Tetsuo, Shinsuke Yamazaki, and Hiroyuki Okada. Development of low drag aerodynamically stable cable with indented processing. *Nippon Steel Technical Report*, 82, 15–22 (2000).
- [2] Svensson, Holger. *Cable-stayed bridges: 40 years of experience worldwide*. John Wiley & Sons (2013).
- [3] Miyata, T., Yamada, H., Fujiwara, T., Hojo, T. Wind-resistant design of cables for the Tatara bridge. *IABSE Symposium on Long-span and High-rise Structures*, Kobe, Japan, September, 79, 51–56 (1998).
- [4] Chen, Z.Q. Cable vibration incidence of the Jintang Bridge, Hunan University, private communication, July (2011).
- [5] Katsuchi, H., Yamada, H. Dry galloping characteristics of indented stay cables in turbulent flow. *9th International Symposium on Cable Dynamics*, Shanghai, China, 359–364, (2011).
- [6] Kleissl, K., Georgakis, C. T. Comparison of the aerodynamics of bridge cables with helical fillets and a pattern-indented surface. *Journal of Wind Engineering and Industrial Aerodynamics*, 104-106, 166-175 (2012).
- [7] 岩崎 聖. 空力振動現象に対するインデントケーブルの改良と水路形状の解明. 横浜国立大 (2017).
- [8] K. J. Niklas and S. L. Buchman, The allometry of saguaro height. *Amer. J. Botany*, 81, 1161–1168 (1994).
- [9] Hodge, C. *All about Saguaros*. Hugh Harelson-Publisher, Phoenix (1991).
- [10] G. N. Geller and P. S. Nobel. Cactus ribs: influence on PAR interception and CO<sub>2</sub> uptake. *Photosynthetica*, 107, 482–494 (1984).
- [11] Bearman, P. W. Golfball aerodynamics. *Aeronautical Quarterly* 27, 112–122 (1976).
- [12] Bechert, D et al. Fluid mechanics of biological surfaces and their technological application. *Naturwissenschaften*, 87(4), 157-171 (2000).
- [13] Lentink, D and de Kat, R. Gliding swifts attain laminar flow over rough wings. *PloS ONE*, 9(6), e99901 (2014).
- [14] Malik, K et al. Effects of bio-inspired surface roughness on a swept back tapered NACA 4412 wing. *Journal of Aerospace Technology and Management*, 11, e1719 (2019).
- [15] Batchelor, G.K. *An Introduction to Fluid Dynamics*. Cambridge University Press. (1967).
- [16] Williamson, C.H.K. The existence of two stages in the transition to three-dimensionality of a cylinder wake. *The Physics of fluids* 31.11, 3165–3168 (1988).
- [17] Bloor, M Susan. The transition to turbulence in the wake of a circular cylinder. *Journal of Fluid Mechanics* 19.02, 290–304 (1964).
- [18] Schewe, Günter. On the force fluctuations acting on a circular cylinder in crossflow

- from subcritical up to transcritical Reynolds numbers. *Journal of fluid mechanics* 133, 265–285 (1983).
- [19] Rodríguez, I et al. On the flow past a circular cylinder from critical to supercritical Reynolds numbers: Wake topology and vortex shedding. *International Journal of Heat and Fluid Flow* 55, 91–103 (2015).
- [20] Lehmkuhl, O et al. Unsteady forces on a circular cylinder at critical Reynolds numbers. *Physics of Fluids* 26.12, 125110 (2014).
- [21] Gerrard, J. H. The mechanics of the formation region of vortices behind bluff bodies. *Journal of Fluid Mechanics* 25.02, 401–413 (1966).
- [22] Zdravkovich, MM (1997). *Flow around circular cylinders, vol. 1: Fundamentals*, — (2003). “*Flow around circular cylinders, vol. 2: Applications*”. Oxford University Press, ISBN 0 19.856561, p. 5.
- [23] Norberg, Christoffer. Fluctuating lift on a circular cylinder: review and new measurements. *Journal of Fluids and Structures* 17.1, 57–96 (2003).
- [24] Achenbach, E., and Heinecke, E. On Vortex Shedding from Smooth and Rough Cylinders in the Range of Reynolds Numbers  $6 \times 10^3$  to  $5 \times 10^6$ . *Journal of Fluid Mechanics*, 109, 239-251 (1981).
- [25] Achenbach, E. Influence of Surface Roughness on the Cross-flow around a Circular Cylinder. *Journal of Fluid Mechanics*, 46, part 2, 321-335 (1971).
- [26] Kimura, T., and Tsutaharat, M. Fluid Dynamic Effects of Grooves on Circular Cylinder Surface. *AIAA Journal*, 29, 2062-2068 (1991)
- [27] P. W. Bearman & J. K. Harvey. Control of circular cylinder flow by the use of dimples. *AIAA Journal*, 31, 1753-1756 (1993).
- [28] Zhou, B., Wang, X. K., Guo, W., Gho, W. M., Tan, S. K. Control of flow past a dimpled circular cylinder. *Experimental Thermal and Fluid Science*, 69, 19-26 (2015).
- [29] Babu, P., Mahesh, K. Aerodynamic loads on cactus-shaped cylinders at low Reynolds numbers. *Physics of Fluids*, 20, 035112 (2008)
- [30] Liu, Y. Z., Shi, L. L., and Yu, J. TR-PIV measurement of the wake behind a grooved cylinder at low Reynolds number. *Journal of Fluids and Structures*, 27, 394-407 (2011).
- [31] Zhou, B., Wang, X. K., Guo, W., Gho, W. M., Tan, S. K. Experimental study on flow past a circular cylinder with rough surface. *Ocean Engineering*, 109, 7-13 (2015).
- [32] 沖 真, 青木克巳, 中山泰喜. 溝つき円柱まわりの流動特性に対する溝深さの影響, 日本機械学会論文集 B 編, 65, 631, 870-875 (1999).
- [33] 山岸 陽一, 木村 茂雄, 沖 眞. 溝つき円柱の抗力低減に関する研究. 日本機械学会論文集 B 編, 79, 805, 1742-1751 (2013).
- [34] Smagorinsky, Joseph. General circulation experiments with the primitive equations: I. the basic experiment. *Monthly Weather Review*, 91. 3, 99–164 (1963).
- [35] Germano, Massimo et al. A dynamic subgrid-scale eddy viscosity model. *Physics of Fluids A: Fluid Dynamics* (1989-1993) 3.7, 1760–1765 (1991).



- [36] Fureby, C et al. A comparative study of subgrid scale models in homogeneous isotropic turbulence. *Physics of Fluids*, 9.5, 1416–1429 (1997).
- [37] Versteeg, Henk Kaarle and Weeratunge Malalasekera. An introduction to computational fluid dynamics: the finite volume method. Pearson Education (2007).
- [38] Jasak, Hrvoje. Error analysis and estimation for finite volume method with applications to fluid flow. PhD thesis. Imperial College London (1996).
- [39] Mittal, R., Moin, P. Suitability of upwind biased schemes for large-eddy simulation. *AIAA J.* 30(8), 1415–1417 (1997)
- [40] Parnaudeau, P., Carlier, J., Heitz, D., Lamballais, E. Experimental and numerical studies of the flow over a circular cylinder at Reynolds number 3900. *Phys. Fluids*. 20(8), 85-101 (2008)
- [41] Lysenko, Dmitry A, Ivar S Ertesvåg, and Kjell Erik Rian. Large-eddy simulation of the flow over a circular cylinder at Reynolds number 3900 using the OpenFOAM toolbox. *Flow, Turbulence and Combustion*. 89(4), 491–518 (2012)
- [42] Kravchenko, A., Moin, P. Numerical studies of flow over a circular cylinder at  $Re=3900$ . *Phys. Fluids*. 12(2), 403–417 (2000)
- [43] Breuer, M. Large eddy simulation of the sub-critical flow past a circular cylinder: numerical and modeling aspects. *Int. J. Numer. Methods Fluids*. 28, 1281–1302 (1998)
- [44] Lehmkuhl, O., Rodríguez, I., Borrell, R., Chiva, J., Oliva, A. Unsteady forces on a circular cylinder at critical Reynolds numbers. *Phys. Fluids*. 26 (12), 125110 (2014)
- [45] Lourenco, L.M., Shih, C. Characteristics of the plane turbulent near wake of a circular cylinder, a particle image velocimetry study. Published in Ref. [51] (1993)
- [46] Norberg, C. Experimental investigation of the flow around a circular cylinder: influence of aspect ratio. *J. Fluid Mech.* 258, 287–316 (1994)
- [47] Norberg, C. Flow around a circular cylinder: aspects of fluctuating lift. *J. Fluids Struct.* 15, 459–469 (2001)
- [48] Dong, S., Karniadakis, G.E., Ekmekci, A., Rockwell, D. A combined direct numerical simulation particle image velocimetry study of the turbulent air wake. *J. Fluid Mech.* 569, 185–207 (2006)
- [49] Ma, X., Karamanos, G.S., Karniadakis, G.E. Dynamics and low dimensionality of a turbulent near wake. *J. Fluid Mech.* 410, 29–65 (2000)
- [50] Franke, J., Frank, W. Large eddy simulation of the flow past a circular cylinder at  $Re = 3900$ . *J. Wind Eng. Ind. Aerod.* 90, 1191–1206 (2002)
- [51] Beaudan, P., Moin, P. Numerical experiments on the flow past a circular cylinder at sub-critical Reynolds number. Technical Report TF-62, CTR Annual Research Briefs, NASA Ames/Stanford University (1994)
- [52] Hunt, Julian C.R, Alan A Wray, and Parviz Moin. Eddies, streams, and convergence zones in turbulent flows. Center for Turbulence Research CTR-S 88 (1988)
- [53] Williamson, C. H. K. Vortex dynamics in the cylinder wake. *Annu. Rev. Fluid*

- Mech. 28, 477-539 (1996)
- [54] Unal M F, Rockwell D. On vortex shedding from a cylinder: Part 1. The initial instability. *J. Fluid Mech.* 190-491 (1988)
- [55] S. Talley, G. Iaccarino, G. Mungal and N. Mansour, An experimental and computational investigation of flow past cacti, Annual research briefs, Center for turbulence research, NASA Ames/Stanford Univ., 51–63 (2001).
- [56] S. Talley and G. Mungal, Flow around cactus-shaped cylinders, Annu. research briefs, Center for turbulence research, NASA Ames/Stanford Univ., 363–376 (2002).
- [57] Yamagishi, Y., and Oki, M. Effect of the Number of Grooves on Flow Characteristics around a Circular Cylinder with Triangular Grooves, *Journal of Visualization*, Vol. 8, No. 1, 57-64 (2005).
- [58] Choi, H., Jeon, W. P. and Kim, J. Mechanism of drag reduction by dimples on a sphere. *Physics of Fluids*, 18, 041702 (2006).
- [59] Kim, J. and Choi, H. Distributed forcing of flow over a circular cylinder. *Physics of Fluids (1994-present)* 17.3, 033103 (2005).
- [60] Choi, H., Jeon, W. P. and Kim, J. Control of flow over a bluff body. *Annual Reviewer Fluid Mechanics*, 40, 113–139 (2008).
- [61] John D. Anderson, Jr. *Fundamentals of Aerodynamics*. McGraw-Hill. The fifth edition (2011).